4-13-2017

Magnetic Properties of Porous Iron Oxides and their Application as Desulfurization Sorbents

Jing Jin
Institute of Materials Science, jing.jin@uconn.edu

Magnetic Properties of Porous Iron Oxides and their Application as Desulfurization Sorbents

Jing Jin, Ph.D.

University of Connecticut, 2017

This work focused on the study of porous iron oxides and on applying them as a desulfurization sorbent. The advantages of this sorbent material are gaining high sulfur sorption capacity at a low working temperature with a cheaper price. To achieve this goal, the research was broken down into three sections: (1) material synthesis and magnetic study; (2) the study on the desulfurization process; (3) high sulfur sorption capacity sorbent and condition optimization.

In the first section, the different phased iron oxides with different porous structure were synthesized by the improved inversed micelle sol-gel method. The mesoporous maghemite and magnetite were carefully studied by an ^{57}Fe spin-echo nuclear magnetic resonance (NMR) and a magnetometer. From those magnetic studies, the phases of iron oxides were identified. In addition, the crystalline structure, morphology and the porosity of the structures were characterized using X-ray diffraction (XRD), transmission electron microscope (TEM), scanning electron microscope (SEM), and N_2 sorption techniques.

The process parameters are also very important to improve the sulfur sorption capacity. According to the experimental data, the pressure on the sorbent during the desulfurization process greatly improves the sorption efficiency. The sorption capacity would be increased more than 3 times compared with the same sorbent without pressure. All those detailed analyses and discussion are presented in the second section.

Porous hydrous ferric oxide is carefully studied as a good desulfurization sorbent in the third section. The fresh sorbent and the deactivate materials are characterized by XRD, high resolution TEM, SEM, and N_2 sorption techniques. Without the pressure, the sulfur sorption capacity of porous hydrous ferric oxide can be reached up to 58.5 under 50 sccm at 300 ^oC, which is more than 4 times higher than the commercial sample and about 50% higher than mesoporous Co_3O_4. Based on the comparison of the material characterization, the high sorption capacity is probably due to the combination effect of physical and chemical sorption.

Magnetic Properties of Porous Iron Oxides and their Application as Desulfurization Sorbents

Jing Jin

M.S., Clark University, USA, 2012

M.E., Tianjin University China, 2010

B.S., Tianjin University, China, 2008

A Dissertation

Submitted in Partial Fulfillment of the

Requirements for the Degree of Doctor of Philosophy

at the University of Connecticut

2017

APPROVAL PAGE

Doctor of Philosophy Dissertation

Magnetic Properties of Porous Iron Oxides and their Application as Desulfurization Sorbents

Presented by

Jing Jin, M.S. & M.E.

Major Advisor

Steven L. Suib

Associate Advisor

S. Pamir Alpay

Associate Advisor

Mu-Ping Nieh

University of Connecticut

2017

Dedicated to my family and everyone who loves me

ACKNOWLEDGEMENTS

My most sincere gratitude goes to my major advisor Dr. Steven L. Suib, for all his guidance, encouragement and support. Throughout my Ph.D. study, Dr. Suib not only taught me to be a good material scientist, but also to be a better person who would be stronger and more appreciative. I also would like to sincerely thank Dr. Francis Galasso who treated me as his granddaughter and gave me lots of help and suggestions during my life in UConn. Additionally, I greatly appreciate my associate advisors and committee members: Drs. S. Pamir Alpay, Mu-Ping Nieh, Pu-Xian Gao and Mark Aindow.

I would also love to thank the faculties and staff who helped me a lot throughout my Ph.D. studies. Thanks to Drs. William A. Hines, Nicholas Eddy and Vitaliy Gorbatyuk for guidance on NMR studies; thanks to Dr. Clyde Cady for guidance on EPR studies; thanks to Dr. Edward Neth, Dr. Roger Ristau, Dr. Lichun Zhang, Dr. Laura Pinatti, Dr. William Willis, Dr. Luyi Sun, Gary Lavigne, Rick George, Daniel Daleb, YoungHee Chudy, Kim Post, Nancy Kellerann, Charlene Fuller, Ashely Butler, Emilie Hogrebe for their tireless support and help.

My appreciation also goes to our former and current group members: Dr. Yashan Zhang, Dr. Jacqui E. Cloud, Dr. Altug Poyraz, Dr. Chung-Hao Kuo, Dr. Zhu Luo, Dr. Lakshitha Pahalagedara, Dr. Madhavi Pahalagedara, Dr. Ting Jiang, Dr. Abdelhamid El-Sawy, Dr. Hui Huang, Dr. Wenqiao Song, Dr. Sheng-Yu Chen, Dr. Curtis Guild, Dave Kriz, Ran Miao, Wei Zhong, Junkai He, Biswanath Dutta, Shannon Poges, Niluka Wasalathanthri, Tehereh Jafari, and everyone in Dr. Suib's group.

Finally, I am extremely grateful to my family for their love, sacrifice and support, especially to my parents. Without them, I would not be able to accomplish this work.

TABLE OF CONTENTS

LIST OF FIGURES

LIST OF TABLES

LIST OF SCHEMES

CHAPTER 1. INTRODUCTION

1.1 Overview

Recently, environmental concerns have attracted more and more attention. Due to industry development, waste and hazardous gases are released into the atmosphere. The number of people exhibiting heart, lung and respiratory diseases have increased drastically. Many cities including Los Angeles, Beijing and London have been attacked or experiencing "smog" which is due to bad air pollution. Most of the air pollution originates from coal fires, traffic emissions or volcanos. Sulfur containing compounds such as H_2S, COS, dimethyl sulfide (DMS), and CS_2 are part of the haze.[1-6] Efficiently removing sulfur contaminants will not only provide benefits for avoiding corrosion, catalyst deactivation or electrode poisoning, but also greatly protect the health of human beings. As shown in **Figure 1.1**, the concentration of 100 ppm H_2S is damaging to olfactory glands, while 2000 ppm is lethal to most people.

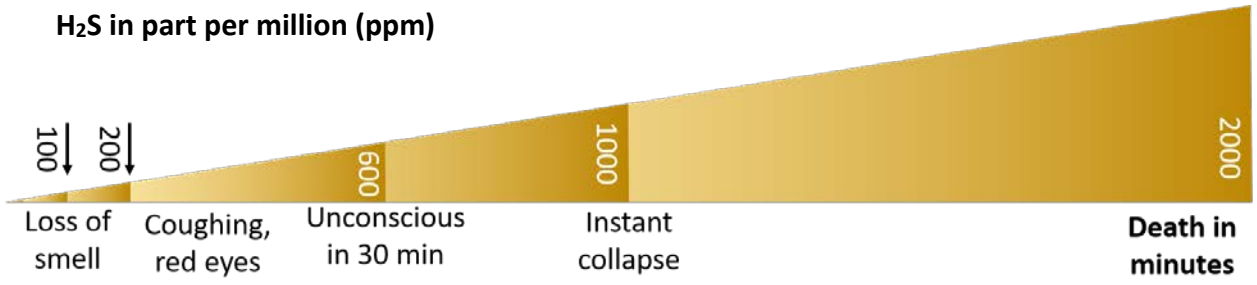

Figure 1.1 H_2S concentration effect on the human health

Porous materials, due to their large surface areas and pore structures, are widely studied and applied for adsorption, gas storage and separation, drug delivery, catalysis, and electrochemistry.[7-10] According to the pore size, the materials are classified into microporous (pore size smaller than 2 nm), mesoporous (pore size between 2 to 50 nm) and macroporous (pore size

larger than 50 nm).[11] With respect to material synthesis techniques, the use of the hard template method (nanocasting) and soft template method are the two major strategies for mesoporous material synthesis. For transition metal oxide mesoporous materials, the hard template method introduced by Rhoo and coworkers[12] is widely used. But the soft template method is problematic for transition metal oxides. Recently, Poyraz and coworkers introduced an inverse micelle sol-gel method to fabricate crystalline and monomodal pore size mesoporous materials.[13] This method not only produces mesoporous silica and carbon systems, but also can be applied to first-row transition metal oxides such as iron and cobalt.

As the commonly used desulfurization sorbents, metal oxides and metal oxide mixtures have been studied for years.[14-16] The sulfurization reaction of metal oxides used in sulfur removal can be represented by the equation below:[17-18]

$$MO_x\,(s) + x\,H_2S\,(g) \rightarrow MS_x\,(s) + x\,H_2O\,(g) \quad (1)$$

where MO_x is the fresh metal oxide sorbent and MS_x is the metal sulfide after adsorption. Therefore, the gas phase sulfur contaminants will be adsorbed by the metal oxide sorbents, and the sorbent will be sulfurized. The optimized working temperatures are varied according to the specific sorbent. Usually, zinc oxide and zinc-based sorbents are used for hot desulfurization processes, which is above 700 ^{o}C.[18-19] For low temperature desulfurization, mesoporous Co_3O_4 has been studied recently.[20] However, cobalt is relatively expensive. Therefore, porous iron oxides are carefully studied in this work. By tuning synthesis conditions, different phases and nano-structures of iron oxides were prepared and characterized before and after the desulfurization process. The optimized conditions and mechanism are studied in detail.

1.2 Background of this research

1.2.1 Porous iron oxide materials

Transition metal oxides in a mesoporous nanostructure have localized d-electrons within the thin walls between pores. The materials are endowed with unusual magnetic, semiconducting, electrical and optical properties because of their electronic nature.[21-23] The special nanostructure enables the unusual magnetic phenomena in the material, which can benefit from applications. For example, bulk Co_3O_4 is an anti-ferrimagnetic compound due to its outer level electronic configuration, but shows super-paramagnetic behavior in the mesoporous structure.[24] Therefore, coupled with the catalytic properties, the materials were proposed for additional applications to exploit their magnetic properties.

Iron oxides, as the most common magnetic materials, have been studied for decades.[25-28] Due to their cheap cost and unique properties, iron oxides have been applied to a lot of different areas, such as high-density magnetic storage, ferrofluids, and biomedical applications.[29-34]

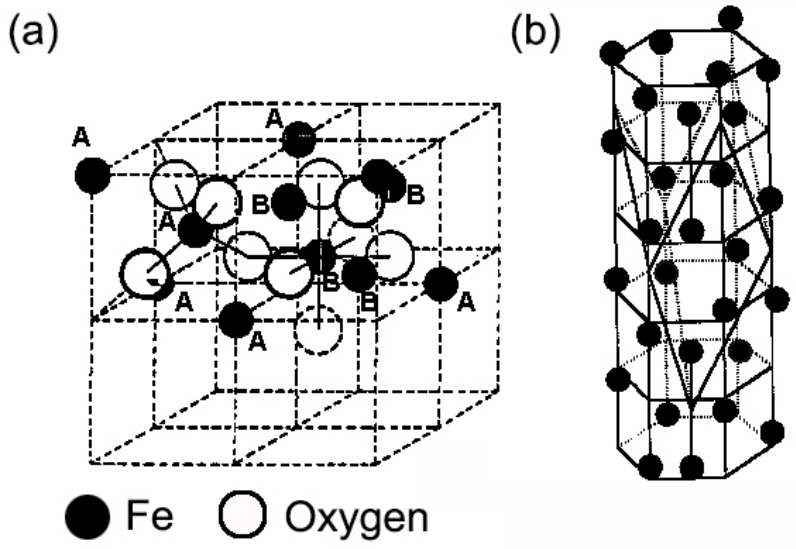

Figure 1.2 (a) Inversed spinal structure of magnetite and maghemite;
(b) Hexagonal close packed framework of hematite

Naturally, there are two oxidation states of iron which are Fe^{2+} and Fe^{3+}. The mixed oxidation state compound is Fe_3O_4, which is called magnetite. Iron (III) oxides are separated into four phases according to their crystalline structure. Among them, gamma phase iron oxide (γ-Fe_2O_3), so called maghemite, has a similar structure as magnetite which is an inverse spinal structure shown in **Figure 1.2a**.[35] Both of these are ferromagnetic materials. Another common iron (III) oxide is hematite which has the alpha phase (α-Fe_2O_3). Due to its hexagonal close packed structure, α-Fe_2O_3 is antiferromagnetic. The crystal structure is shown in **Figure 1.2b**. Many reports on the synthesis, characterization and magnetic properties of these phases of nanoparticles have been published in the past decade.[36-38] This work involves detailed studies of the mesoporous iron oxides including their crystalline structures, nanostructures, morphologies, and phase identification.

1.2.2 Desulfurization process

In industry, flue-gas desulfurization (FGD) is widely used to remove sulfur-containing exhaust flue gases and emissions. There are two stages employed in most FGD systems: fly ash removal and sulfur containing compound removal. People are still working on improving the efficiency and lowering the cost of methods. Today, alkaline sorbents are the most frequently used for FGD, such as CaO, $CaCO_3$ or $Ca(OH)_3$. There are many reports on zeolites,[39] active carbons,[40] zinc oxide, and zinc-based sorbents,[5, 16-18, 41-44] because of their high efficiency level of sulfur removal and ideal thermal stability. However, for the low-temperature process, transition metal oxides are attractive, due to thermodynamic studies, such as the oxides of Co, Cu, Mn, Cr, Fe, Ni, and W.[45-51] Among them, mesoporous Co_3O_4 has been primary studied and shows better results than other oxides.[20]

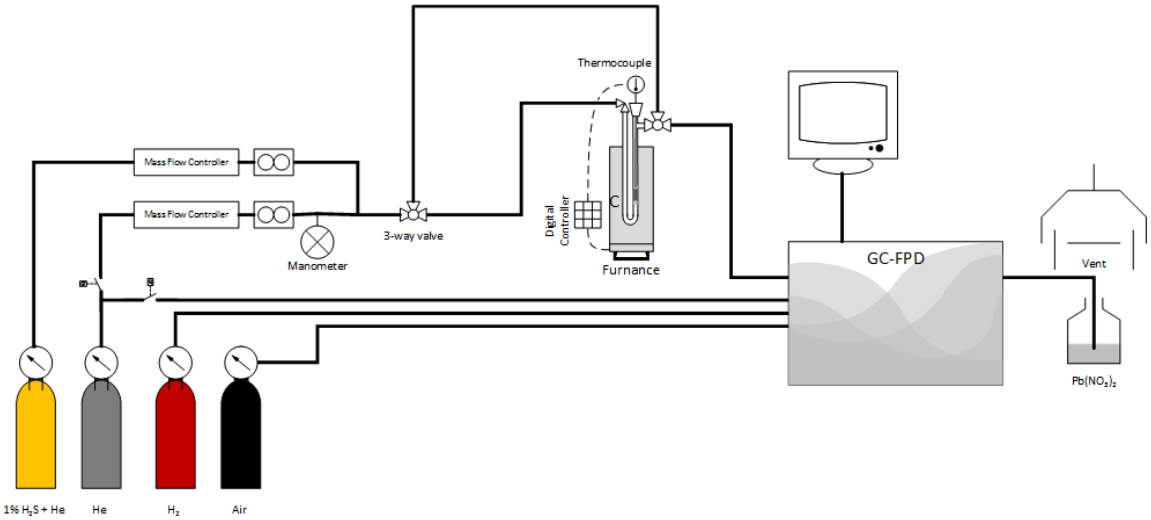

Scheme 1.1. Schematic representation of the sulfur sorption setup.

To reduce the cost and reach a higher sorption capacity, this work focused on applying porous iron oxide materials as sorbents for sulfur removal and optimize processing conditions. To test the actual desulfurization capacity of the sorbent, the FGD system was mimicked by the laboratory setup shown in **Scheme 1.1**. The diluted H_2S (1% H_2S in He) was a certified gas mixture and was purchased from Scott Specialty Gases. A U-shape tubular reactor was made of quartz with an internal diameter (I.D.) of 2 mm. The reactor was vertically oriented in a tube furnace with a proportional-integral-derivative (PID) controller. In each experiment, 50 mg of sorbent material was packed in the reactor supported by quartz wool. A J-type thermocouple was placed at the top of the sorbent bed. Prior to each experiment, the samples were heated at 200 ^{o}C with 40 sccm He flowing for 1 h. The outlet gases were analyzed for sulfur using an SRI 8610C gas chromatograph (GC) with a GS-GasPro capillary column (30 m × 0.32 mm I.D.) and a flame photometric detector (FPD). A 10-port sampling valve with an electronic actuator was used to make automatic injections into the GC every 10 min with He as the carrier gas. Two mass flow controllers (MFCs) controlled the flow rates, feed and composition. One of the MFCs is a MKS

model 1479A with 20 sccm ± 1% full scale. The other is an Alicat Scientific with 200 sccm ± 0.2% full scale. The weight hourly space velocity (WHSV) was fixed at ~ 60 L/h·g. The sulfur sorption capacity (SSC) is identified by the function below:[18]

$$\mathbf{SSC}\left(\frac{\mathbf{g-sulfur}}{\mathbf{100\ g\ sorbent}}\right) = \mathbf{WHSV}\times\left[\frac{\boldsymbol{M}}{\boldsymbol{V_{mol}}}\times\int_{\mathbf{0}}^{\boldsymbol{t}}\boldsymbol{C}_{\mathbf{in}}-\boldsymbol{C}_{\mathbf{out}}\boldsymbol{dt}\right]\cdot\mathbf{1}\times\mathbf{10}^{-\mathbf{4}} \quad \textbf{(4)}$$

where WHSV is the weight hourly space velocity in L/h·g, M is the atomic weight of sulfur, V_{mol} is the molar volume in L/mol at standard conditions (298 K and 1 atm). C_{in} and C_{out} are the inlet and outlet concentrations in ppm, and t is the breakthrough time in h. The breakthrough time was the time when the outlet concentration reached 50 ppm.[18, 20]

1.3 References

1. Van der Drift, A.; Van Doorn, J.; Vermeulen, J., Ten residual biomass fuels for circulating fluidized-bed gasification. *Biomass and Bioenergy* **2001,** *20* (1), 45-56.

2. Leppälahti, J.; Koljonen, T., Nitrogen evolution from coal, peat and wood during gasification: Literature review. *Fuel Process. Tech.* **1995,** *43* (1), 1-45.

3. Torres, W.; Pansare, S. S.; Goodwin Jr, J. G., Hot gas removal of tars, ammonia, and hydrogen sulfide from biomass gasification gas. *Catal. Rev.* **2007,** *49* (4), 407-456.

4. Cal, M.; Strickler, B.; Lizzio, A., High temperature hydrogen sulfide adsorption on activated carbon: I. Effects of gas composition and metal addition. *Carbon* **2000,** *38* (13), 1757-1765.

5. Habibi, R.; Rashidi, A. M.; Daryan, J. T., Study of the Rod-Like and spherical nano-ZnO morphology on H_2S removal from natural gas. *Appl. Surf. Sci.* **2010,** *257* (2), 434-439.

6. Meng, X.; De Jong, W.; Pal, R.; Verkooijen, A. H., In bed and downstream hot gas desulphurization during solid fuel gasification: A review. *Fuel Process. Tech.* **2010,** *91* (8), 964-981.

7. Tüysüz, H.; Salabaş, E. L.; Bill, E.; Bongard, H.; Spliethoff, B.; Lehmann, C. W.; Schüth, F., Synthesis of hard magnetic ordered mesoporous $Co_3O_4/CoFe_2O_4$ nanocomposites. *Chem. Mater.* **2012,** *24* (13), 2493-2500.

8. Wang, G.; Liu, H.; Horvat, J.; Wang, B.; Qiao, S.; Park, J.; Ahn, H., Highly ordered mesoporous cobalt oxide nanostructures: synthesis, characterisation, magnetic properties, and applications for electrochemical energy devices. *Chem. Eur. J.* **2010,** *16* (36), 11020-11027.

9. Chen, C. H.; Abbas, S. F.; Morey, A.; Sithambaram, S.; Xu, L. P.; Garces, H. F.; Hines, W. A.; Suib, S. L., Controlled synthesis of self-assembled metal oxide hollow spheres via tuning redox potentials: versatile nanostructured cobalt oxides. *Adv. Mater.* **2008,** *20* (6), 1205-1209.

10. Tian, B.; Liu, X.; Solovyov, L. A.; Liu, Z.; Yang, H.; Zhang, Z.; Xie, S.; Zhang, F.; Tu, B.; Yu, C., Facile synthesis and characterization of novel mesoporous and mesorelief oxides with gyroidal structures. *J. Am. Chem. Soc.* **2004,** *126* (3), 865-875.

11. Rouquerol, J.; Avnir, D.; Fairbridge, C.; Everett, D.; Haynes, J.; Pernicone, N.; Ramsay, J.; Sing, K.; Unger, K., Recommendations for the characterization of porous solids (Technical Report). *Pure Appl. Chem.* **1994,** *66* (8), 1739-1758.

12. Ryoo, R.; Joo, S. H.; Jun, S., Synthesis of highly ordered carbon molecular sieves via template-mediated structural transformation. *J. Phys. Chem. B* **1999,** *103* (37), 7743-7746.

13. Poyraz, A. S.; Kuo, C.-H.; Biswas, S.; King'ondu, C. K.; Suib, S. L., A general approach to crystalline and monomodal pore size mesoporous materials. *Nat. Commun.* **2013,** *4*, 3952.

14. Chung, J. B.; Chung, J. S., Desulfurization of H_2S using cobalt-containing sorbents at low temperatures. *Chem. Eng. Sci.* **2005,** *60* (6), 1515-1523.

15. Westmoreland, P. R.; Harrison, D. P., Evaluation of candidate solids for high-temperature desulfurization of low-Btu gases. *Environ. Sci. Technol.* **1976,** *10* (7), 659-661.

16. Meng, X.; De Jong, W.; Verkooijen, A., Thermodynamic analysis and kinetics model of H_2S sorption using different sorbents. *Environ. Prog. Sustainable Energy* **2009,** *28* (3), 360-371.

17. Ko, T.-H.; Chu, H.; Liou, Y.-J., A study of Zn–Mn based sorbent for the high-temperature removal of H_2S from coal-derived gas. *J. Hazard. Mater.* **2007,** *147* (1), 334-341.

18. Garces, H. F.; Galindo, H. M.; Garces, L. J.; Hunt, J.; Morey, A.; Suib, S. L., Low temperature H_2S dry-desulfurization with zinc oxide. *Microporous Mesoporous Mater.* **2010,** *127* (3), 190-197.

19. Samokhvalov, A.; Tatarchuk, B. J., Characterization of active sites, determination of mechanisms of H_2S, COS and CS_2 sorption and regeneration of ZnO low-temperature sorbents: past, current and perspectives. *Phys. Chem. Chem. Phys.* **2011,** *13* (8), 3197-3209.

20. Pahalagedara, L. R.; Poyraz, A. S.; Song, W.; Kuo, C.-H.; Pahalagedara, M. N.; Meng, Y.-T.; Suib, S. L., Low temperature desulfurization of H_2S: High sorption capacities by mesoporous cobalt oxide via increased H_2S diffusion. *Chem. Mater.* **2014,** *26* (22), 6613-6621.

21. Tian, Z.-R.; Tong, W.; Wang, J.-Y.; Duan, N.-G.; Krishnan, V. V.; Suib, S. L., Manganese oxide mesoporous structures: mixed-valent semiconducting catalysts. *Science* **1997,** *276* (5314), 926-930.

22. Jiao, F.; Jumas, J.-C.; Womes, M.; Chadwick, A. V.; Harrison, A.; Bruce, P. G., Synthesis of ordered mesoporous Fe_3O_4 and γ-Fe_2O_3 with crystalline walls using post-template reduction/oxidation. *J. Am. Chem. Soc.* **2006,** *128* (39), 12905-12909.

23. Yu, B. Y.; Kwak, S.-Y., Assembly of magnetite nanocrystals into spherical mesoporous aggregates with a 3-D wormhole-like pore structure. *J. Mater. Chem.* **2010,** *20* (38), 8320-8328.

24. Poyraz, A. S.; Hines, W. A.; Kuo, C.-H.; Li, N.; Perry, D. M.; Suib, S. L., Mesoporous Co_3O_4 nanostructured material synthesized by one-step soft-templating: A magnetic study. *J. Appl. Phys.* **2014,** *115* (11), 114309.

25. Brundle, C.; Chuang, T.; Wandelt, K., Core and valence level photoemission studies of iron oxide surfaces and the oxidation of iron. *Surf. Sci.* **1977,** *68*, 459-468.

26. Shen, T.; Weissleder, R.; Papisov, M.; Bogdanov, A.; Brady, T. J., Monocrystalline iron oxide nanocompounds (MION): physicochemical properties. *Magn. Reson. Med.* **1993,** *29* (5), 599-604.

27. Kim, D.; Zhang, Y.; Voit, W.; Rao, K.; Muhammed, M., Synthesis and characterization of surfactant-coated superparamagnetic monodispersed iron oxide nanoparticles. *J. Magn. Magn. Mater.* **2001,** *225* (1), 30-36.

28. Park, J.; Lee, E.; Hwang, N. M.; Kang, M.; Kim, S. C.; Hwang, Y.; Park, J. G.; Noh, H. J.; Kim, J. Y.; Park, J. H., One-nanometer-scale size-controlled synthesis of monodisperse magnetic iron oxide nanoparticles. *Angew. Chem. Int. Ed.* **2005,** *117* (19), 2932-2937.

29. Speliotis, D., Magnetic recording beyond the first 100 years. *J. Magn. Magn. Mater.* **1999,** *193* (1), 29-35.

30. Leslie-Pelecky, D. L.; Rieke, R. D., Magnetic properties of nanostructured materials. *Chem. Mater.* **1996,** *8* (8), 1770-1783.

31. Tan, Y.; Zhuang, Z.; Peng, Q.; Li, Y., Room-temperature soft magnetic iron oxide nanocrystals: synthesis, characterization, and size-dependent magnetic properties. *Chem. Mater.* **2008,** *20* (15), 5029-5034.

32. Raj, K.; Moskowitz, R., Commercial applications of ferrofluids. *J. Magn. Magn. Mater.* **1990,** *85* (1-3), 233-245.

33. Hergt, R.; Andra, W.; d'Ambly, C. G.; Hilger, I.; Kaiser, W. A.; Richter, U.; Schmidt, H.-G., Physical limits of hyperthermia using magnetite fine particles. *IEEE Transactions on Magnetics* **1998,** *34* (5), 3745-3754.

34. Jordan, A.; Scholz, R.; Wust, P.; Fähling, H.; Felix, R., Magnetic fluid hyperthermia (MFH): Cancer treatment with AC magnetic field induced excitation of biocompatible superparamagnetic nanoparticles. *J. Magn. Magn. Mater.* **1999,** *201* (1), 413-419.

35. Banerjee, S. K.; Moskowitz, B. M., Ferrimagnetic properties of magnetite. *Magnetite biomineralization and magnetoreception in organisms*, Springer: **1985**, 17-41.

36. Lu, A. H.; Salabas, E. e. L.; Schüth, F., Magnetic nanoparticles: synthesis, protection, functionalization, and application. *Angew. Chem. Int. Ed.* **2007,** *46* (8), 1222-1244.

37. Dormann, J. L.; Fiorani, D.; Tronc, E., Magnetic relaxation in fine-particle systems. *Adv. Chem. Phys.* **1997**, 98, 283-494.

38. Majetich, S.; Sachan, M., Magnetostatic interactions in magnetic nanoparticle assemblies: energy, time and length scales. *J. Phys. D: Appl. Phys.* **2006,** *39* (21), R407.

39. Steijns, M.; Derks, F.; Verloop, A.; Mars, P., The mechanism of the catalytic oxidation of hydrogen sulfide: II. Kinetics and mechanism of hydrogen sulfide oxidation catalyzed by sulfur. *J. Catal.* **1976,** *42* (1), 87-95.

40. Adib, F.; Bagreev, A.; Bandosz, T. J., Effect of pH and surface chemistry on the mechanism of H_2S removal by activated carbons. *J. Colloid. Interface. Sci.* **1999,** *216* (2), 360-369.

41. Slimane, R. B.; Abbasian, J., Utilization of metal oxide-containing waste materials for hot coal gas desulfurization. *Fuel Process. Tech.* **2001,** *70* (2), 97-113.

42. Jung, S. Y.; Lee, S. J.; Park, J. J.; Lee, S. C.; Jun, H. K.; Lee, T. J.; Ryu, C. K.; Kim, J. C., The simultaneous removal of hydrogen sulfide and ammonia over zinc-based dry sorbent supported on alumina. *Sep. Purif. Tech.* **2008,** *63* (2), 297-302.

43. Yang, H.; Cahela, D. R.; Tatarchuk, B. J., A study of kinetic effects due to using microfibrous entrapped zinc oxide sorbents for hydrogen sulfide removal. *Chem. Eng. Sci.* **2008,** *63* (10), 2707-2716.

44. Wang, X.; Sun, T.; Yang, J.; Zhao, L.; Jia, J., Low-temperature H_2S removal from gas streams with SBA-15 supported ZnO nanoparticles. *Chem. Eng. J.* **2008,** *142* (1), 48-55.

45. Gibson, J. B.; Harrison, D. P., The reaction between hydrogen sulfide and spherical pellets of zinc oxide. *Ind. Eng. Chem. Process Des. Dev.* **1980,** *19* (2), 231-237.

46. Lew, S.; Jothimurugesan, K.; Flytzani-Stephanopoulos M., High-temperature H_2S removal from fuel gases by regenerable zinc oxide-titanium dioxide sorbents. *Ind. Eng. Chem. Res.* **1989,** *28* (5), 535-541.

47. Woods, M. C.; Gangwal, S. K.; Harrison, D. P., Kinetics of the reactions of a zinc ferrite sorbent in high-temperature coal gas. *Ind. Eng. Chem. Res.* **1991,** *30* (1), 100-107.

48. Bakker, W. J.; Kapteijn, F.; Moulijn, J. A., A high capacity manganese-based sorbent for regenerative high temperature desulfurization with direct sulfur production: Conceptual process application to coal gas cleaning. *Chem. Eng. J.* **2003,** *96* (1), 223-235.

49. Wang, Z.; Flytzani-Stephanopoulos, M., Cerium oxide-based sorbents for regenerative hot reformate gas desulfurization. *Energy & Fuels* **2005,** *19* (5), 2089-2097.

50. Kobayashi, M.; Shirai, H.; Nunokawa, M., High-temperature sulfidation behavior of reduced zinc ferrite in simulated coal gas revealed by in situ X-ray diffraction analysis and Mössbauer spectroscopy. *Energy & Fuels* **2002,** *16* (3), 601-607.

51. Zhang, R.; Huang, J.; Zhao, J.; Sun, Z.; Wang, Y., Sol−gel auto-combustion synthesis of zinc ferrite for moderate temperature desulfurization. *Energy & Fuels* **2007,** *21* (5), 2682-2687.

CHAPTER 2. CHARACTERIZATION METHODS

2.1 X-ray diffraction (XRD)

Both low-angle X-ray diffraction (LAXD) and wide-angle powder X-ray diffraction (PXRD) patterns were obtained at room temperature using a Rigaku Ultima IV diffractometer with Cu $K\alpha_1$ radiation (λ = 0.15406 nm). The porous structure of the samples was analyzed using a low-angle step width of 0.05º with an acquisition time of 0.01s per step in the range 2θ = 0.5º to 8º for the LAXD data. The center-to-center distance of the close-packed particles can be calculated by Bragg's law: $n\lambda = 2\ d \sin\theta$, where λ is the wave length of the X-ray, d is identifying the pore diameter.

The data collected for the wide-angle PXRD were in the range 2θ = 5º to 75º with scanning rates ranging from 0.2º/min to 2º/min, an operating voltage of 40 kV, and a current of 44 mA. Comparing the diffraction pattern with the standard PDF pattern, the crystalline phase of the samples will be indicated. According to the Sherrer equation: $D = 0.89\ \lambda / \beta \cos\theta$, the crystalline size can be calculated, where β is the full width at half maximum of the peak and θ is the peak position.

2.2 N_2 physisorption

Nitrogen sorption isotherms were measured with a NOVA 2000e system at liquid nitrogen temperature. Prior to the measurement, the sample was degassed at a temperature of 120 ºC for 8 hrs. The total pore volume was determined using the adsorption volume at a relative pressure of 0.9918. A Brunauer-Emmett-Teller (BET)[1] surface area was estimated from the adsorption data

in the relative pressure range p/p_o = 0.05 to 0.3. The mesopore size distribution was calculated from the desorption branch of the isotherm using the Barrett-Joyner-Halenda (BJH)[2] method.

2.3 Scanning electron microscopy (SEM)

The morphology of the final sample was characterized using an FEI Nova NanoSEM 450 variable pressure field emission scanning electron microscope (FESEM) in **Chapter 3 and 4**. In **Chapter 5**, the SEM images were carried out by FEI TENEO Low Vacuum SEM. The sample was prepared on a carbon tape or a silicon wafer supported by a stub holder.

2.4 Transmission electron microscopy (TEM)

Transmission electron microscopy (TEM), high resolution transmission electron microscopy (HRTEM), and selected area electron diffraction (SAED) images in **Chapter 3** were obtained with a JEOL 2010 FasTEM operating at 200 kV. In **Chapter 4 and 5**, HRTEM and scanning transmission electron microscopy (STEM) measurements were carried out using a Talos F200X microscope operating at 200 kV equipped with an energy dispersive X-ray spectroscopy (EDS) detector. The sample was dispersed in ethanol and one drop of the homogeneous-like solution was placed on a QUANTIFOIL® TEM grid. The grid was dried in air and then used for the TEM studies.

2.5 Superconductor quantum interfere device (SQUID)

Measurements of the DC magnetization were carried out for magnetic fields $-50\ \text{kOe} \leq H \leq +50\ \text{kOe}$ over the temperature range $5.0\ \text{K} \leq T \leq 350\ \text{K}$ using a Quantum Design MPMS-5 SQUID magnetometer. 5 mg sample were packed in the plastic sample holder with the cotton plug-in. The sample holder was stuck in a transparent straw to attach with the magnetometer probe.

The sample would be automatically adjusted to the center of the field by the program. The empty sample holder with the cotton plug-in was measured under the same condition for the background substrate.

2.6 Small angle X-ray scattering (SAXS)

Small-angle X-ray scattering (SAXS) measurements were carried out on a Bruker NanoSTAR instrument. The X-rays were generated by a Turbo (rotating anode) X-ray source (TXS). A Cu Kα wavelength $\lambda = 0.15418$ nm was selected using a Göble mirror. The X-ray beam was collimated by two scatterless pinholes with a diameter of 350 μm. The data were recorded on a 2-D MikroGap VANTEC-2000 detector with a sample-to-detector distance of 106.5 cm, in order to include a scattering vector $q = (4\pi/\lambda) \sin \theta$ range of 0.071/nm to 2.276/nm, where 2θ is the scattering angle. The 2-D SAXS data were corrected for empty-cell background, sample transmission, and empty-cell transmission. The 1-D data were obtained by integration of the 2-D data. The sample was sealed between two pieces of Kapton tape and mounted on the sample holder. The empty Kapton tape was measured under the same condition for the background subtraction.

2.7 X-ray photon spectrum (XPS)

The X-ray photoelectron spectroscopy (XPS) analysis was done with a PHI model 590 spectrometer with multiprobes (Φ Physical Electronics Industries Inc.). The radiation source was Al-Kα radiation with $\lambda = 1486.6$ eV. The sample was prepared on a carbon tape supported by a stub holder. The survey spectrum and high resolution spectrum of the specific elements were collected for each sample. Carbon spectra were collected for calibration.

2.8 Nuclear magnetic resonance (NMR)

Zero-field NMR ^{57}Fe spin-echo nuclear magnetic resonance (NMR) spectra were obtained over the frequency range from ν = 66.0 MHz to 76.0 MHz using a Matec model 7700 pulsed-oscillator mainframe and model 760 pulsed-oscillator/receiver, with the sample in a tuned circuit that was matched to 50 Ω. The NMR echo amplitude was optimized using a standard τ_{p1}-τ-τ_{p2} spin-echo pulse sequence with τ_{p1}, τ_{p2} = 4.0 μs rf pulses, a pulse separation of τ = 20 μs, and a repetition rate of 33 Hz. Spectra were obtained by averaging the NMR signals 500 to 1,000 times at 0.25 MHz intervals across the frequency range. A resolution of 0.25 MHz is consistent with the 4.0 μs rf pulses. Spin-echo NMR spectra were obtained at T = 4.2 K with $0 \leq H \leq 7.5$ kOe. The NMR sensitivity of the spectrometer (including the $1/\nu^2$ correction) was monitored over the entire frequency range by injecting an RF calibration pulse signal using a 50 Ω antenna. Measurements of the spin-spin relaxation time T_2 were made at selected frequencies across the spectrum by varying the pulse separation time from τ = 20 μs to 450 μs. As discussed below, the frequency dependence of T_2 can result in a significant correction to the NMR spectrum[3]. Operation at liquid He temperature was carried out using a conventional glass double dewar system.

2.9 Reference

1. Brunauer, S.; Emmett, P. H.; Teller, E., Adsorption of gases in multimolecular layers. *J. Am. Chem. Soc.* **1938,** *60*, 309-319.

2. Barrett, E. P.; Joyner, L. G.; Halenda, P. P., The determination of pore volume and area distributions in porous substances: I. Computations from nitrogen isotherms. *J. Am. chem. soc* **1951,** *73* (1), 373-380.

3. Hines, W.; Budnick, J.; Perry, D.; Majetich, S.; Booth, R.; Sachan, M., Nuclear magnetic resonance and magnetization study of surfactant-coated epsilon-Co nanoparticles. *Phys. Status Solidi B* **2011,** *248* (3), 741-747.

CHAPTER 3. Magnetic Studies of Mesoporous Nanostructured Iron Oxide Materials Synthesized by One-Step Soft-Templating

3.1 Introduction

Currently, there is intense interest in mesoporous nanostructured materials because of their wide spread technological applications such as adsorption, gas storage, separation, catalysis, drug delivery, and electrochemistry[1-4]. All these applications benefit from the high specific surface area and suitable pore volume of the ordered nanostructure. These materials provide model systems for basic scientific studies as well.

The transition metal oxides in a mesoporous nanostructure have localized d-electrons within the thin walls between pores and, therefore, the materials are endowed with unusual magnetic, semiconducting, electrical, and optical properties[5-7]. The magnetic properties, coupled with the catalytic properties, provide the opportunity for additional applications using the new materials. In particular, iron oxides with magnetic ordering and relatively large magnetization at room temperature have already found application in high-density magnetic storage, ferrofluids, and the biomedical area[9]. A number of reports on the synthesis, characterization, and magnetic properties of iron oxide nanoparticles have been published in the past decade[10-12].

General speaking, there are two methods to synthesize mesoporous nanostructured materials. They are the hard template (nanocasting) method and the soft template (cooperative assembly) method. In the hard template procedure, introduced by Rhoo and co-workers[13], the silicas MCM-41, SBA-15, and KIT-6, are used as molds and then dissolved afterwards. For the soft template procedure, the mesoporous solid is assembled by using a surfactant. However, the

soft template method is problematic in fabricating mesoporous transition metal oxide nanostructures because the surfactant/oxide composite precursors are often more susceptible to lack of condensation, redox reactions, or phase transitions accompanied by thermal breakdown of the structure[14].

The mesoporous nanostructured iron oxides in this work were synthesized using a recently developed one-step soft-templating procedure, which consists of an inverse micelle packing approach[15-16]. This method allows one to synthesize a variety of thermally-stable mesoporous oxides including transition metals (e.g., Ti, Zr, Nb, Hf, Cr, Fe, Mn, Ni, and Co), metalloids (e.g., Si), post-transition metals (e.g., Sn), non-metals (e.g., C), lanthanides (e.g., Ce, Nd, Sm, and Gd), as well as various mixed oxides (e.g., aluminosilicates, YSZ). This approach makes it possible to synthesize mesoporous materials with tunable mesostructure, mesoporosity, and nanocrystallinity. The facile one-step synthesis also shortens the reaction time to obtain the mesoporous structures of iron oxides with removable surfactant template and high repeatability. The crystal structure, particle size, pore topology, and sample morphology are examined using X-ray diffraction/scattering, electron microscopy, and N_2 sorption techniques. A detailed description of the magnetic moment, magnetic interactions, and blocking temperature, obtained through SQUID magnetometry, is presented in this work. ^{57}Fe spin-echo nuclear magnetic resonance (NMR) has been used to map the hyperfine distribution which provides a local probe of the microscopic atomic and electronic structure. In particular, NMR spectra are used to distinguish the crystallographically similar iron oxide phases in the nanostructured materials.

3.2 Synthesis method

Two series of mesoporous nanostructured iron-oxide materials, consisting of the Fe_3O_4 and γ-Fe_2O_3 phases, were synthesized using a procedure based on the recently-developed one-step soft-templating approach described above[15]. Reagent-grade chemicals were used in the synthesis. Pluronic P123 copolymer surfactant (PEO_{20}-PPO_{70}-PEO_{20}), 1-butanol (anhydrous, 99.8%), and iron (III) nitrate nonahydrate $Fe(NO_3)_3 \cdot 9H_2O$ were purchased from Sigma-Aldrich. Concentrated nitric acid (68%-70% HNO_3) was purchased from J. T. Baker. The starting material for the first series of three mesoporous (nominally γ-Fe_2O_3) samples was synthesized by dissolving 4.04 g (0.010 mol) of $Fe(NO_3)_3 \cdot 9H_2O$ in 8.9 g (0.12 mol) of 1-butanol solution containing 1.2 g (2.04×10^{-4} mol) of P123 and 1.2 g (0.019 mol) of concentrated HNO_3. A clear red-brown gel was obtained after magnetically stirring the above-mentioned solution at room temperature for 4 hrs. The gel was placed in an oven and maintained at 90 ºC for 2 hr. The resulting fine powder was washed twice with ethanol, centrifuged, and dried in a vacuum jar overnight. The dry powder was heated to 150 ºC for 6 hrs and then cooled down naturally to room temperature.

The starting material was separated into three portions after the 150 ºC heat treatment. Variations in temperature and time were explored. The three portions of first series starting material were calcined at 250 ºC, 300 ºC, and 350 ºC (heating rate = 10 ºC/min) for 3 hrs individually in air atmosphere. Preliminary results in earlier work indicated that the above calcination procedure yielded the γ-Fe_2O_3 phase. In the following discussion, these three samples will be denoted by the calcination temperature (i.e., 250 ºC, 300 ºC, and 350 ºC). The starting material for the second series of three mesoporous (nominally Fe_3O_4) samples was synthesized following the above procedure while maintaining the same ratio of the four constituents. Again, the starting material was separated into three portions after the 150 ºC heat treatment. The three

portions of second series starting material were heated at 250 ºC (heating rate = 10 ºC/min) for 3 hrs individually in 5% H_2 – 95% Ar, 10% H_2 – 90% Ar, and 20% H_2 – 80% Ar atmospheres. Using a H_2−Ar atmosphere instead of air during heat treatment has been shown previously to yield the Fe_3O_4 phase[6]. In the following discussion, these three samples will be denoted by the H_2 percentage (i.e., 5% H_2, 10% H_2, and 20% H_2).

In the one-step soft-templating synthesis procedure used here, the surfactant species are oxidized at long reaction times and form carboxyl groups nitrate. Temperature programmed desorption (TPD) has been used previously to monitor their removal during the 150 ºC heat treatment.[15]

For comparison, commercial lab grade magnetite (Fe_3O_4) and maghemite (γ-Fe_2O_3) were used as macrocrystalline or "bulk" standards: (1) "Fe_3O_4, 99.99%, lot #518158"; (2) "Fe_3O_4, < 5 μm, 95%, lot #310069"; and (3) "γ-Fe_2O_3, < 5 μm, > 99%, lot #310050". All of the materials were purchased from Sigma-Aldrich.

3.3 Results

3.3.1 Characterization

A typical ordered mesoporous nanostructured material is characterized by: (1) small-angle X-ray diffraction peak(s), indicating the existence of a "long-range", "periodic" mesostructure and (2) a Type IV N_2 sorption isotherm with H1 hysteresis, indicating a regular nanosized pore structure[15]. **Figures 3.1a and 3.1b** show the small-angle X-ray diffraction (SAXD) and wide-angle X-ray diffraction (PXRD) patterns, respectively, for the three first series (nominally γ-Fe_2O_3) of mesoporous samples which were calcined at 250 ºC, 300 ºC, and 350 ºC for 3 hrs. Each SAXD

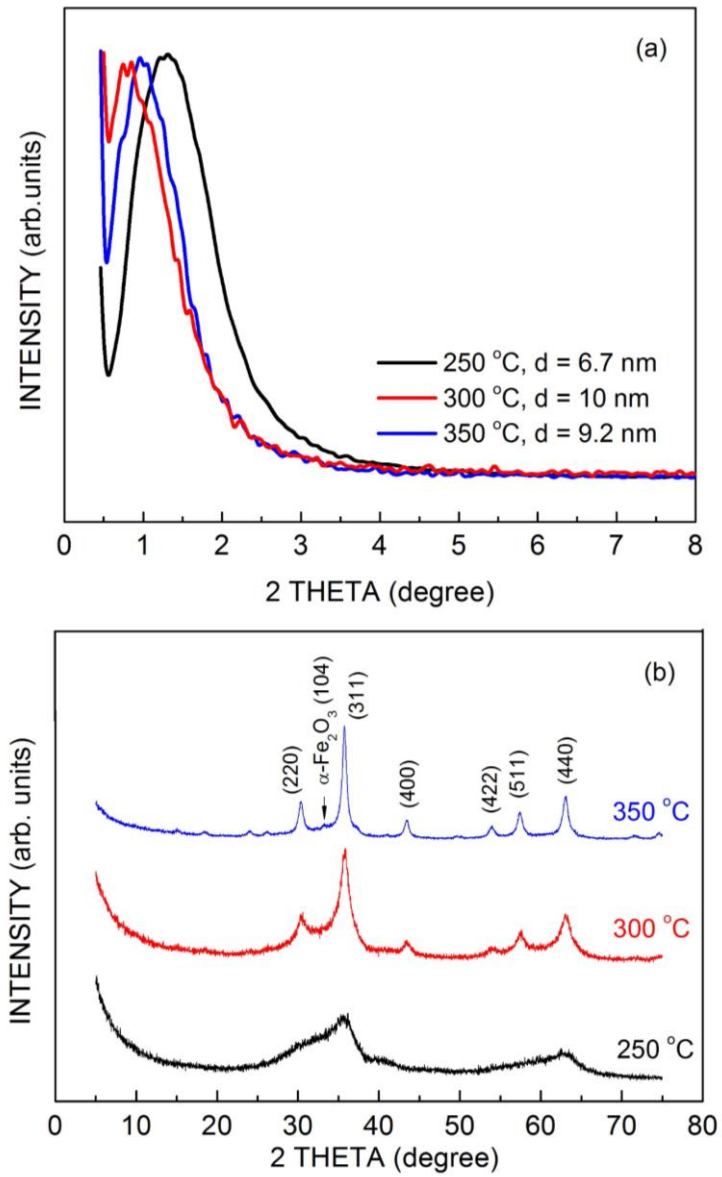

Figure 3.1. (Color Online) (a) Small-angle and (b) wide-angle XRD patterns, respectively, for the three (first series) mesoporous nanostructured samples calcined at 250 °C, 300 ºC, and 350 ºC for 3 hrs. The low-angle pattern shows a single peak characteristic of the mesostructure; the peak position, which defines the "periodic" order, gives a measure of the nanoparticle diameter. The wide-angle pattern is consistent with the spinel γ-Fe_2O_3 crystalline phase; cubic unit cell with Fd−3m space group (JCPDS no. 04-0755)[8].

pattern is characterized by a single broad peak; the peak shifting to lower angle with increasing calcination temperature. A peak shift to smaller angle with increasing heat treatment temperature or time is typical for UCT materials and indicates an expansion of the mesoporous structure[15-16]. This is in contrast to traditional mesoporous materials in which the mesostructure shrinks with heat treatment. As discussed below, the mesoporous structure is formed by a random close-packed aggregation of nanoparticles having similar size and not an iron oxide framework. Consequently, the small-angle peak position (2θ) has been related to the average particle diameter D[15-16].

The small-angle peak in **Figure 3.1a** is a consequence of the order associated with the mesoporous structure, i.e., the pore center-to-center correlation distance[17]. Using Bragg's law, $n\lambda = 2d \sin\theta$, to calculate the d-spacing value and assuming a random close-packing of the particles, an estimate is obtained for the average particle diameter, $D \approx d$. From the peak positions in **Figure 3.1a**, values of $D \approx d$ = 6.7 nm, 10 nm, and 9.2 nm are obtained from the samples calcined at 250 ºC, 300 ºC, and 350 ºC for 3 hrs, respectively. (As discussed below, the calcination temperature/time resulted in some degradation of the 350 ºC sample mesostructure.)

The wide-angle PXRD patterns in **Figure 3.1b** for the three samples have reduced signal-to-noise due to the small particle size (vanishing XRD peaks due to small grain size is sometimes referred to as "XRD amorphous" in the literature[15]) and this will be discussed later. Nevertheless, the few peaks which are observed are consistent with the γ-Fe_2O_3 phase, i.e., a cubic unit cell with the Fd−3m space group and an accepted lattice parameter a_o = 0.8350 nm (JCPDS no. 04-0755)[8]. It is quite difficult to distinguish between γ-Fe_2O_3 and Fe_3O_4 using PXRD because these two magnetic spinel phases are structurally very similar. The situation is even more difficult in the case of nanoparticles, where the Bragg peaks are broadened. Using the Scherrer equation D =

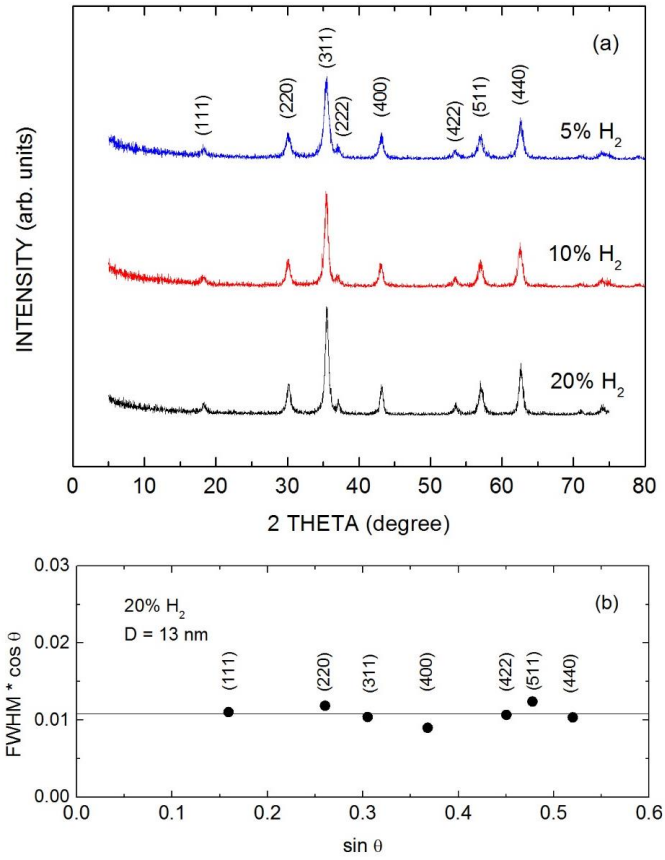

Figure 3.2. (a) Wide-angle PXRD patterns for the three (second series) mesoporous nanostructured samples heated at 250 ºC for 3 hrs in 5% H_2, 10% H_2, and 20% H_2 atmospheres, and (b) (expanded) Scherrer equation analysis for the grain size in the 20% H_2 sample. The wide-angle pattern is consistent with the spinel Fe_3O_4 crystalline phase; cubic unit cell with Fd−3m space group (JCPDS no. 85-1436)[8].

$0.89\lambda/(\beta \cos \theta)$, where D is the average grain size, β is the broadening of the (311) reflection (see **Figure 1b**), and $\lambda = 0.15406$ nm, estimates of D = 4.3 nm, and 13 nm are obtained for the 300 ºC and 350 ºC (nominally γ-Fe_2O_3) samples, respectively. An estimate of the grain size was not possible for the 250 ºC sample. **Figure 3.2a** shows the wide-angle X-ray diffraction (PXRD) patterns for the three second series (nominally Fe_3O_4) mesoporous samples which were heated in 5% H_2, 10% H_2, and 20% H_2 atmospheres. **Figure 3.2b** shows the (expanded) Scherrer equation analysis for the 20% H_2 sample; a similar analysis was carried out for both the 5% H_2 and 10% H_2

samples (not shown). Due to the larger particle size for these three samples, the LAXD peaks occur below the 0.5º lower limit for the diffractometer. From the Scherrer equation analysis as illustrated in **Figure 3.2b**, values of D = 9.9 nm, 12 nm, and 13 nm were obtained for the 5% H_2, 10% H_2, and 20% H_2 samples, respectively (see **Table 3.1**).

Table 3.1 Characterization Results

Sample	PXRD Grain Size (nm)	SAXD Particle Size (nm)	SAXS Particle Size (nm)	HR-TEM particle Size (nm)	N_2 sorption BET Surface Area (m^2/g)	BJH Pore Size Desorption (nm)	Phase Identi-fication NMR
(250 ºC)[1]	NA[3]	6.7	5.7	NA[4]	240	(≤ 5)[3]	NA[4]
(300 ºC)[1]	4.3	10	10	12~18	223	(≤ 5)[3]	γ-Fe_2O_3
(350 ºC)[1]	13	9.2	18	NA[4]	114	NA[2]	NA[4]
(5% H_2)[2]	9.9	NA[1]	22	NA[4]	67	9.1	NA[4]
(10% H_2)[2]	12	NA[1]	26	NA[4]	50	9.1	NA[4]
(20% H_2)[2]	13	NA[1]	30	17~23	243	16	Fe_3O_4 + γ-Fe_2O_3

[1]Sample designation based on calcination temperature in air for 3 hrs.

[2]Sample designation based on calcination atmosphere at 250 ºC for 3 hrs.

[3]Upper limit due to N_2 adsorptive.

NA[1] not available, outside range of diffractometer.

NA[2] not available, Type H3 hysteresis.

NA[3] not available, "PXRD amorphous", peaks too broad to measure the FWHM.

NA[4] not available, selected measurements on 300 ºC and 20% H_2 samples only.

Figure 3.3 shows the 1-D SAXS profiles obtained by integration of the 2-D data for the three first series mesoporous samples which were calcined at 250 ºC, 300 ºC, and 350 ºC for 3 hrs. In order to bring out the structural features in **Figure 3.3**, a log-log plot is presented where q is the magnitude of the scattering vector, $q = (4\pi/\lambda) \sin \theta$ and 2θ is the scattering angle. As seen in the SAXS patterns, the "knee"-like feature shifts toward lower q with increased calcination temperature. A q^{-4} intensity decay is observed in the low q regime for the 250 ºC and 300 ºC

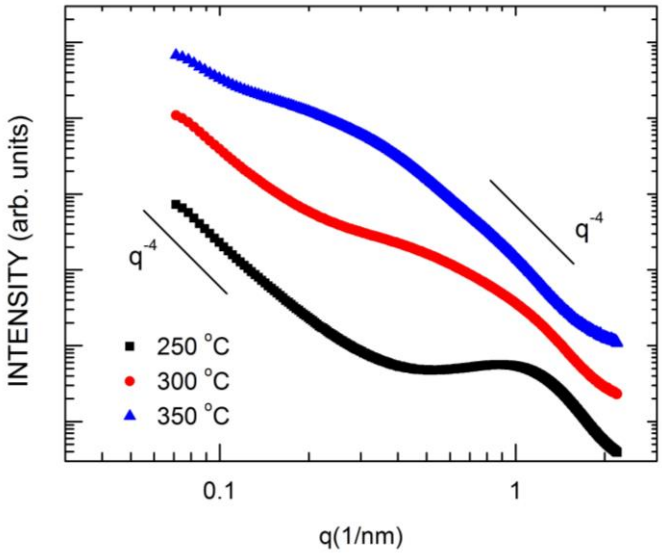

Figure 3.3. 1-D SAXS intensity profiles (log-log plots) obtained by integration of the 2-D data for the three (first series) mesoporous samples calcined at 250 ºC, 300 ºC, and 350 ºC for 3 hrs. The "knee"-like features yield estimates for the nanoparticle size (see text).

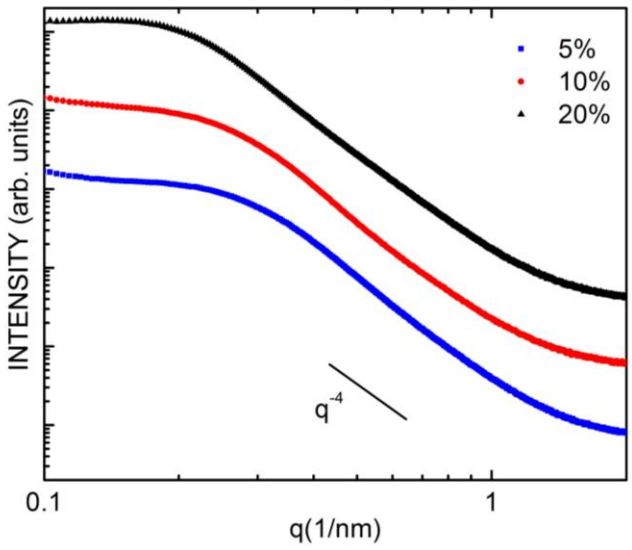

Figure 3.4. 1-D SAXS intensity profiles (log-log plots) obtained by integration of the 2-D data for the three (second series) mesoporous samples heated in 5% H_2, 10% H_2 and 20% H_2 atmospheres. The "knee"-like features yield estimates for the nanoparticle size (see text).

samples. This is indicative of the interfacial scattering (known as "Porod" scattering) from well-defined surfaces of large clusters presumably originating from the aggregation of γ-Fe_2O_3 nanoparticles[18]). SAXS data for the 350 ºC sample (blue curve in **Figure 3.3**) deviate from q^{-4} probably due to the proximity of the knee-like feature. In the high q regime (q > 1.5 nm), the intensity approaches a q^{-2} dependence for all three samples. As discussed below, the analysis of the SAXS data for these systems is complicated and problematic due to both form factor and structure factor contributions to the measured intensity q-dependence[19]. From the knee-like features shown in **Figure 3.3**, which occur at q = 0.35/nm, 0.63/nm, and 1.1/nm for the 350 ºC, 300ºC, and 250 ºC samples, respectively, corresponding estimates of 18 nm, 10 nm, and 5.7 nm are obtained for the particle size. Again, the shift of the peaks to lower q-values with increased calcination temperature indicates an increase in the nanoparticle size and, therefore, an expansion of the mesoporous structure. **Figure 3.4** shows the log-log SAXS intensity plots for the 5% H_2, 10% H_2, and 20% H_2 mesoporous samples. From the SAXS analysis, knee-like values (particle size values) of 0.28/nm (22 nm), 0.24/nm (26 nm), and 0.21/nm (30 nm) are obtained for the 5% H_2, 10% H_2, and 20% H_2 samples (see **Table 3.1**).

Figure 3.5 shows N_2 sorption isotherms for the three first series samples which were calcined at 250 ºC, 300 ºC, and 350 ºC for 3 hrs. For the 250 ºC and 300 ºC samples, the resulting isotherms are typical of a good mesoporous structure, i.e., Type IV according to the definitions provided by the IUPAC[20]. The isotherm for the 350 ºC sample also appears to be Type IV; however, the hysteresis behavior is clearly Type H3. The hysteresis behavior for the 250 ºC and 300 ºC samples appears to be intermediate between H1 and H3. A type IV isotherm is characterized by its hysteresis loop which is associated with capillary condensation taking place

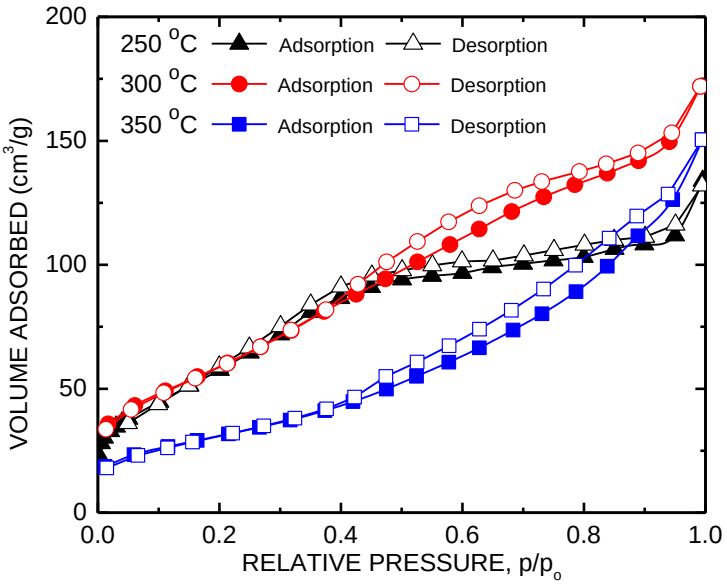

Figure 3.5. (Color Online) Nitrogen sorption isotherms for the three (first) series mesoporous samples calcined at 250 °C, 300 ºC, and 350 ºC for 3 hrs. The BET surface areas obtained from analysis of the isotherms are presented in **Table 3.1**. Unlike traditional mesoporous materials, the UCT materials expand with heat treatment.

in the mesopores. Type H1 hysteresis is typically associated with agglomerates of approximately spherical particles and cylindrical mesopores. The presence of Type H3 hysteresis indicates aggregates of elliptically-shaped particles resulting in (non-cylindrical) slit-like pores. Although the isotherms for the first series samples are Type IV, which is required for any reliable calculation of the mesopore size distribution; the existence of Type H3 hysteresis makes it unlikely that such a calculation will be meaningful, even for comparative purposes. For a detailed discussion of the above topics, the reader is referred to Ref. [20]. In **Figure 3.5**, it can be seen that, by increasing the calcination temperature from 250 ºC to 300 ºC, one obtains a shift of the adsorption step to a higher relative pressure value. This is a consequence of an increase in the mesopore size and consistent with the behavior of the LAXD and SAXS peaks described above. The mesopores are formed by interparticle voids and, hence, an increase in the nanoparticle size yields larger interparticle voids. The values ≤ 5 nm listed for the pore diameters of the two first series samples

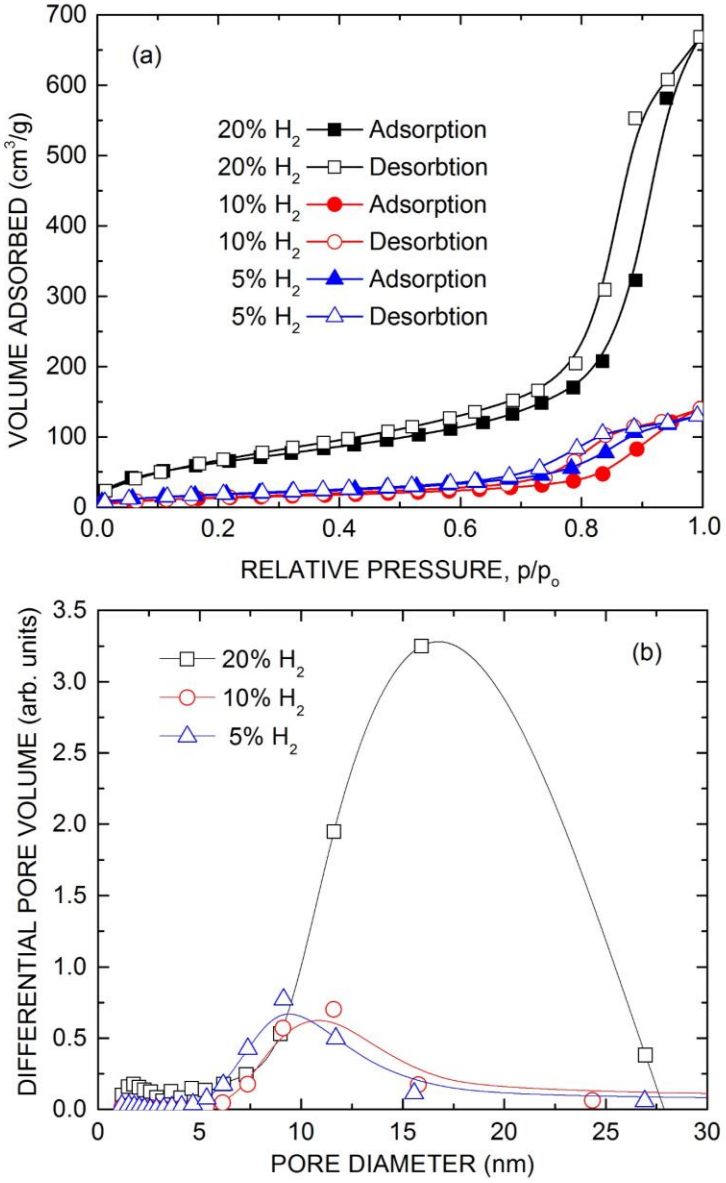

Figure 3.6. (Color Online) (a) Nitrogen sorption isotherms and (b) pore size distribution curves for the three (second) series mesoporous samples heated at 250 °C for 3 hrs in 5% H_2, 10% H_2, and 20% H_2 atmospheres. The BET surface areas and BJH pore sizes obtained from analysis of the isotherms are presented in **Table 3.1**. Unlike traditional mesoporous materials, the UCT materials expand with heat treatment.

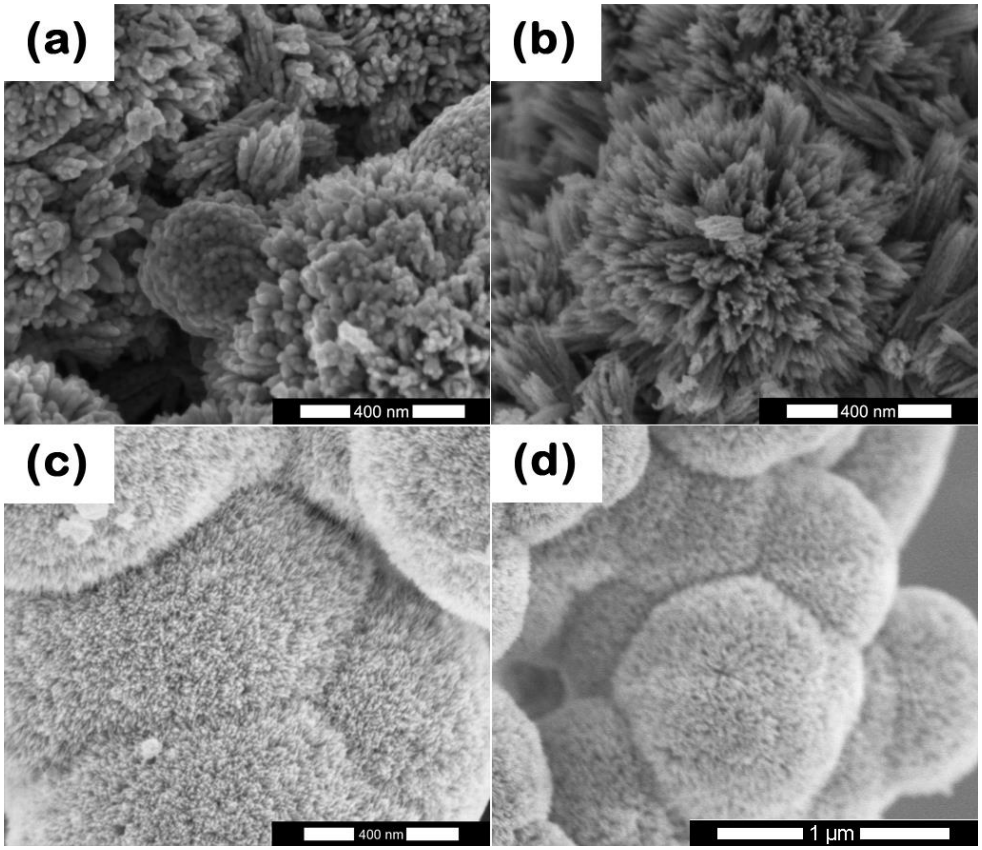

Figure 3.7. Scanning electron microscope images obtained from the three (first) series mesoporous samples: (a) 350 ºC sample - 400 nm scale bar (b) 300 ºC sample - 400 nm scale bar, (c) 250 ºC sample - 400 nm scale bar, and (d) 250 ºC sample - 1,000 nm scale bar. The overall sample morphology can be described as essentially spherical clusters with nanoscale segments.

in **Table 3.1** simply reflect the lower limit of hysteresis closure at $p/p_o \approx 0.4$ for nitrogen at its boiling point (77 K). Following IUPAC protocol[20], the BET values were obtained by the measurement of five points over a range within $0.05 \leq p/p_o \leq 0.3$ (see **Table 3.1**). **Figures 3.6a and 3.6b** show the N_2 sorption isotherms and pore size distribution curves, respectively, for the 5% H_2, 10% H_2, and 20% H_2 mesoporous samples. All three second series samples are characterized by Type IV sorption isotherms with H1 hysteresis indicating good mesoporous structures. The pore size distribution curves were calculated from the desorption branch using the BJH method[21]. The desorption branch was used as it seems to be preferred by most researchers in the literature. The BET surface area and BJH pore size values are summarized in **Table 3.1**.

The mesoporous structure was characterized by a combination of FESEM, TEM, and HRTEM. **Figures 3.7a, 3.7b, and 3.7c** show representative FESEM images with scale bars of 400 nm for the 350 ºC, 300 ºC, and 250 ºC samples, respectively. **Figure 3.7d** shows an image for the 250 ºC sample with a scale bar of 1,000 nm. The overall sample morphology can be described as essentially spherical clusters with nanoscale segments. For example, in the case of the 250 ºC sample, the clusters are approximately 1,000 nm in diameter. The size of the nanoscale pieces that compose the spherical clusters becomes larger with calcination temperature. **Figures 3.8a and 3.8b** show representative FESEM images for 5% H_2 and 20% H_2 mesoporous samples.

Further insight into the morphology and microstructure of the 300 ºC mesoporous material was obtained using TEM, HRTEM, and SAED. **Figures 3.9a and 3.9b** show representative TEM images with scale bars of 20 nm and 10 nm, respectively. The TEM images show that the clusters seen in the SEM images above consist of nanoparticles. Those nanoparticles exhibit polyhedral shape with the diameters of the particles ranging from 12 nm to 18 nm. The particle size estimates

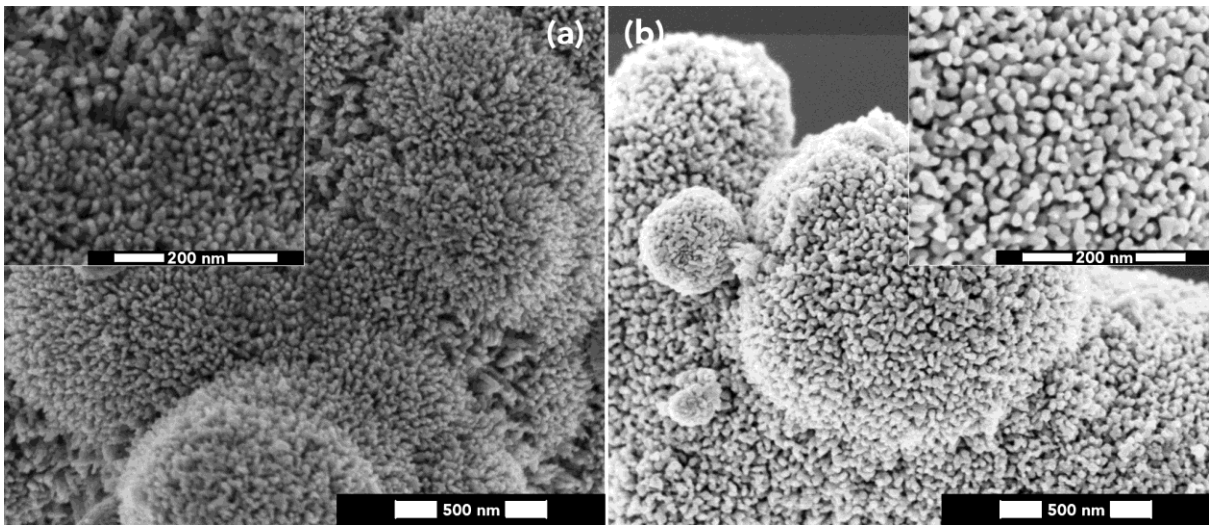

Figure 3.8. Scanning electron microscope images obtained from two of the three (second) series samples: (a) 5% H_2 sample - 500 nm scale bar (inset 200 nm) and (b) 20% H_2 sample - 500 nm scale bar (inset 200 nm). The overall sample morphology can be described as essentially spherical clusters with nanoscale segments.

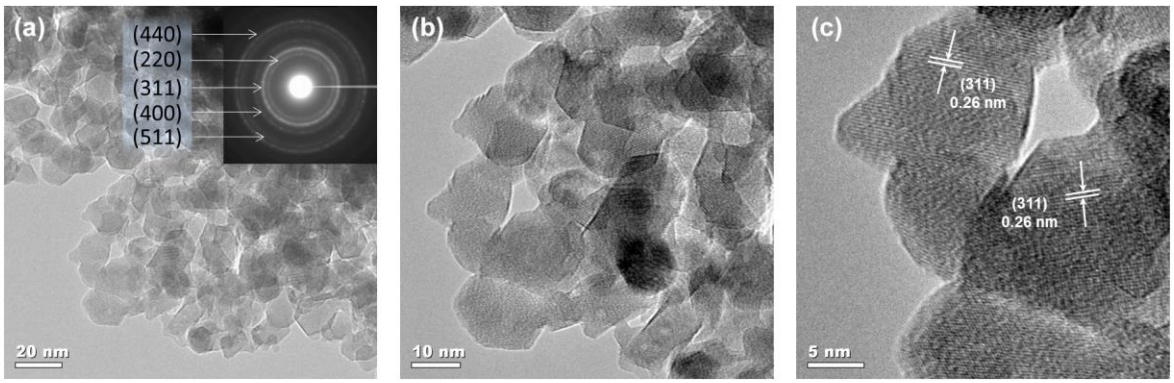

Figure 3.9. Transmission electron microscope images obtained from the mesoporous sample calcined at 300 ºC for 3 hrs: (a) TEM, 20 nm scale bar, (b) TEM, 10 nm scale bar, and (c) HRTEM, 5 nm scale bar. The inset in **Fig. 5a** shows a SAED pattern with Debye-Scherrer-type rings which can be indexed to the cubic spinel γ-Fe_2O_3 structure. The mesostructure consists of an assembly of nanoparticles with diameters ranging from 12 nm to 18 nm (see **Fig. 5b**). With high resolution (see **Fig. 5c**), the d-spacing of the resolved fringes is 0.26 nm, consistent with (311) planes for γ-Fe_2O_3.

from the TEM images are larger than the grain size values obtained from PXRD peaks using the Scherrer equation (≈ 4.3 nm for the 300 ºC sample). This would indicate that the majority of the nanoparticles are not single crystals. The nanoparticles are randomly close-packed to form the mesoporous morphology. As shown in **Figure 3.9c**, HRTEM images of the mesoporous 300 ºC

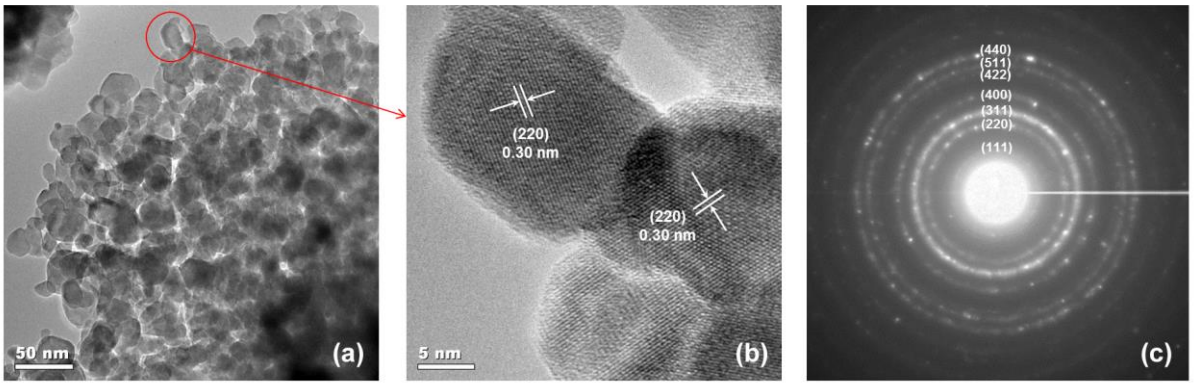

Figure 3.10. Transmission electron microscope images obtained from the sample heated at 250 ºC for 3 hrs in a 20% H_2 atmosphere: (a) TEM, 50 nm scale bar, (b) HRTEM, 5 nm scale bar, and (c) SAED pattern with Debye-Scherrer-type rings which can be indexed to the spinel Fe_3O_4 structure. The mesostructure consists of an assembly of nanoparticles with diameters ranging from 17 nm to 24 nm (see **Figure 3.10a**). With high resolution (see **Figure 3.10b**), the d-spacing of the resolved fringes is 0.30 nm, consistent with (200) planes for Fe_3O_4.

indicate the crystalline nature of the nanoparticles; the crystal orientation of the phase has no relationship with the orientation of the mesoporous network. Moreover, the visible lattice fringes with a lattice spacing of about 0.26 nm are characteristic of the (311) plane for the γ-Fe_2O_3 phase, which is consistent with the PXRD results. Again, due to the structural similarity, it is not possible to rule out the Fe_3O_4 phase. From SAED patterns (the inset of **Figure 3.9a**) obtained from larger areas of the mesoporous material, Debye-Scherrer-type rings are seen and can be indexed to the spinel γ-Fe_2O_3 structure. **Figures 3.10a, 3.10b, and 3.10c** show representative TEM, HRTEM, and SAED images, respectively, for the 20% H_2 sample. All the samples studied in this work, along with the corresponding characterization data, are summarized in **Table 3.1**.

3.3.2 Magnetization

Figures 3.11a, 3.11b, and 3.11c show the temperature dependence of the zero-field-cooled (ZFC) and field-cooled (FC) DC magnetization in a magnetic field of 100 Oe, 500 Oe, and 1,000 Oe, respectively, for the 300 ºC sample. The ZFC/FC protocol used here involves cooling the sample in zero field, applying the indicated field, and measuring the magnetization as the sample is heated (ZFC curve). The magnetization is then measured again as the sample is cooled in the same field (FC curve). The magnetization behavior is characterized by: (1) a peak in the ZFC curve and (2) hysteresis, in the form of a bifurcation of the ZFC and FC curves as the temperature is decreased. The strong (decreasing) field dependence of the ZFC peak temperature, T_B, indicates superparamagnetic (and not spin-glass) behavior, where T_B is defined as the blocking temperature[22-25]. Due to the relatively large size of the nanoparticles, T_B is near room temperature for magnetic fields $H < 100$ Oe. The ZFC peak is quite broad which is likely due to a particle size distribution as well as strong interactions between the particles[26]. **Figure 3.12a** shows a series of

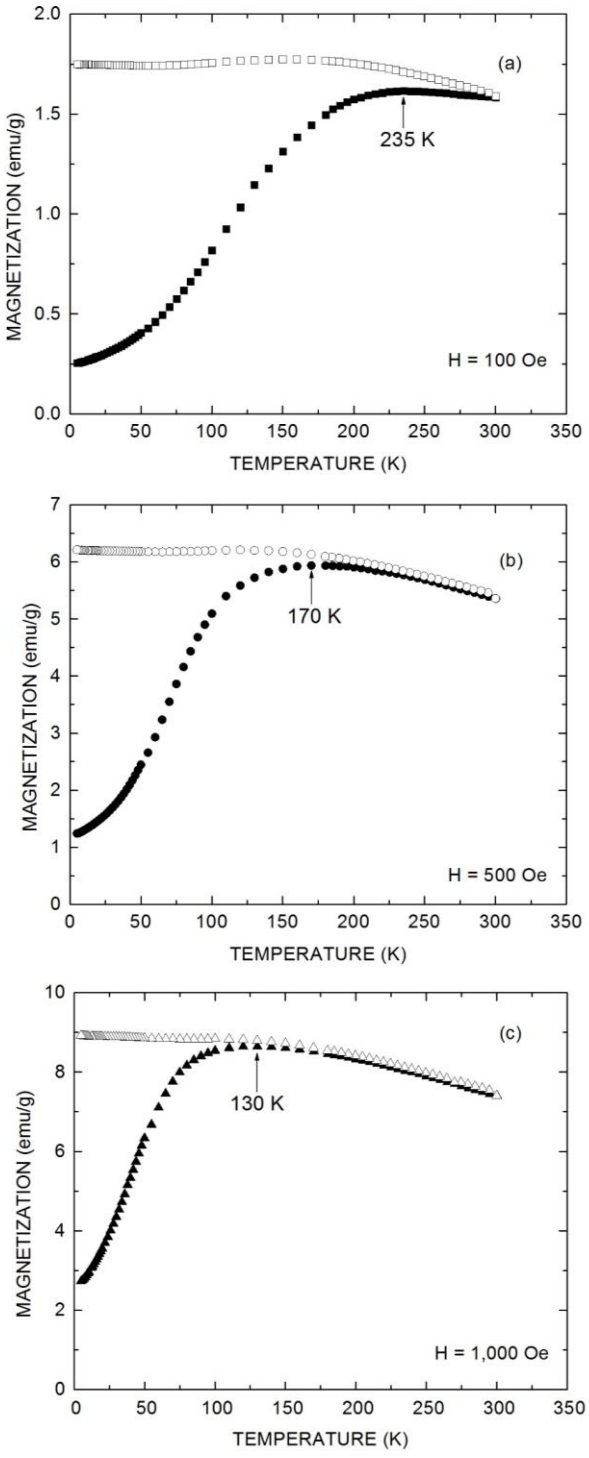

Figure 3.11. Zero-field-cooled (closed symbols) and field-cooled (open symbols) magnetization versus temperature for the sample calcined at 300 ºC for 3 hrs: (a) H = 100 Oe (squares), (b) H = 500 Oe (circles), and (c) H = 1,000 Oe (triangles). The decrease of the peak temperature with magnetic field indicates superparamagnetic behavior; the blocking temperatures T_B are indicated.

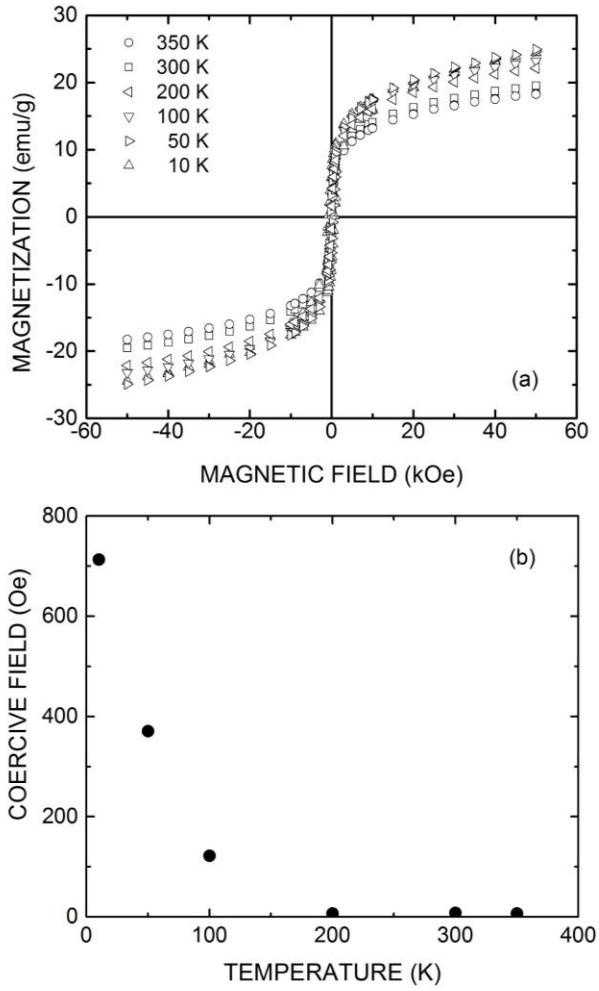

Figure 3.12. (a) Magnetization versus magnetic field (hysteresis loops) measured at temperatures ranging from 10 K to 350 K for the sample calcined at 300 ºC for 3 hrs, (b) temperature dependence of the coercive field values, H_c, obtained from the hysteresis loops.

hysteresis loops measured at temperatures ranging from 10 K to 350 K for the 300 ºC sample. As discussed below, the reduced values for the magnetization are attributed to small particle effects. **Figure 3.12b** shows the temperature dependence of the coercive field values, H_c, obtained from the hysteresis loops. **Figure 3.13** shows ZFC/FC curves (H = 500 Oe and 1,000 Oe) obtained for the 5% H_2 and 20% H_2 samples, while **Figure 3.14** shows hysteresis loops (T = 10 K to 300 K) for the 20% H_2 sample. **Figure 3.14b** shows the temperature dependence of the coercive field values, H_c, obtained from the hysteresis loops. Even for the 5% H_2 sample, which has the smallest

nanoparticles, relatively large fields H = 500 Oe and 1,000 Oe were necessary in order to have T_B appear below the upper temperature limit of the magnetometer.

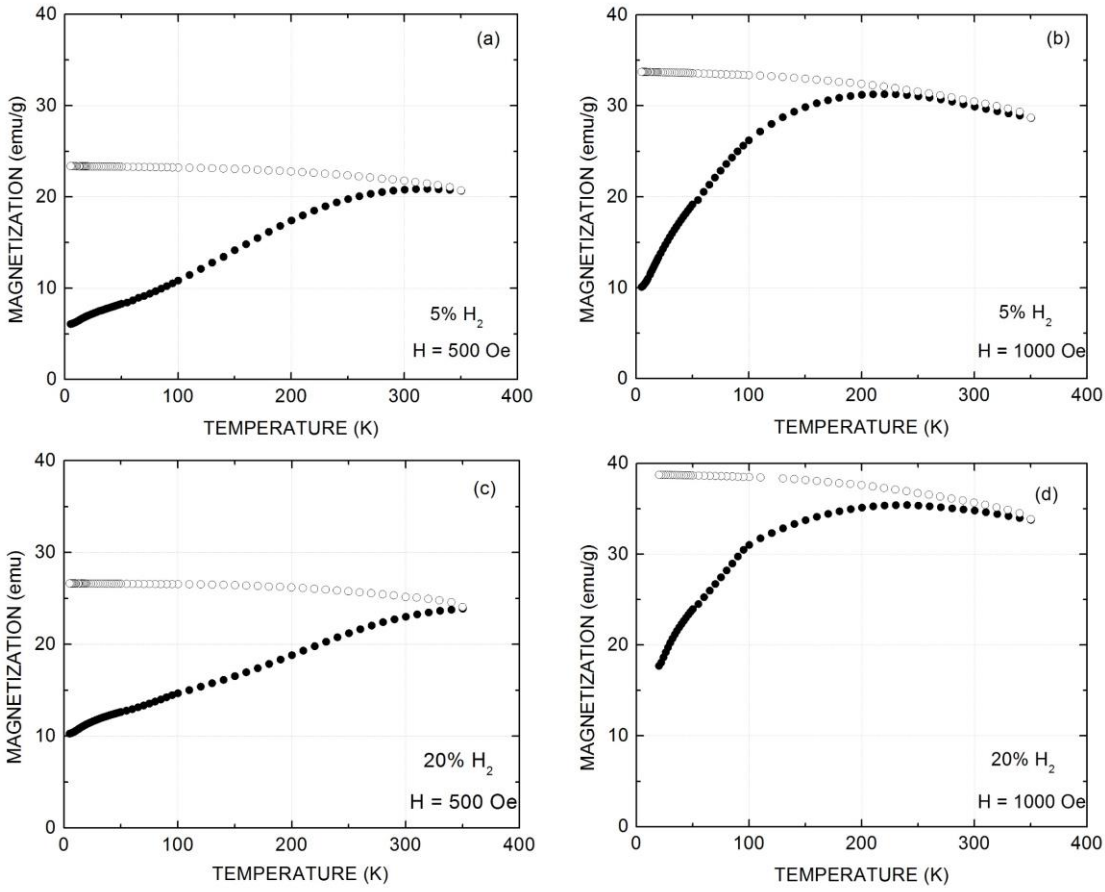

Figure 3.13. Zero-field-cooled (closed symbols) and field-cooled (open symbols) magnetization versus temperature for the sample heated in a 5% H_2 atmosphere at 250 ºC for 3 hrs (a) H = 500 Oe and (b) H = 1,000 Oe. Zero-field-cooled (closed symbols) and field-cooled (open symbols) magnetization versus temperature for the sample heated in a 20% H_2 atmosphere at 250 ºC for 3 hrs (c) H = 500 Oe and (d) H = 1,000 Oe. The decrease of the peak temperature with magnetic field indicates superparamagnetic behavior; the blocking temperatures T_B are indicated.

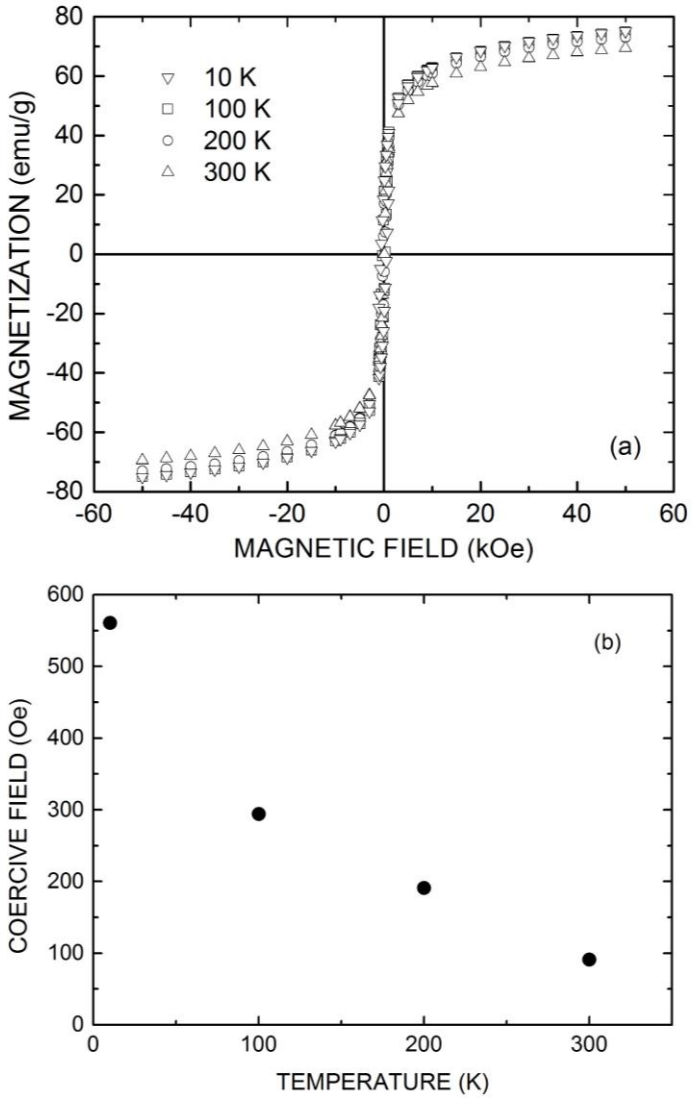

Figure 3.14. (a) Magnetization versus magnetic field (hysteresis loops) measured at temperatures ranging from 10 K to 300 K for the sample heated in a 5% H_2 atmosphere at 250 ºC for 3 hrs and (b) temperature dependence of the coercive field values, H_c, obtained from the hysteresis loops.

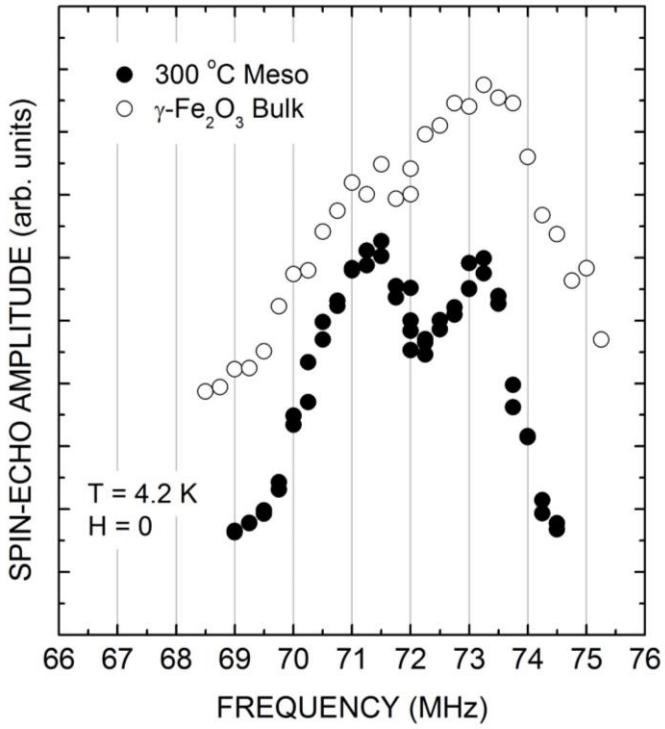

Figure 3.15. ^{57}Fe spin-echo NMR spectra obtained at T = 4.2 K and H = 0: closed circles - mesoporous sample calcined at 300 ºC for 3 hrs and open-circles - commercial "bulk γ-Fe_2O_3 powder sample. The peaks at 71.5 MHz and 73.2 MHz correspond to Fe in the tetrahedral (A) sites and octahedral (B) sites, respectively. The 300 ºC sample shows only the γ-Fe_2O_3 phase.

3.3.3 Nuclear Magnetic Resonance

Figure 3.15 shows the ^{57}Fe spin-echo NMR spectrum obtained at T = 4.2 K and H = 0 for the mesoporous sample calcined at 300 ºC for 3 hrs (closed circles). Distinct peaks are observed at 71.5 MHz and 73.2 MHz which are assigned to Fe in the tetrahedral (A) and octahedral (B) sites, respectively. For reference, the spectrum obtained from a commercial grade "bulk" standard is included (Sigma-Aldrich "γ-Fe_2O_3, < 5 um, > 99%, lot #310050"). The peak positions match; however, the peaks for the mesoporous 300 ºC sample are narrower and more distinct than for the standard. Based on the echo characteristics for the two samples, this is attributed to the fact that

the mesoporous sample has smaller particles with single-domain behavior, whereas the standard sample with larger particles are multidomain (see below). The existence of domain walls in multidomain particles leads to a more pronounced NMR signal enhancement factor than is the case for single domain particles. (The NMR enhancement factors arise in magnetically-ordered materials[27].) Another difference is the existence of a demagnetizing field for single domain particles compared to none for multidomain particles and, therefore, a difference in NMR peak frequencies. However, the relatively small gyromagnetic ratio for ^{57}Fe (γ = 0.13815 MHz/kOe)

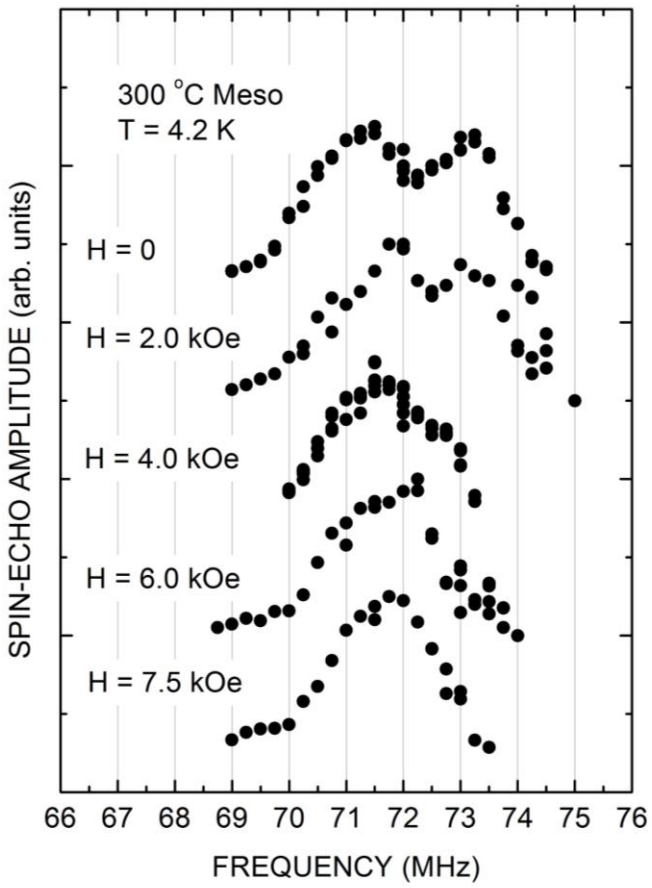

Figure 3.16. ^{57}Fe spin-echo NMR spectra for the sample calcined at 300 °C for 3 hrs obtained at T = 4.2 K with various applied magnetic fields $0 \leq H \leq 7.5$ kOe. Consistent with the ferrimagnetic structure, the tetrahedral (A) site and octahedral (B) site peaks move together for $H \leq 7.5$ kOe (see text).

makes the difference between domain and domain-wall peak frequencies too small to be resolved[28]. Finally, the peak frequencies observed for both samples in **Figure 3.15** are in very good agreement with literature values (71.8 MHz and 73.0 MHz) for "bulk" or multidomain particles of γ-Fe_2O_3[29]. **Figure 3.16** shows a series of ^{57}Fe spin-echo NMR spectra for the sample calcined at 300 ºC for 3 hrs which were obtained at T = 4.2 K and for various magnetic fields $0 \leq H \leq 7.5$ kOe. The tetrahedral (A) site and octahedral (B) site peaks shift upward and downward in frequency, respectively, as the field is increased. This is consistent with the ferrimagnetic structure. In an applied magnetic field, the larger octahedral site moments (smaller tetrahedral site moments) are aligned parallel(antiparallel) to the field. Since the sign of the (contact) hyperfine interaction between the electronic and nuclear moments is negative, the octahedral (tetrahedral) peak shifts

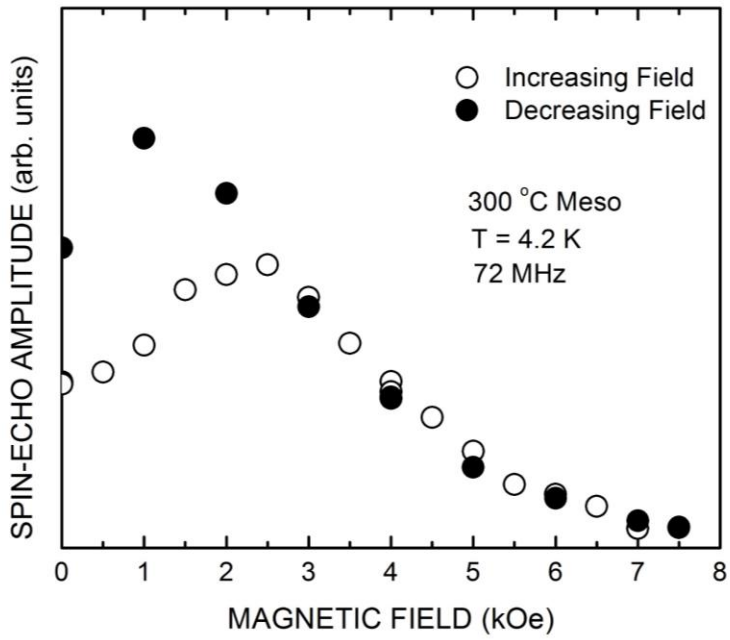

Figure 3.17. ^{57}Fe spin-echo NMR signal amplitude (arb. units) versus applied magnetic field (kOe) obtained at T = 4.2 K and ν = 72.0 MHz for the sample calcined at 300 ºC for 3 hrs: open circles - increasing field and closed circles- decreasing field. The behavior is a consequence of both the anisotropy field and domain enhancement factor.

downward (upward). This behavior confirms the NMR peak assignments. As discussed below, Lee et al.[29] and Daou et al.[30] have used the shift of the NMR peaks with applied magnetic field to calculate a spin canting angle for γ-Fe_2O_3. **Figure 3.17** shows the behavior of the ^{57}Fe spin-echo NMR signal amplitude as a function of the applied magnetic field. The initial increase of the NMR signal amplitude arises as the external field overcomes the anisotropy field (estimated $H_{anis} \approx 2{,}500$

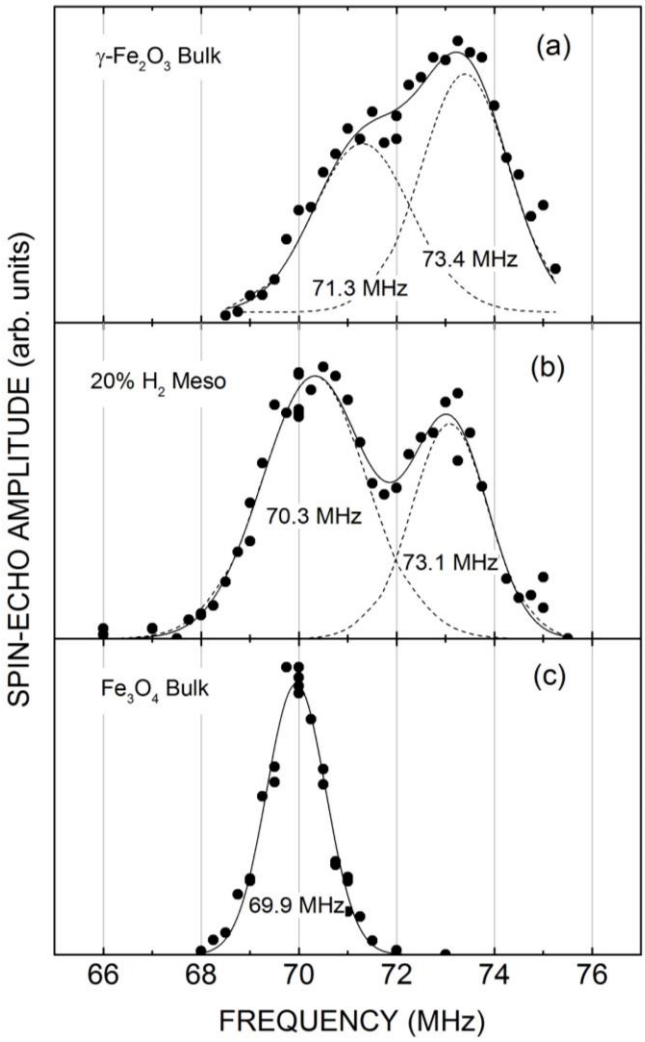

Figure 3.18. ^{57}Fe spin-echo NMR spectra obtained at T = 4.2 K and H = 0: (a) commercial "bulk" γ-Fe_2O_3 powder sample, (b) mesoporous sample heated at 250 ºC for 3 hrs in an 20% H_2 – 80% Ar atmosphere, and (c) commercial "bulk" Fe_3O_4 powder sample. The 20% H_2 sample shows both the γ-Fe_2O_3 and Fe_3O_4 phases.

Oe) and the magnetic moments align parallel (or antiparallel) with the external field (perpendicular to the RF coil). The gradual decease of the signal amplitude is due to the decrease in the domain enhancement factor with the magnetic field[31].

Figure 3.18 shows the ^{57}Fe spin-echo NMR spectrum obtained at T = 4.2 K and H = 0 for the sample heated at 250 ºC for 3 hrs in an atmosphere of 20% H_2 - 80% Ar (see **Figure 3.18b**). For reference see the ^{57}Fe spin-echo NMR spectra for commercial "bulk" γ-Fe_2O_3 (see **Figure 3.18a**, same standard described above) and commercial "bulk" Fe_3O_4 (see **Figure 3.18c**, Sigma-Aldrich "Fe_3O_4, 99.99%, lot #518158"). The relatively sharp peak at 69.9 MHz for bulk Fe_3O_4 (**Figure 3.18c**) is attributed to Fe in the tetrahedral (A) sites. This is in good agreement with many previous reports[32]. The sharp peak for tetrahedral (A) site Fe is in contrast to the more distributed, and usually hard to observe, line shape for octahedral (B) site Fe which occurs over the frequency range $\nu \approx 65.7$ MHz to 67.3 MHz. The spectrum for the 20% H_2 mesoporous sample (**Figure 3.18b**) has a distinct peak at 73.1 MHz, which is characteristic of γ-Fe_2O_3 and not Fe_3O_4.

Furthermore, the peak at 70.3 MHz in the spectrum for the 20% H_2 mesoporous sample is broad due to the fact that it is a combination of the tetrahedral (A) site peaks for both γ-Fe_2O_3 and Fe_3O_4. This shows that the 20% H_2 meso sample has both phases present, which is hard to determine from PXRD, particularly when dealing with nanoparticles. The ^{57}Fe NMR spectrum obtained from a second commercial lab grade magnetite bulk standard (Sigma-Aldrich "Fe_3O_4, < 5 μm, 95%, lot #310069") also showed a combination of the γ-Fe_2O_3 and Fe_3O_4 phases. In their work on monodisperse iron oxide nanoparticles, S. G. Lee et al.[33] have suggested using ^{57}Fe NMR as a tool for distinguishing between the two spinel phases. Finally, the spin-spin relaxation time T_2 was typically much longer than the pulse separation $\tau = 20$ μs used to obtain the NMR spectra

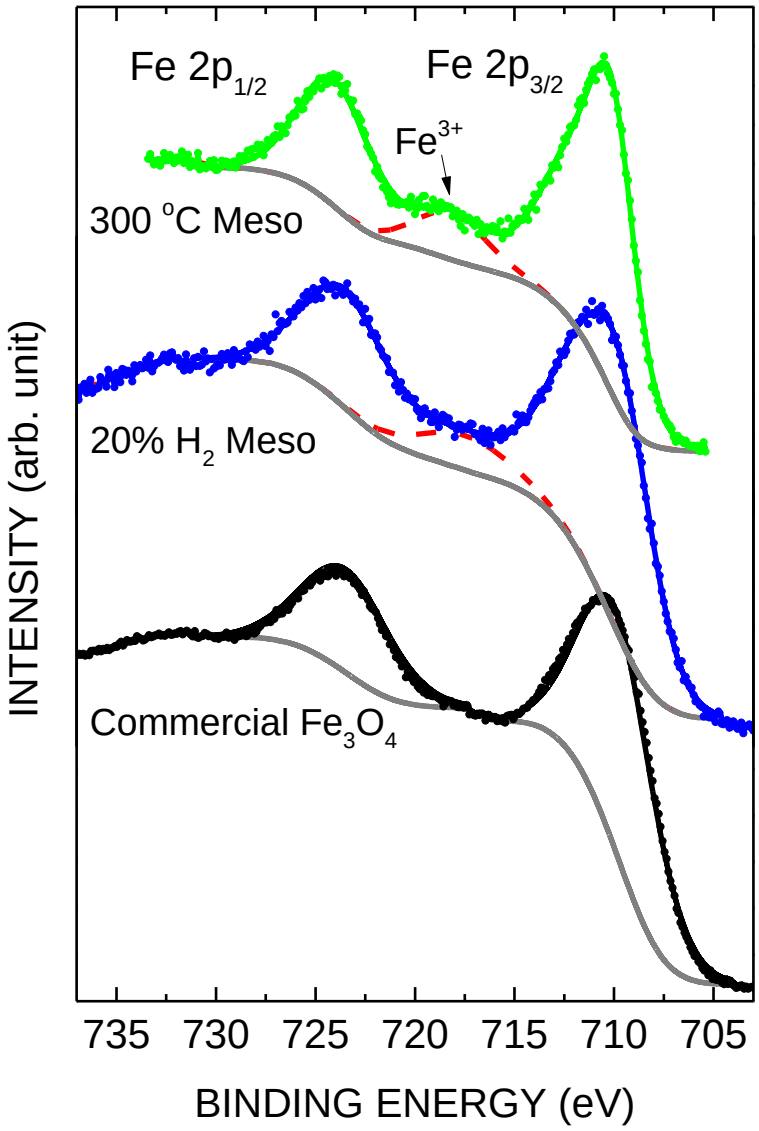

Figure 3.19. X-ray Photoemission Spectrum (XPS) for the 300 ºC mesoporous sample (green dots are the data points and the green solid line is the fitting curve), 20% H_2 mesoporous sample (blue dots are the data points and the blue solid line is the fitting curve) and the commercial Fe_3O_4 (black dots are the data points and the black solid line is the fitting curve). The Shirley backgrounds for each sample are presenting as the solid gray lines. The Fe^{3+} satellite peak (red dash line) is clearly observed for the 300 ºC mesoporous sample, consistent with the γ-Fe_2O_3 phase. The satellite structure of the commercial Fe_3O_4 is completely obscured by the overlapping Fe^{2+} and Fe^{3+} satellites. The Fe^{3+} satellite is only partially obscured by the Fe^{2+} satellite for the 20% H_2 mesoporous sample, which indicates a contribution from the γ-Fe_2O_3 phase.

in this report. (e.g., $T_2 \approx 400$ μs at ν = 72.0 MHz for the 300 ºC sample.) Therefore, no T_2 correction to the measured spectra was required[34].

As shown in **Figure 3.19**, Fe 2p core level X-ray photoemission spectra (XPS) were obtained for the 300 ºC mesoporous sample and the 20% H_2 mesoporous sample. For reference, the XPS spectrum for the commercial standard Fe_3O_4 sample (lot #518158) is also shown. The various iron oxides (such as γ-Fe_2O_3, Fe_3O_4, and FeO) can be distinguished from each other by their characteristic satellite peaks[35]. The Fe $2p_{3/2}$ satellite binding energies are 715.5 eV and 718.8 eV for the Fe^{2+} and Fe^{3+} valence states, respectively. For the Fe_3O_4 commercial standard, the Fe $2p_{3/2}$ (710.6 eV) and the Fe $2p_{1/2}$ (724.1 eV) double peaks match up with literature values[35]. However, the Fe^{2+} and Fe^{3+} satellites overlap and, therefore, the satellite structure is completely obscured. **Figure 3.19** shows that for the 300 ºC sample there is a clear Fe^{3+} satellite consistent with the γ-Fe_2O_3 phase. However, for the 20% H_2 sample, a less obvious Fe^{3+} satellite becomes apparent after a careful curve fitting. This is consistent with the NMR results in that there is a contribution from the γ-Fe_2O_3 phase.

3.4 Discussion and Conclusions

This work presents a combined magnetization and NMR study of mesoporous iron oxide nanostructured materials. The materials were prepared by a recently developed one-step soft-templating procedure, which consists of an inverse micelle packing approach[15]. The iron oxide phases studied were maghemite (γ-Fe_2O_3) and magnetite (Fe_3O_4). In this study, a first series of three samples (nominally γ-Fe_2O_3) was synthesized using the soft-templating procedure with three different calcination temperatures (250 ºC, 300 ºC, and 350 ºC) for 3 hrs in an air atmosphere. A

second series of three samples (nominally Fe_3O_4) was synthesized using the soft-templating procedure with a temperature of 250 ºC for 3 hrs in three different atmospheres (5% H_2 − 95% Ar, 10% H_2 − 90% Ar, and 20% H_2 − 80% Ar). All the samples were characterized by a combination of LAXD, PXRD, SAXS, N_2 sorption, SEM, and TEM; the results from the characterization are summarized in **Table 3.1**.

A general review of the parameters listed in **Table 3.1** shows that, in contrast to traditional mesoporous materials, the materials which are prepared using the new soft-template procedure (designated UCT materials[15]) exhibit an expansion of the structure with heat treatment. The first series sample with calcination at 350 ºC for 3 hours appears to go against this trend; however, the mesoporous structure might be breaking down. Although the N_2 sorption isotherms for the first series samples are Type IV, the hysteresis character becomes more Type H3 with heat treatment, indicating slit-like pores. However, the N_2 sorption isotherms for the second series (H_2 treated) samples are all Type IV with Type H1 hysteresis. This is consistent with a more uniform cylindrical pore network. From the SEM, TEM, and small-angle X-ray results, the general sample morphology can be described as spherical clusters consisting of random closed-packed aggregations of similar size iron oxide nanoparticles and not an iron oxide framework. This picture is consistent with earlier work[15-16]. The 250 ºC, 300 ºC, and 20% H_2 samples are characterized by favorable BET surface areas all in excess of 100 m^2/g.

In the spinel structure, the O atoms form an fcc lattice and the Fe atoms are located in the interstitial sites of the O lattice. There are two types of interstitial sites with: (1) Fe in the center of a tetrahedron (A) formed by surrounding O atoms and (2) Fe in the center of an octahedron (B) formed by surrounding O atoms. Magnetite (Fe_3O_4) has the inverse spinel structure with all the tetrahedral (A) sites occupied by Fe^{3+} ions and an equal number of Fe^{2+} and Fe^{3+} ions occupying

the octahedral (B) sites. Bulk Fe_3O_4 is ferrimagnetic with an ordering temperature 850 K. The Fe^{3+} moments on the two sublattices are antiparallel and cancel leaving just the Fe^{2+} moments unpaired and a net magnetic moment of 4.0 μ_B per formula unit. Maghemite (γ-Fe_2O_3) has the normal spinel structure with all the tetrahedral (A) sites occupied by Fe^{3+} ions and both Fe^{3+} ions and vacancies occupying the octahedral (B) sites. Bulk γ-Fe_2O_3 is also ferrimagnetic with an ordering temperature 850 K. The minority Fe^{3+} moments on the tetrahedral (A) sites are antiparallel to the majority Fe^{3+} moments on the octahedral (B) sites resulting in a magnetic moment of 3.33 μ_B per formula unit.

Detailed magnetization and NMR measurements were carried out on selected samples from the six characterized in **Table 3.1**. Ferromagnetic and ferrimagnetic particles with diameters in the nanometer range can exhibit superparamagnetic behavior at or below room temperature. Such is the case for the first series samples which were calcined at different temperatures. For the first series samples, the nanoparticles which form the mesoporous structure are γ-Fe_2O_3. The magnetic field dependence of the peak in the ZFC curves (which defines the blocking temperature T_B) shown in **Figure 3.11** for the 300 ^oC sample, confirms that the behavior is superparamagnetic and not spin-glass. The corresponding magnetization curves (hysteresis loops) obtained at various temperatures are shown in **Figure 3.12** for the 300 ^oC sample. The absence of a remanent magnetization and coercive field at or near room temperature also indicates superparamagnetic behavior and facilitates magnetic separation and recycling in any practical application[36]. There is no real saturation of the magnetization for fields up to 50 kOe even at 10 K. The highest magnetization value is approximately one third that for bulk γ-Fe_2O_3 (80 emu/g)[28]. This reduction of the saturation magnetization has been attributed a variety of mechanisms: (1) spin canting, both surface and volume[30, 37], (2) octahedral moments that are aligned antiparallel to the magnetic field[30],

and (3) non-magnetic surface layers[38]. To date, there is no clear agreement on this point. For the second series samples which were heated in different H_2−Ar atmospheres, the nanoparticles which form the mesoporous structure are mixed phase γ-Fe_2O_3 + Fe_3O_4. As can be seen from the data in **Table 3.1**, the particle sizes are larger than those for the first series samples. Consequently, the blocking temperature values obtained from the ZFC curves are higher and hysteresis behavior in the magnetization curves still exists at room temperature (**Figures 3.14 and 3.19**).

Since the first observation of NMR in a magnetically ordered material by Gossard and Portis[39], there have been numerous reports concerning ^{57}Fe NMR in various bulk Fe-based metal oxides[40]. For a recent review, see M. Fardis, et al.[28]. To our knowledge, there have been only two previous reports of ^{57}Fe NMR measurements on small diameter (≤ 10 nm) single-domain γ-Fe_2O_3 nanoparticles. S. G. Lee et al.[33] studied two samples of monodisperse iron oxide nanoparticles (7 nm and 9.6 nm) and suggest that ^{57}Fe is a useful tool for distinguishing between iron oxide phases. M. Fardis, et al.[28] have studied the interparticle interactions for well-crystallized 10 nm γ-Fe_2O_3 nanoparticles, both coated and uncoated. There are two ^{57}Fe NMR reports for larger γ-Fe_2O_3 nanoparticles: (1) S.-J. Lee, et al.[29] and T. J. Daou, et al.[30] carried out a combined study of ^{57}Fe NMR and in-field Mössbauer spectroscopy, which examined the spin canting of surface spins in 39 nm γ-Fe_2O_3 nanoparticles and (2) T. J. Bastow et al.[41-42] reported detailed ^{57}Fe NMR line shapes for γ-Fe_2O_3 powders, 18 nm to 85 nm, prepared by attrition milling. We have found no NMR reports in the literature for small Fe_3O_4 nanoparticles or iron oxide mesoporous nanostructured materials.

Probably the most significant result from the NMR measurements in this work is the identification of the crystallographically similar γ-Fe_2O_3 and Fe_3O_4 spinel phases in the mesoporous nanostructured materials. It is difficult to distinguish between these two phases with

XRD, particularly in the case of nanoparticles where the peaks are broadened. As shown in **Figure 3.15**, the ^{57}Fe spin-echo NMR spectrum for the 300 ^{o}C mesoporous sample is characterized by peaks at 71.5 MHz and 73.2 MHz which match the peaks for the standard bulk γ-Fe_2O_3 sample as well as previously reported values for bulk γ-Fe_2O_3[29]. The γ-Fe_2O_3 phase, and only the γ-Fe_2O_3 phase, is identified in the 300 ^{o}C mesoporous sample. The magnetic field dependences for the two peaks (see **Figure 3.16**) are consistent with the peak assignments in the spinel ferrimagnetic structure, i.e., 71.5 MHz and 73.2 MHz for Fe in the tetrahedral (A) and octahedral (B) sites, respectively. However, unlike the case for the 300 ^{o}C first series sample, both the γ-Fe_2O_3 and Fe_3O_4 phases are identified in the 20% H_2 second series sample (see **Figure 3.18**). The peak at 73.1 MHz is attributed to Fe in the octahedral (B) sites of γ-Fe_2O_3 while the (broadened) peak at 70.3 MHz is a combination of the tetrahedral (A) sites for both γ-Fe_2O_3 and Fe_3O_4. Subsequent XPS spectra supported the NMR results for both the 300 ^{o}C and 20% H_2 samples.

3.5 Reference

1. Tüysüz, H.; Salabaş, E. L.; Bill, E.; Bongard, H.; Spliethoff, B.; Lehmann, C. W.; Schüth, F., Synthesis of hard magnetic ordered mesoporous $Co_3O_4/CoFe_2O_4$ nanocomposites. *Chem. Mater.* **2012,** *24* (13), 2493-2500 and references therein.

2. Wang, G.; Liu, H.; Horvat, J.; Wang, B.; Qiao, S.; Park, J.; Ahn, H., Highly ordered mesoporous cobalt oxide nanostructures: synthesis, characterisation, magnetic properties, and applications for electrochemical energy devices. *Chem. Eur. J.* **2010,** *16* (36), 11020-11027 and references therein.

3. Chen, C. H.; Abbas, S. F.; Morey, A.; Sithambaram, S.; Xu, L. P.; Garces, H. F.; Hines, W. A.; Suib, S. L., Controlled synthesis of self-assembled metal oxide hollow spheres via tuning redox potentials: versatile nanostructured cobalt oxides. *Adv. Mater.* **2008,** *20* (6), 1205-1209 and references therein.

4. Tian, B.; Liu, X.; Solovyov, L. A.; Liu, Z.; Yang, H.; Zhang, Z.; Xie, S.; Zhang, F.; Tu, B.; Yu, C., Facile synthesis and characterization of novel mesoporous and mesorelief oxides with gyroidal structures. *J. Am. Chem. Soc.* **2004,** *126* (3), 865-875 and references therein.

5. Tian, Z.-R.; Tong, W.; Wang, J.-Y.; Duan, N.-G.; Krishnan, V. V.; Suib, S. L., Manganese oxide mesoporous structures: mixed-valent semiconducting catalysts. *Science* **1997,** *276* (5314), 926-930.

6. Jiao, F.; Jumas, J.-C.; Womes, M.; Chadwick, A. V.; Harrison, A.; Bruce, P. G., Synthesis of ordered mesoporous Fe_3O_4 and γ-Fe_2O_3 with crystalline walls using post-template reduction/oxidation. *J. Am. Chem. Soc.* **2006,** *128* (39), 12905-12909 and references therein.

7. Yu, B. Y.; Kwak, S.-Y., Assembly of magnetite nanocrystals into spherical mesoporous aggregates with a 3-D wormhole-like pore structure. *J. Mater. Chem.* **2010,** *20* (38), 8320-8328.

8. Long, J. W.; Logan, M. S.; Rhodes, C. P.; Carpenter, E. E.; Stroud, R. M.; Rolison, D. R., Nanocrystalline iron oxide aerogels as mesoporous magnetic architectures. *J. Am. Chem. Soc.* **2004,** *126* (51), 16879-16889.

9. Tan, Y.; Zhuang, Z.; Peng, Q.; Li, Y., Room-temperature soft magnetic iron oxide nanocrystals: synthesis, characterization, and size-dependent magnetic properties. *Chem. Mater.* **2008,** *20* (15), 5029-5034.

10. Lu, A.-H.; Salabas, E. L.; Schüth, F., Magnetic nanoparticles: synthesis, protection, functionalization, and application. *Angew. Chem. Int. Ed.* **2007,** *46* (8), 1222-1244.

11. Tronc, E., Magnetic relaxation in fine-particle systems. *Advances in* **1997**, 283.

12. Majetich, S.; Sachan, M., Magnetostatic interactions in magnetic nanoparticle assemblies: energy, time and length scales. *J. Phys. D: Appl. Phys.* **2006,** *39* (21), R407.

13. Ryoo, R.; Joo, S. H.; Jun, S., Synthesis of highly ordered carbon molecular sieves via template-mediated structural transformation. *J. Phys. Chem. B* **1999,** *103* (37), 7743-7746.

14. Schüth, F., Non-siliceous mesostructured and mesoporous materials. *Chem. Mater.* **2001,** *13* (10), 3184-3195.

15. Poyraz, A. S.; Kuo, C.-H.; Biswas, S.; King'ondu, C. K.; Suib, S. L., A general approach to crystalline and monomodal pore size mesoporous materials. *Nat. Commun.* **2013,** *4*, 2952.

16. Poyraz, A. S.; Hines, W. A.; Kuo, C.-H.; Li, N.; Perry, D. M.; Suib, S. L., Mesoporous Co_3O_4 nanostructured material synthesized by one-step soft-templating: A magnetic study. *J. Appl. Phys.* **2014,** *115* (11), 114309.

17. Boissière, C.; Larbot, A.; van der Lee, A.; Kooyman, P. J.; Prouzet, E., A new synthesis of mesoporous MSU-X silica controlled by a two-step pathway. *Chem. Mater.* **2000,** *12* (10), 2902-2913.

18. Porod, G., Die Röntgenkleinwinkelstreuung von dichtgepackten kolloiden Systemen. *Colloid. Polym. Sci.* **1951,** *124* (2), 83-114.

19. Korgel, B. A.; Fitzmaurice, D., Small-angle X-ray-scattering study of silver-nanocrystal disorder-order phase transitions. *Phys. Rev. B* **1999,** *59* (22), 14191.

20. Sing, K.; Everett, D.; Haul, R.; Moscou, L.; Pierotti, R.; Rouquerol, J.; Siemieniewska, T., Reporting physisorption data for gas/solid systems with special reference to the determination of surface area and porosity. *Pure Appl. Chem.* **1985,** *57*, 603-619.

21. Barrett, E. P.; Joyner, L. G.; Halenda, P. P., The determination of pore volume and area distributions in porous substances. I. Computations from nitrogen isotherms. *J. Am. Chem. Soc.* **1951,** *73* (1), 373-380.

22. Zhang, Y.; Budnick, J.; Hines, W.; Chien, C.; Xiao, J., Effect of magnetic field on the superparamagnetic relaxation in granular Co-Ag samples. *Appl. Phys. Lett.* **1998,** *72* (16), 2053-2055.

23. Dutta, P.; Manivannan, A.; Seehra, M.; Shah, N.; Huffman, G., Magnetic properties of nearly defect-free maghemite nanocrystals. *Phys. Rev. B* **2004,** *70* (17), 174428.

24. Dormann, J.; Fiorani, D.; El Yamani, M., Field dependence of the blocking temperature in the superparamagnetic model: H^{23} coincidence. *Phys. Lett. A* **1987,** *120* (2), 95-99.

25. El-Hilo, M.; O'grady, K.; Chantrell, R., Susceptibility phenomena in a fine particle system: II. Field dependence of the peak. *J. Magn. Magn. Mater.* **1992,** *114* (3), 307-313.

26. García-Otero, J.; Porto, M.; Rivas, J.; Bunde, A., Influence of dipolar interaction on magnetic properties of ultrafine ferromagnetic particles. *Phys. Rev. Lett.* **2000,** *84* (1), 167.

27. Turov, E.; Petrov, M., Nucelar Magnetic Resonance in Ferro and Antiferromagnets Halsted. *New York* **1972**.

28. Fardis, M.; Douvalis, A.; Tsitrouli, D.; Rabias, I.; Stamopoulos, D.; Kehagias, T.; Karakosta, E.; Diamantopoulos, G.; Bakas, T.; Papavassiliou, G., Structural, static and dynamic magnetic properties of dextran coated γ-Fe_2O_3 nanoparticles studied by ^{57}Fe NMR, Mössbauer, TEM and magnetization measurements. *J. Phys. Condens. Matter*. **2012,** *24* (15), 156001.

29. Lee, S.-J.; Lee, S., The spin structure of maghemite investigated by ^{57}Fe NMR. *New J. Phys.* **2006,** *8* (6), 98.

30. Daou, T. J.; Greneche, J.-M.; Lee, S.-J.; Lee, S.; Lefevre, C.; Bégin-Colin, S.; Pourroy, G., Spin canting of maghemite studied by NMR and In-Field Mossbauer spectrometry. *J. Phys. Chem. C* **2010,** *114* (19), 8794-8799.

31. Dho, J.; Kim, M.; Lee, S.; Lee, W.-J., The enhancement effect in the domain and domain wall in ^{57}Fe nuclear magnetic resonance. *J. Appl. Phys.* **1997,** *81* (3), 1362-1367.

32. Boyd, E. L., Temperature Dependence of Nuclear Magnetic Resonance of ^{57}Fe in Magnetite. *Phys. Rev.* **1963,** *129* (5), 1961.

33. Lee, S.; Kang, H.; Kwak, M.; Lee, Y.-J.; Lee, G.; Yu, I.; Kim, H. J., Identification of spinel iron oxide nanoparticles by ^{57}Fe NMR. *J. Anal. Sci. Tech* **2011,** *2*, A84-A87.

34. Hines, W.; Budnick, J.; Perry, D.; Majetich, S.; Booth, R.; Sachan, M., Nuclear magnetic resonance and magnetization study of surfactant-coated epsilon-Co nanoparticles. *Phys. Status Solidi B* **2011,** *248* (3), 741-747.

35. Yamashita, T.; Hayes, P., Analysis of XPS spectra of Fe^{2+} and Fe^{3+} ions in oxide materials. *Appl. Surf. Sci.* **2008,** *254* (8), 2441-2449.

36. Ge, J.; Zhang, Q.; Zhang, T.; Yin, Y., Core–satellite nanocomposite catalysts protected by a porous silica shell: controllable reactivity, high stability, and magnetic recyclability. *Angew. Chem. Int. Ed.* **2008,** *120* (46), 9056-9060.

37. Coey, J. M. D., Noncollinear spin arrangement in ultrafine ferrimagnetic crystallites. *Phys. Rev. Lett.* **1971,** *27* (17), 1140.

38. Berkowitz, A.; Schuele, W.; Flanders, P., Influence of Crystallite Size on the Magnetic Properties of Acicular γ-Fe_2O_3 Particles. *J. Appl. Phys.* **1968,** *39* (2), 1261-1263.

39. Gossard, A.; Portis, A., Observation of nuclear resonance in a ferromagnet. *Phys. Rev. Lett.* **1959,** *3* (4), 164.

40. Freeman, A. J.; Watson, R. E.; Rado, G.; Suhl, H., Magnetism. *Academic Press*, New York: 1965.

41. Bastow, T. J.; Trinchi, A.; Hill, M.; Harris, R.; Muster, T., Vacancy ordering in γ-Fe_2O_3 nanocrystals observed by ^{57}Fe NMR. *J. Magn. Magn. Mater.* **2009,** *321* (17), 2677-2681.

42. Bastow, T. J.; Trinchi, A., NMR analysis of ferromagnets: Fe oxides. *Solid State Nucl. Magn. Reson.* **2009,** *35*, 25-31.

CHAPTER 4. Pressure Effects on the High Sorption Capacity of Mesoporous Cobalt Oxide for Desulfurization at Low Temperature

4.1 Introduction

Hydrogen sulfide (H_2S) is an intensely poisonous, corrosive, flammable, and explosive gas. H_2S is found in natural gas and coal gas. This water soluble gas may be oxidized into sulfur dioxide or sulfuric acid in the atmosphere and is adsorbed into moist soil, plant foliage, or other organic material.[1] A low concentration of H_2S will cause irritation of the eyes, nose, or throat. More than 100 ppm of H_2S will lead to the loss of smell and 2000 ppm will kill people in minutes. The removal of sulfur will benefit not only the natural environment but also industrial processes, where sulfur is formed from corrosion and deactivation.[2] Nowadays, adsorption, condensation, oxidation reactions, catalytic combustion and acid gas treatment are commonly used to remove H_2S.[2-4] Adsorption is one of the most widely used methods, because of its efficiency and reliability. By using different sorbents, adsorption can work efficiently in a wide temperature range. Studies have been done with many common sorbents, such as activated carbon, zeolites, modified alumina, clays, and metal oxides.[3-7] The metal oxides have a high affinity for their sulfides. Therefore, zinc, manganese, copper, iron, cobalt, nickel, chromium, and calcium based oxides have been deeply studied.[6-10] The reaction equation is shown in **Equation (1)**:[1]

$$M_xO_{y\,(s)} + y\,H_2S_{\,(g)} \rightarrow M_xS_{y\,(s)} + y\,H_2O_{\,(g)} \qquad (1)$$

Mesoporous materials, with high surface area and highly ordered nano-structures, aid the solid-gas reaction. The gas molecules would have a larger contact area with the sorbent, making the reaction more efficient. In addition, the molecules might be trapped in the pores, and thus

extend the contact time between the solid and the gas. Therefore, the conversion of the solid will be increased during the reaction. In a previous study[2], the sulfur sorption capacity of mesoporous Co_3O_4 was considerably higher than other materials, which were synthesized by a newly developed one-step, soft-templating method.[11] When compared with the commercial, non-porous samples, the capacity was about 50 times better. In this study, we determined the mechanism of this process by studying the effects of pressure on the same sorbent under the same reaction conditions.

4.2 Synthesis method

4.2.1 Sorbent Preparation

Highly-ordered mesoporous nanostructured cobalt-oxide materials (meso-Co_3O_4) were synthesized using a recently-developed one-step, soft-templating approach.[11] Reagent-grade chemicals were used in the synthesis. Poly(ethylene glycol)-block-poly(propylene glycol)-block-poly(ethylene glycol) PEO_{20}-PPO_{70}-PEO_{20} (Pluronic P123) copolymer surfactant, 1-butanol (anhydrous, 99.8%), and cobalt(II) nitrate hexahydrate ($Co(NO_3)_2 \cdot 6H_2O \geq 98.0\%$) were purchased from Sigma-Aldrich. Concentrated nitric acid (68%-70% HNO_3) was purchased from J. T. Baker. The material was synthesized by dissolving 5.82 g (0.020 mol) of $Co(NO_3)_2 \cdot 6H_2O$ in 17.8 g (0.23 mol) of a 1-butanol solution containing 2.4 g (4.31×10^{-4} mol) of P123 and 2.4 g (0.038 mol) of concentrated HNO_3 at room temperature (RT). A clear gel was obtained after stirring the above-mentioned solution in a 150 mL beaker. The gel was placed in an oven and maintained at 120 ºC for 3.5 h. The resulting powder was washed with ethanol, centrifuged, and dried in a vacuum oven overnight. The dry powder was heated at 150 ºC for 12 h and cooled down to room temperature.

To achieve the desired crystallite mesoporous structure, the product was calcined at 250 ºC for 1 h.

4.2.2 Sulfurization Reactor

The sulfur sorption experiments were carried out at 200 ºC. The laboratory scale sulfur sorption apparatus is shown in **Scheme 1.1**. In each experiment, 50 mg of mesoporous Co_3O_4 was uniformly packed in the reactor supported by quartz wool. The back pressure was built up by the densely-packed sample and read from the manometer. The pressures were controlled by the condensation of the sample packing in each experiment. Prior to each experiment, the samples were heated at 200 ºC with 40 sccm He flowing for 1 h. During the experiments, all the flow rates were set at 50 sccm. The concentration of H_2S was 500 ppm, which was diluted by helium gas. The outlet gases were analyzed for sulfur using an SRI 8610C gas chromatograph (GC) with a GS-GasPro capillary column (30 m × 0.32 mm I.D.) and a flame photometric detector (FPD). A 10-port sampling valve with an electronic actuator was used to make automatic injections into the GC every 10 min with He as the carrier gas. Two mass flow controllers (MFCs) controlled the flow rates, feed and composition. One of the MFCs is a MKS model 1479A with 20 sccm ± 1% full scale. The other is an Alicat Scientific with 200 sccm ± 0.2% full scale. The weight hourly space velocity (WHSV) was fixed at ~ 60 L/h·g.

4.3 Results

4.3.1 Fresh Sorbent Characterization

Figure 4.1a shows the wide-angle powder X-ray diffraction (PXRD) pattern of the fresh mesoporous Co_3O_4 sorbent. The pattern matches up well with the cobalt oxide standard (PDF Card No. 00-042-1467). According to the broadening of the diffraction peaks, the crystalline size of the sorbent sample was calculated by the Scherrer equation which is shown in **Equation (2)**:

$$D = 0.89\,\lambda / (\beta \cos\theta) \qquad (2)$$

where D is the crystalline grain diameter, β is the full width at half maximum (FWHM) of the diffraction peak (see **Figure 4.1a**), and λ is the wavelength of Cu Kα1, which is 0.15406 nm. The

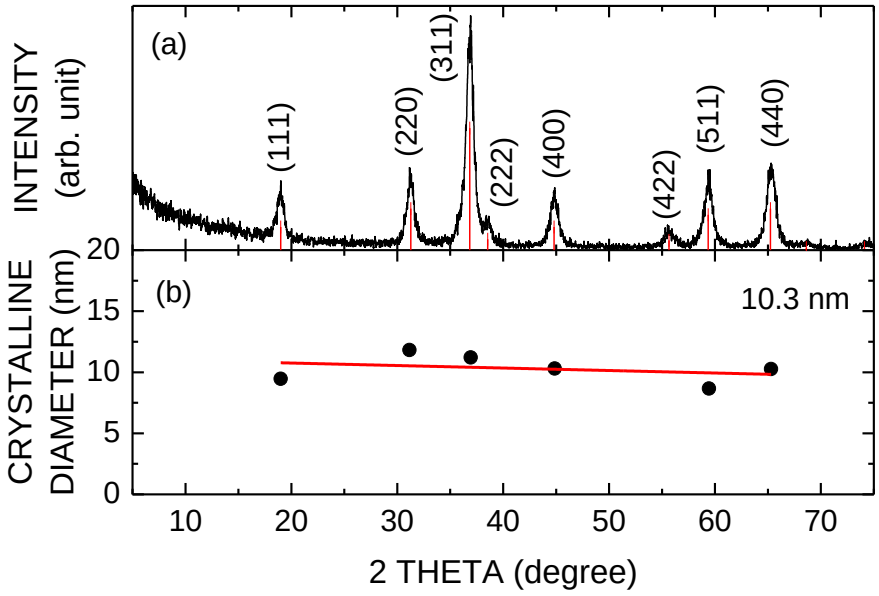

Figure 4.1. (a) Wide angle X-ray diffraction pattern of the fresh mesoporous Co_3O_4. (b) Crystalline size fitting by the Scherrer equation.

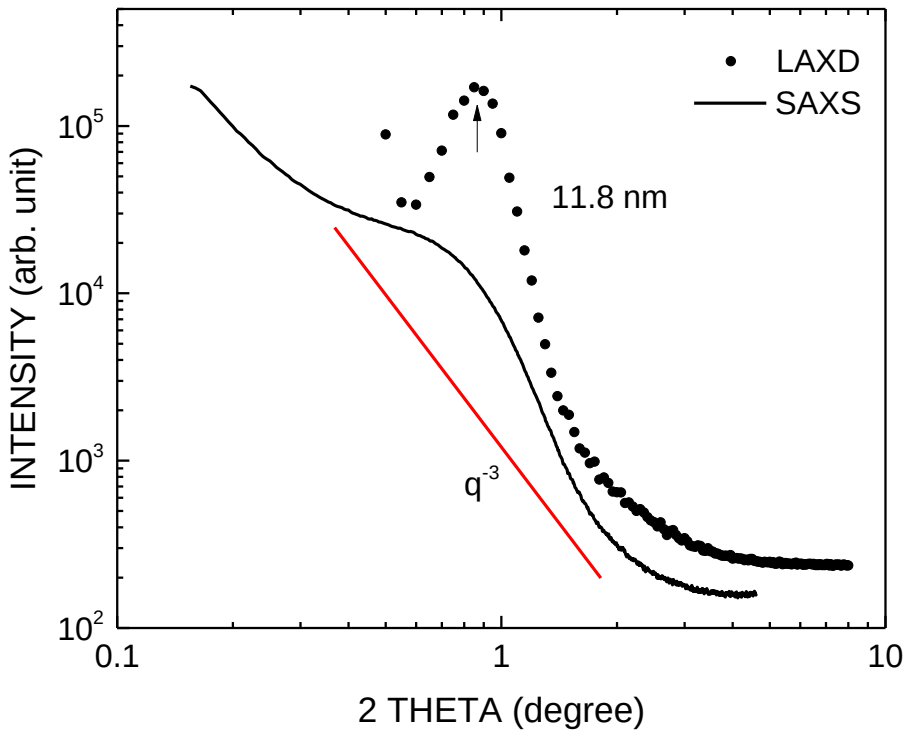

Figure 4.2. Low-angle X-ray diffraction (black solid dots) and small angle X-ray scattering (black line) of the fresh mesoporous Co_3O_4. The red line is the slope fitting of q^{-3}.

calculation results from each peak were averaged by linear fitting, which is shown in **Figure 4.1b**. Therefore, the average crystalline size of the fresh mesoporous Co_3O_4 is approximately 10.3 nm.

The typical ordered mesoporous nanostructure of the fresh mesoporous Co_3O_4 was characterized by low-angle X-ray diffraction (LAXD), small angle X-ray scattering (SAXS) and N_2 sorption. **Figure 4.2** shows the LAXD and SAXS of the fresh mesoporous Co_3O_4. The black dots represent the LAXD measurement and the black solid line represents the SAXS measurement. Because the mesoporous structure was formed by the close-packed nanoparticles, Bragg's law can be employed to calculate nanoparticle size. The formula is given by **Equation (3)**:

$$n\lambda = 2d \sin \theta \qquad (3)$$

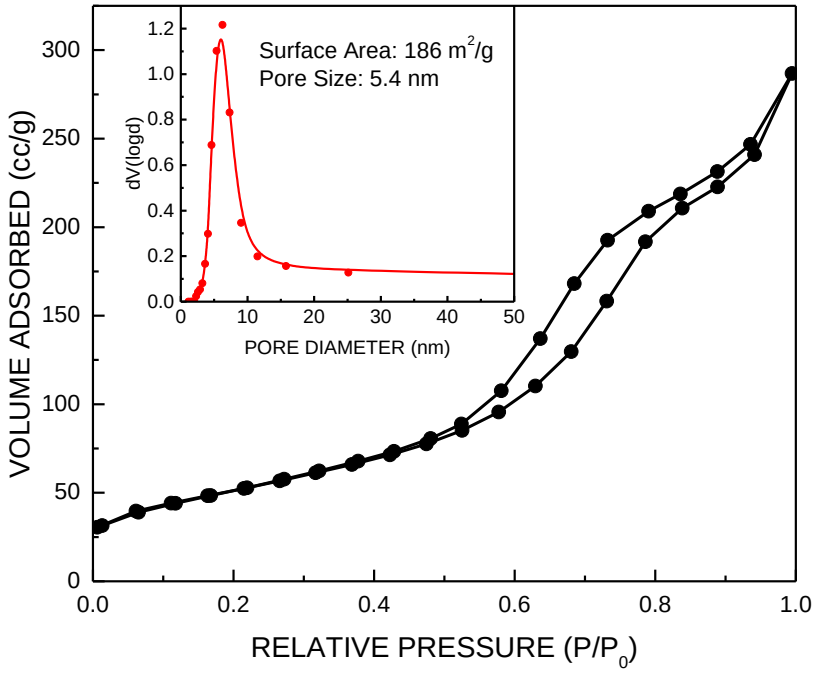

Figure 4.3. N_2 sorption isotherm of the fresh mesoporous Co_3O_4 and BJH pore size distribution (inset).

where *d* represents the d-spacing value between the lattice planes in Bragg's law. In this case, *d* is obtained by estimating the average of the fresh mesoporous Co_3O_4 particle size diameter,[11-12] which was about 11.8 nm. The peak position matches the hump of the SAXS result. The scattering pattern is represented by the black solid line. The slope of the SAXS pattern was roughly fitted by q^{-3} which is identified as the solid red line in **Figure 4.2**. These data show that the particles are formed as universally spherical shapes. **Figure 4.3** shows the N_2 sorption of fresh mesoporous Co_3O_4 sorbent. The isotherm was the typical Type IV and the hysteresis loop shape matched with Type H1, which represents a good mesoporous structure according to the definitions provided by the IUPAC.[13] The pore size distribution, shown as an inserted plot, was calculated by the BJH method.[14] The majority pore size of the material was 5.4 nm and the surface area was 186 m^2/g.

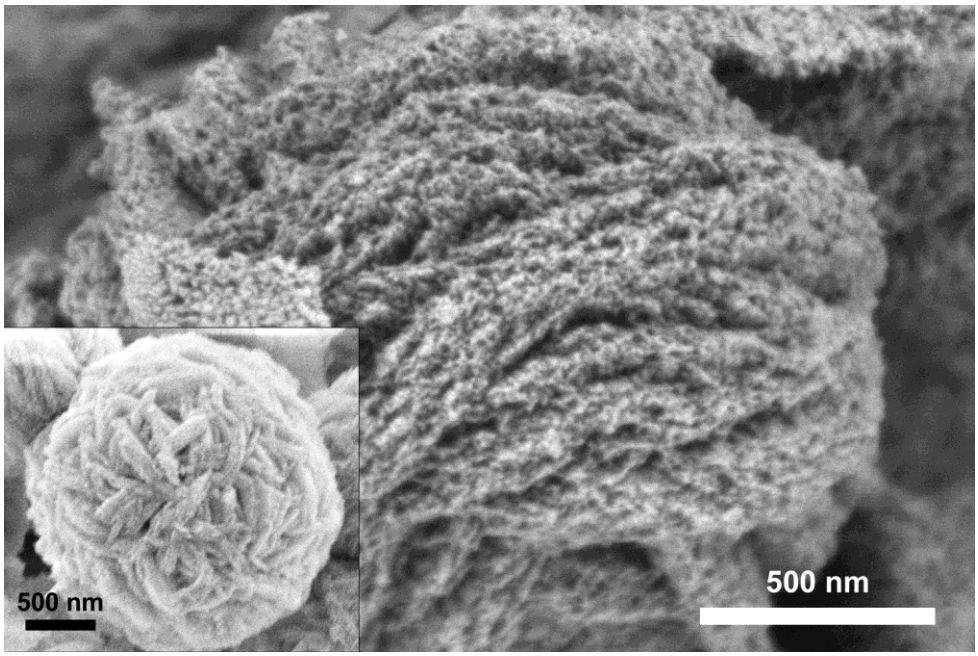

Figure 4.4. High resolution LVSEM image of the fresh mesoporous Co_3O_4.

The mesoporous nano-structure of the material was confirmed by electron microscopy. **Figure 4.4** shows the SEM images of the fresh mesoporous Co_3O_4 sorbent. The clusters were around 2 μm, which is shown in the inset. The surfaces of the clusters were formed by the sponge like rods as shown in **Figure 4.4**. The TEM images are shown in **Figure 4.5**. This mesoporous structure can be observed in **Figure 4.5a**. The particle size can be measured from the high resolution-TEM (HRTEM) image (**Figure 4.5b**), which is approximately 10 ~ 20 nm. The result is consistent with data from XRD, LAXD, and SAXS. The lattice fringes match the (111) and (220) planes of Co_3O_4. The voids among the particles can be seen in **Figure 4.5b**. In **Figure 4.5c**, the selected area electron diffraction (SAED) was taken from the 0.55 μm^2 round area. Thediameters of diffraction rings represent the d-spacings between each of the crystalline planes, which match the standard pattern (PDF Card No. 00-042-1467) of Co_3O_4. The crystalline plane indices are marked for the diffraction rings in **Figure 4.5c**.

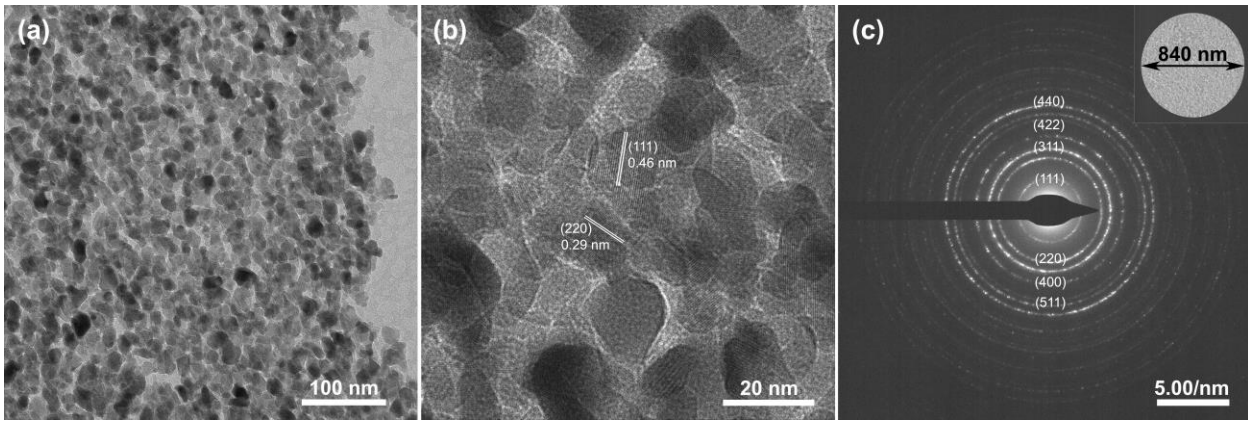

Figure 4.5. (a) TEM image, (b) high resolution TEM, (c) selected area electronic diffraction of the fresh mesoporous Co_3O_4.

4.3.2 Pressure study on the desulfurization performance of the mesoporous cobalt oxide

The breakthrough curves of the mesoporous Co_3O_4 are presented in **Figure 4.6a**. The temperature inside the catalyst bed was maintained at 200 ^oC throughout the process, which is the optimized reaction temperature.[2] The breakthrough time was longer than 26 h, when the reaction

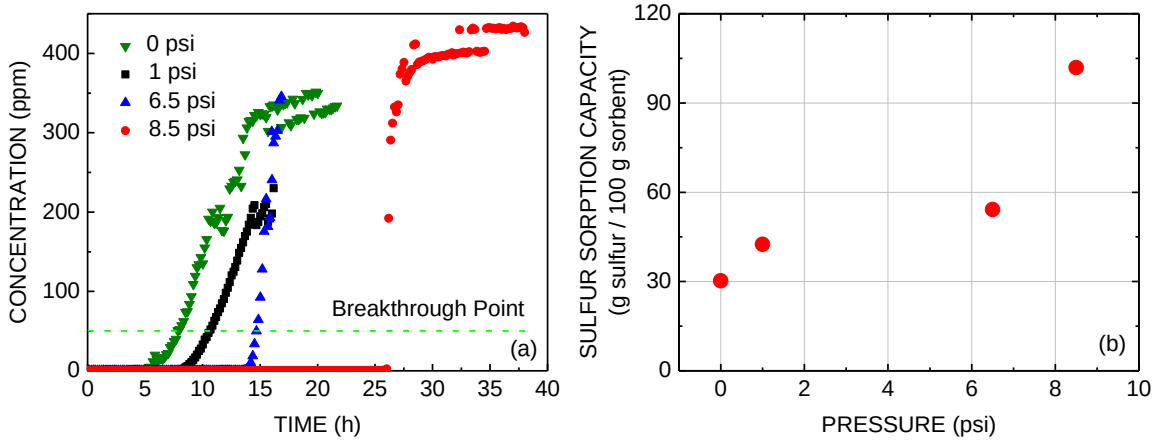

Figure 4.6. (a) Breakthrough curves and (b) sulfur sorption capacities of the mesoporous Co_3O_4 under different reaction pressure at 200 ^oC.

pressure was 8.5 psi. The pressure was constant during the reaction. As shown in **Figure 4.6b**, the sulfur sorption capacity increased with the reaction pressure. More than 101 g sulfur was absorbed by 100 g mesoporous Co_3O_4 under 8.5 psi at 200 °C. Sulfur sorption capacities (SSC)[2] were determined, according to **Equation (4)** which is shown below:

$$\mathbf{SSC}\left(\frac{\mathbf{g-sulfur}}{\mathbf{100\ g\ sorbent}}\right) = \mathbf{WHSV}\times\left[\frac{M}{V_{mol}}\times\int_0^t C_{\mathrm{in}} - C_{\mathrm{out}}dt\right]\cdot \mathbf{1}\times\mathbf{10}^{-4} \qquad \mathbf{(4)}$$

where WHSV is the weight hourly space velocity in L/h·g, M is the atomic weight of sulfur, V_{mol} is the molar volume in L/mol at standard conditions (298 K and 1 atm). C_{in} and C_{out} are the inlet and outlet concentrations in ppm, and t is the breakthrough time in h. The breakthrough time was the time when the outlet concentration reached 50 ppm.

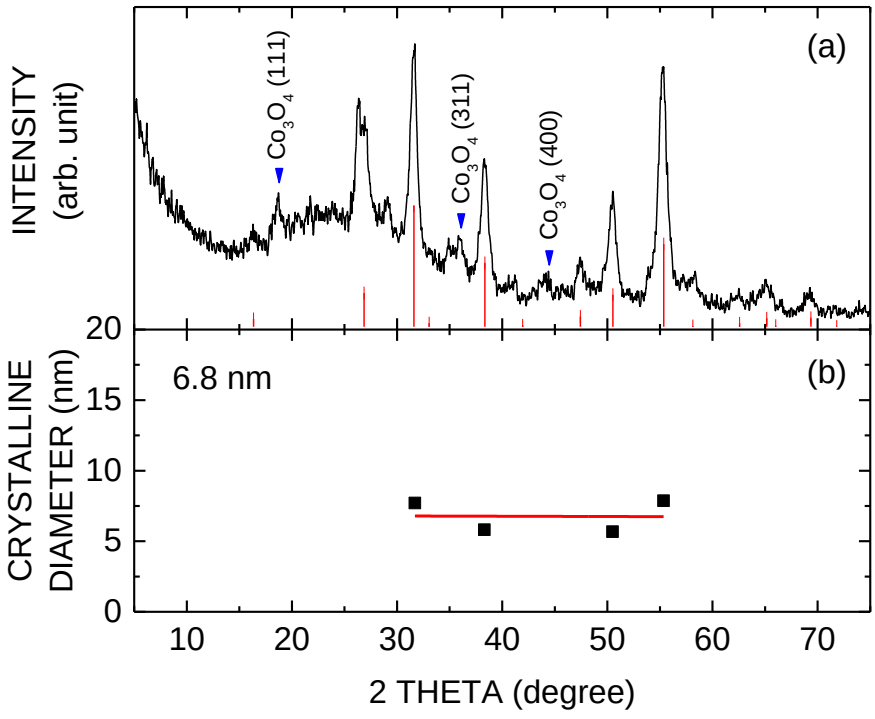

Figure 4.7. (a) Wide angle X-ray diffraction pattern of 8.5 psi sulfurized mesoporous Co_3O_4. (b) Crystalline size fitting by the Scherrer equation.

4.3.3 Characterization of the mesoporous Co_3O_4 sorbent after the desulfurization

Figure 4.7a shows the wide-angle powder X-ray diffraction (PXRD) pattern of the mesoporous Co_3O_4 sulfurized under 8.5 psi pressure at 200 ^oC. The pattern matched the Co_3S_4 standard pattern (PDF Card No. 01-071-4923) with small Co_3O_4 peaks still visible. The crystalline size of the sorbent material was reduced to 6.8 nm after about 40 h adsorption reaction under 8.5 psi at 200 ^oC.

Electron microscopy was employed to study the change of the morphology of the material after the H_2S adsorption. **Figure 4.8** shows SEM images of the sorbent after the desulfurization. The clusters were increased to around 2.4 μm in diameter. A higher magnification image is shown in the inset in **Figure 4.8**, depicting the morphology of the cluster. The particles were sintered during the 40 h reaction, forming into octahedral particles with a size of about 150 nm on average.[15] The HR-TEM of the sulfurized mesoporous Co_3O_4 is shown in **Figure 4.9a**. Most of the lattice

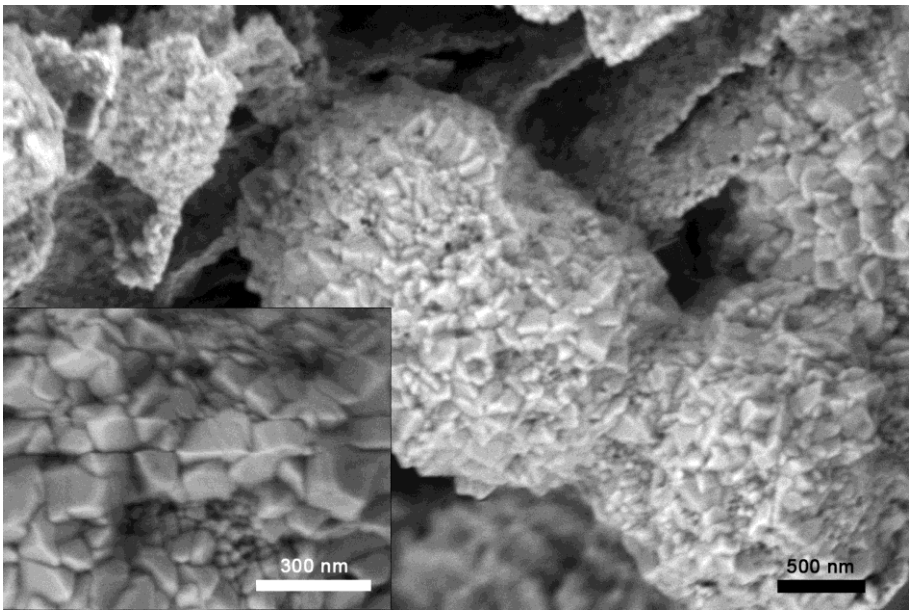

Figure 4.8. SEM image of the mesoporous Co_3O_4 sorbent after sulfurization under 8.5 psi.

fringes match up with the Co_3S_4 (220) plane. Several grains match with the Co_3O_4 (111) planes. The Fast-Fourier Transformation (FFT) pattern (**Figure 4.9a** inset) was calculated from the circled area indicated in the image in **Figure 4.9a**. In the image, about 10 nm diameter holes are seen among the grains. **Figure 4.9b** shows the diffraction pattern taken from the selected area shown in the inset TEM image. The Co_3O_4 (111) diffraction ring is marked. All other patterns matched

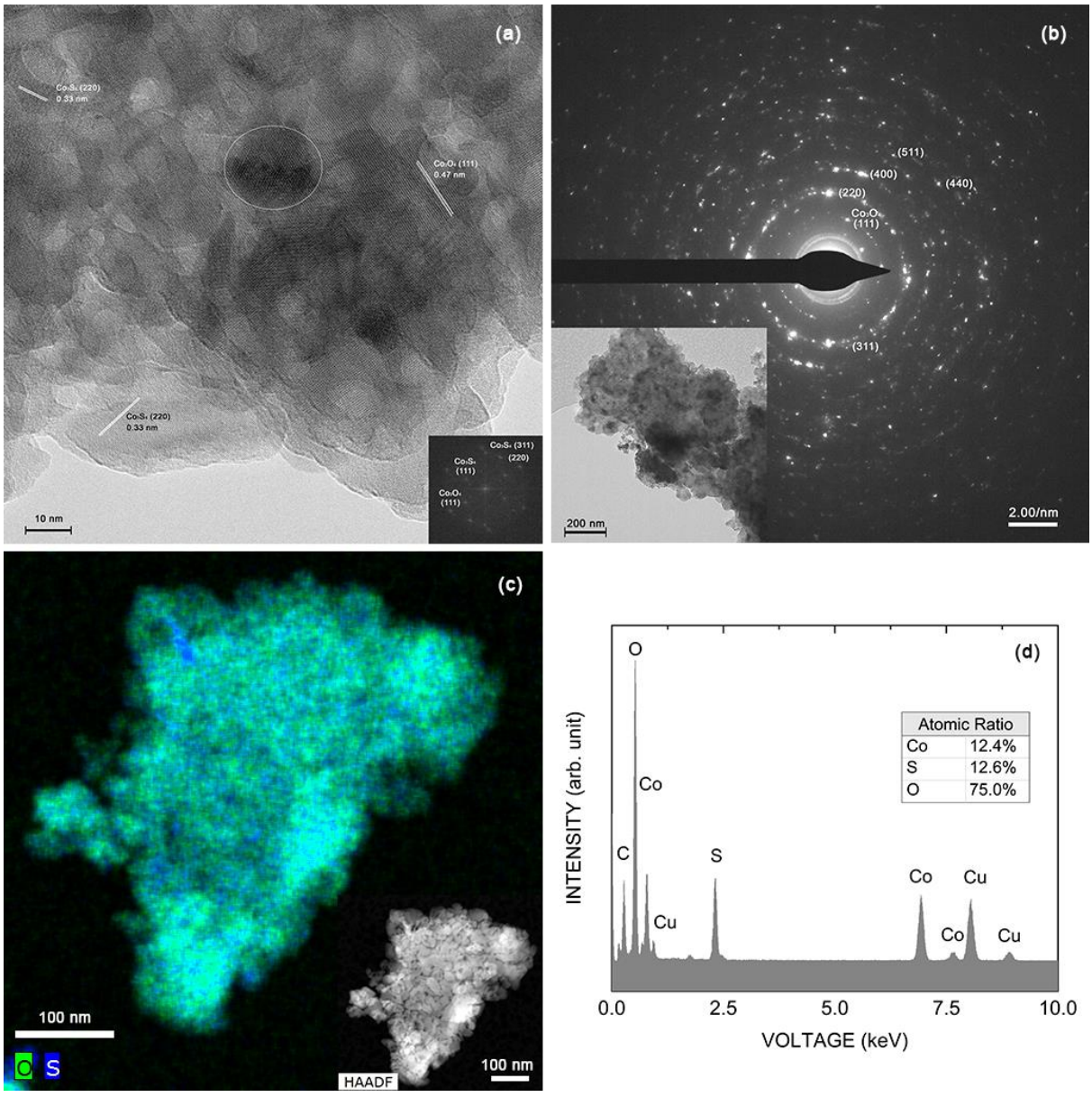

Figure 4.9. (a) High resolution TEM, (b) selected area electron diffraction, (c) elemental mapping, (d) energy-dispersive X-ray spectroscopy.

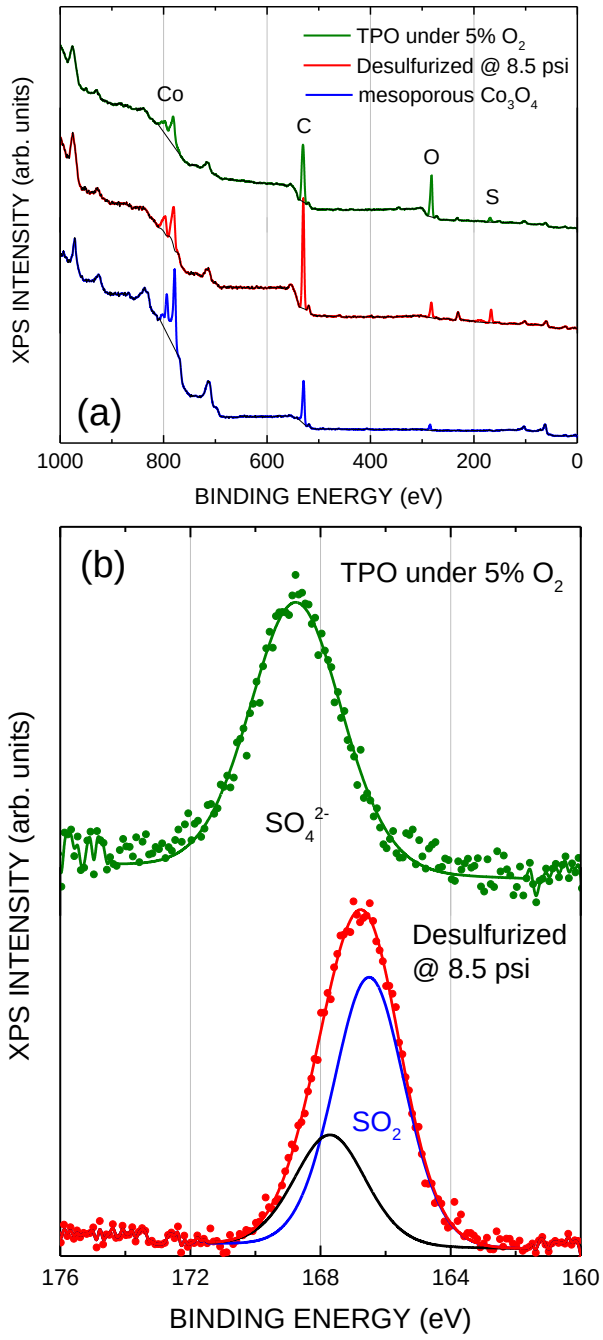

Figure 4.10. X-ray Photoelectron Spectrum (XPS) (a) the full range spectrums of fresh mesoporous Co_3O_4 (blue solid line), the sorbent after 8.5 psi sulfurization reaction (red solid line), and the sulfurized sorbent after the TPO experiment (green solid line). (b) high-resolution XPS spectrum of sulfur for the sorbent after 8.5 psi sulfurization reaction (red dots), and the sulfurized sorbent after the TPO experiment (green dots).

with the Co_3S_4 d-spacings (PDF Card No. 01-071-4923). **Figure 4.9c** is the elemental mapping from the selected area shown in the inset. The blue color represents the sulfur and the green color represents oxygen, which are mixed. From the spectrum in **Figure 4.9d**, the atomic ratio between sulfur and oxygen is about 1:6.

X-ray photoelectron spectroscopy (XPS) surface analyses of the sulfurized sorbent are shown in the **Figure 4.10**, compared to the same analyses on the regenerated Co_3O_4 sorbent by temperature programed oxidation (TPO) experiments[2]. In the full range spectra (**Figure 4.10a**), the sulfur peak appears after the desulfurization reaction and decreases after the TPO experiment[2]. In the high-resolution sulfur XPS analysis (**Figure 4.10b**), the peak shifts to higher energy levels after the TPO reaction. The area ratios of the sulfur peak and oxygen peak are 1:6 for the sulfurized sorbent, which is consistent with the elemental mapping. The ratio decreased to 1:14 for the sorbent after the TPO reaction.

4.4 Discussion

According to the characterization of the fresh sorbent, the Co_3O_4 phase was well crystallized and the mesoporous structure was well defined. The desulfurization experiments results are comparable with our previous work.[2] The sulfur sorption capacities are increasing with the reaction pressure as shown in **Figure 4.6b**. When the sulfur sorption capacities (SSC) increased, the breakthrough times of the same amount of sorbent are extended as the pressure was increasing. According to the kinetic theory of gases[16], the number of molecules N striking each square centimeter of surface per second is given by

$$N = \frac{\bar{N}P}{(2\pi\bar{M}RT)^{1/2}}, \quad \textbf{(5)}$$

where $\bar{N}$ is Avogadro's number, P is the adsorbate pressure, $\bar{M}$ is the adsorbate molecular weight, R is the gas constant, and T is in degrees Kelvin. Since the measurements were taken in the sametemperature, the sorption capacity is expected increasing with the pressure, which explains the mechanism of experiment data shown in **Figure 4.6**.

In **Figure 4.11a**, the breakthrough curve of the reaction under 8.5 psi was fitted by the deactivation model as in **Equation (5)**:[3]

$$\frac{C_{out}}{C_{in}} = \exp\left[-\frac{k_0 \cdot W}{Q_0} \cdot \exp(-k_d \cdot t)\right] \quad \textbf{(5)}$$

where $\frac{k_0 \cdot W}{Q_0}$ and k_d can be calculated from the breakthrough curve, according to **Equation (6)**:

$$\ln\left|\ln\left(\frac{C_{in}}{C_{out}}\right)\right| = \ln\left(\frac{k_0 \cdot W}{Q_0}\right) - k_d \cdot t \quad \textbf{(6)}$$

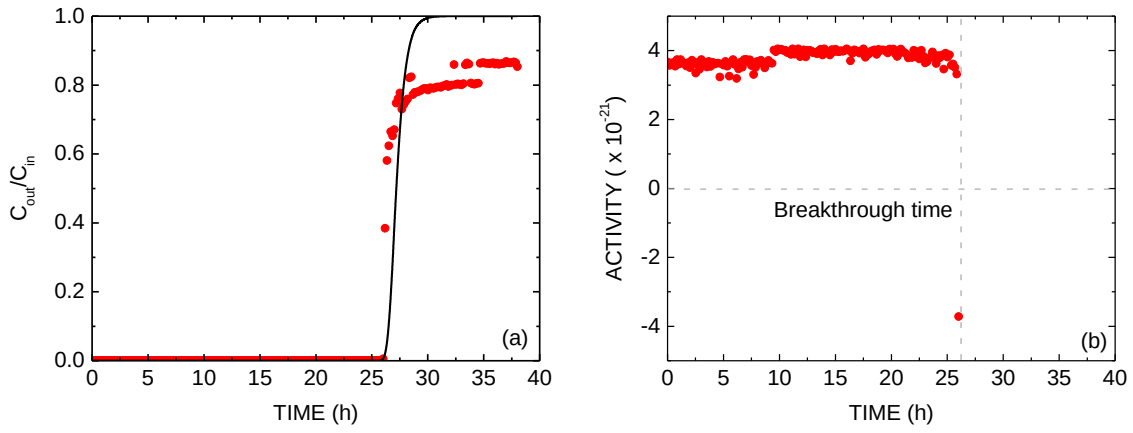

Figure 4.11. (a) the deactivation model fitting and (b) activity calculation on the breakthrough curve of the reaction under 8.5 psi.

In **Equation (6)**, W is the adsorbent weight, Q_0 is the volumetric flow rate, k_0 is the initial sorption rate constant and k_d is the deactivation rate constant. The deactivation model is a prediction of the breakthrough curve of the gas-solid reaction.[17-19] Compared with the saturation value of the model, the sorbent was converted by more than 80% during the desulfurization reaction. These data are consistent with the XRD pattern (**Figure 4.7a**) of the deactivated sorbent. A small amount of the oxide phase was observed. The HR-TEM (**Figure 4.9a**) and the SAED (**Figure 4.9b**) are showing that there is a minor amount of oxide phase existing in the sorbent after the 8.5 psi desulfurization reaction. According to the assumption of the deactivation model, the activity of the sorbent during the reaction can be estimated by **Equation (7)**:[3]

$$-\boldsymbol{Q_0}\frac{\boldsymbol{dC_{out}}}{\boldsymbol{dW}} - \boldsymbol{k_0}\cdot\boldsymbol{C_{out}}\cdot\boldsymbol{a} = \boldsymbol{0} \qquad \textbf{(7)}$$

where a is the activity of the sorbent at any time. In **Figure 4.11b**, the activity of the mesoporous Co_3O_4 dropped to zero at the breakthrough point. However, this calculation is not very meaningful after the deactivation of the catalyst. The sorbent was very stable at the high activation before the breakthrough point.

The X-ray photoelectron spectroscopy (XPS) analysis has shown that the sulfur peak appears after the desulfurization reaction. In the **Figure 4.10a**, the blue solid line represents the XPS full range spectrum of the fresh mesoporous Co_3O_4 sorbent; the red solid line represents the one after 8.5 psi desulfurization. After the temperature programed oxidation (TPO) reaction, the sulfur peak is reduced a lot. The peak ratio of sulfur to oxygen decreases from 1:6 to 1:14. The high-resolution spectrum of sulfur (**Figure 4.10b**) shows that the sulfur peak in the **Figure 4.10a** is the combination of the peak at 167.5 eV (SO_4^{2-})[20] and 166.5 eV (adsorbed SO_2)[20-21]. The cobalt sulfide on the surface was oxidized into sulfate in the air. The adsorbed SO_2 molecules were

formed by the trapped H_2S molecules and oxidized by the sorbent during the desulfurization reaction. After the TPO reaction, the adsorbed molecules might be released by high temperature calcination and the sorbent was completely oxidized into cobalt sulfate, which is shown as green dots in **Figure 4.10b**. Therefore, the sulfur sorption capacity (SSC) of the regenerated sorbent was half recovered in our previous work.[2]

The morphology of the sorbent was changed a great deal by comparison before and after the desulfurization reaction. The clusters were sintered during the reaction. The segments of the cluster were turned into octahedral shape (**Figure 4.8**) instead of the sponge-like features (**Figure 4.4**). Each of the octahedra is considered as a single-crystal particle.[15] The pores of the material might have been blocked during the reaction. Therefore, there is no peak or hump being observed from LAXD and SAXS measurements for the deactivated sorbent after the 8.5 psi desulfurization reaction.

4.5 Conclusions

This work presents a pressure study on H_2S desulfurization by mesoporous Co_3O_4 materials as a sorbent. The materials synthesized by the newly developed inverse micelle, soft-templating method yielded highly ordered pores about 5.4 nm in diameter and a surface area of 186 m^2/g. The sulfur sorption capacity was increased with increased pressure, which was maximized at 101 g sulfur per 100 g sorbent at 200 ^oC under 8.5 psi. This capacity is about 3.4 times higher than the pressure free reaction. The activation of the sorbent reached the theoretical capacity value and

was highly stable before the breakthrough point. This study proved that the mesoporous structure successfully trapped the H_2S molecules and increased the sorption capacity.

4.6 Reference

1. Beitler, C.; Fisher, K.; McIntush, K.; Tyndall, K.; Lundeen, J., When CO_2 is more hazardous than H_2S. *Hydrocarb. Process.* **2011,** *90* (1), 45-48.

2. Pahalagedara, L. R.; Poyraz, A. S.; Song, W.; Kuo, C.-H.; Pahalagedara, M. N.; Meng, Y.-T.; Suib, S. L., Low temperature desulfurization of H_2S: High sorption capacities by mesoporous cobalt oxide via increased H_2S diffusion. *Chem. Mater.* **2014,** *26* (22), 6613-6621.

3. Garces, H. F.; Galindo, H. M.; Garces, L. J.; Hunt, J.; Morey, A.; Suib, S. L., Low temperature H_2S dry-desulfurization with zinc oxide. *Microporous Mesoporous Mater.* **2010,** *127* (3), 190-197.

4. Leppälahti, J.; Koljonen, T., Nitrogen evolution from coal, peat and wood during gasification: Literature review. *Fuel Process. Tech.* **1995,** *43* (1), 1-45.

5. Torres, W.; Pansare, S. S.; Goodwin Jr, J. G., Hot gas removal of tars, ammonia, and hydrogen sulfide from biomass gasification gas. *Catal. Rev.* **2007,** *49* (4), 407-456.

6. Chung, J. B.; Chung, J. S., Desulfurization of H_2S using cobalt-containing sorbents at low temperatures. *Chem. Eng. Sci.* **2005,** *60* (6), 1515-1523.

7. Garces, H. F.; Espinal, A. E.; Suib, S. L., Tunable shape microwave synthesis of zinc oxide nanospheres and their desulfurization performance compared with nanorods and platelet-like morphologies for the removal of hydrogen sulfide. *J. Phys. Chem. C* **2012,** *116* (15), 8465-8474.

8. Flytzani-Stephanopoulos, M.; Sakbodin, M.; Wang, Z., Regenerative adsorption and removal of H_2S from hot fuel gas streams by rare earth oxides. *Science* **2006,** *312* (5779), 1508-1510.

9. Meng, X.; De Jong, W.; Pal, R.; Verkooijen, A. H., In bed and downstream hot gas desulphurization during solid fuel gasification: A review. *Fuel Process. Tech.* **2010,** *91* (8), 964-981.

10. Sethuraman, V. A.; Weidner, J. W., Analysis of sulfur poisoning on a PEM fuel cell electrode. *Electrochim. Acta* **2010,** *55* (20), 5683-5694.

11. Poyraz, A. S.; Kuo, C.-H.; Biswas, S.; King'ondu, C. K.; Suib, S. L., A general approach to crystalline and monomodal pore size mesoporous materials. *Nat. Commun.* **2013,** *4*, 2952.

12. Jin, J.; Hines, W. A.; Kuo, C.-H.; Perry, D. M.; Poyraz, A. S.; Xia, Y.; Zaidi, T.; Nieh, M.-P.; Suib, S. L., Magnetic studies of mesoporous nanostructured iron oxide materials synthesized by one-step soft-templating. *Dalton Trans.* **2015,** *44* (26), 11943-11953.

13. Sing, K. S. W., Reporting physisorption data for gas/solid systems with special reference to the determination of surface area and porosity (Recommendations 1984). *Pure Appl. Chem.* **1985,** *57* (4), 603-619.

14. Barrett, E. P.; Joyner, L. G.; Halenda, P. P., The determination of pore volume and area distributions in porous substances: I. Computations from nitrogen isotherms. *J. Am. Chem. Soc.* **1951,** *73* (1), 373-380.

15. Bao, S.-J.; Li, Y.; Li, C. M.; Bao, Q.; Lu, Q.; Guo, J., Shape evolution and magnetic properties of cobalt sulfide. *Crys. Growth Des.* **2008,** *8* (10), 3745-3749.

16. Lowell, S., *Introduction to powder surface area.* John Wiley & Sons, New York: **1979**.

17. Yaşyerli, S.; Ar, I.; Doğu, G.; Doğu, T., Removal of hydrogen sulfide by clinoptilolite in a fixed bed adsorber. *Chem. Eng. Process.* **2002,** *41* (9), 785-792.

18. Yaşyerli, S.; Dogu, G.; Irfan, A.; Dogu, T., Breakthrough Analysis of H_2S removal on Cu-V-Mo, Cu-V, and Cu-Mo mixed oxides. *Chem. Eng. Commun.* **2003,** *190* (5-8), 1055-1072.

19. Suyadal, Y.; Erol, M.; Oğuz, H., Deactivation model for the adsorption of trichloroethylene vapor on an activated carbon bed. *Ind. Eng. Chem. Res.* **2000,** *39* (3), 724-730.

20. Romano, E. J.; Schulz, K. H., A XPS investigation of SO_2 adsorption on ceria–zirconia mixed-metal oxides. *Appl. Surf. Sci.* **2005,** *246* (1), 262-270.

21. Galtayries, A.; Cousi, C.; Zanna, S.; Marcus, P., SO_2 adsorption at room temperature on Ni (111) surface studied by XPS. *Surf. Interface Anal.* **2004,** *36* (8), 997-1000.

CHAPTER 5. High Desulfurization Capacity Sorbent at Low Working Temperature: Hydrous Ferric Oxide

5.1 Introduction

Ferrihydrite is also called "amorphous ferric oxide" or "hydrous ferric oxide (HFO)".[1] As a member of iron oxides family, HFO is widely spread at the earth's surface.[2-3] This material is considered as a highly disordered material[4] and the structure is controversial issue due to its nanoparticulate nature.[5-6] According to X-ray diffraction, there are two different patterns for ferrihydrite, which are called two-line and six-line ferrihydrites. This is due to the size differences of the constitutive crystallites.[7-8] Hydrous ferric oxides is mostly referring to two-line ferrihydrite.

Because of its nanocrystal formation, ferrihydrite usually forms a nanoporous structure and yields a large surface area which would benefit as to be an absorbent. Chemically, the high density of dangling bonds and vacancies in the structure make the material have a high adsorption capacity in many environmental issued chemical species, such as arsenic, lead, phosphate, and organic molecules.[9-12] In addition, the low cost compared to the other metal catalyst materials is one of the advantages of ferrihydrite for wide use in industrial applications.

However, there is no report on using hydrous ferric oxide as a desulfurization sorbent. In this work, porous hydrous ferric oxide is synthesized by an inverse micelle sol-gel method with detailed studies on sulfur sorption capacity. The fresh sorbent and deactivate materials have been carefully characterized. The sulfur sorption capacity is much higher than the other phases or other metal oxides. Optimized working conditions are determined in this work as well. Based on

comparison of material characterization, the mechanism of the high sorption capacity is investigated.

5.2 Synthesis method

5.2.1 Sorbent Preparation

Hydrous ferrite oxide was the starting product descripted in **Chapter 3**.[13] Reagent-grade chemicals were used in the synthesis. Poly(ethylene glycol)-block-poly(propylene glycol)-block-poly(ethylene glycol) PEO_{20}-PPO_{70}-PEO_{20} (Pluronic P123) copolymer surfactant, 1-butanol (anhydrous, 99.8%), and iron(III) nitrate nonahydrate ($Fe(NO_3)_3 \cdot 9H_2O \geq 98.0\%$) were purchased from Sigma-Aldrich. Concentrated nitric acid (68%-70% HNO_3) was purchased from J. T. Baker. The material was synthesized by dissolving 4.04 g (0.010 mol) of $Fe(NO_3)_3 \cdot 9H_2O$ in 8.9 g (0.12 mol) of a 1-butanol solution containing 1.2 g (2.04×10^{-4} mol) of P123 and 1.2 g (0.019 mol) of concentrated HNO_3 at room temperature (RT). A clear gel was obtained after stirring the above-mentioned solution in a 150 mL beaker. The gel was placed in an oven and maintained at 95 ºC for 1 h. The resulting powder was washed with ethanol, centrifuged, and dried in a vacuum oven overnight. The dry powder was heated to 150 ºC for 6 hrs and then cooled down naturally to room temperature. The product was hydrous ferric oxide as the sorbent. The sulfur sorption capacity was compared with the mesoporous α-Fe_2O_3 and mesoporous Fe_3O_4 from the same batch.

As in **Chapter 3**[13], to have the mesoporous α-Fe_2O_3 and mesoporous Fe_3O_4 powder, the batches of hydrous ferric oxide were post calcined in wide different conditions. Mesoporous α-Fe_2O_3 was calcined at 400 ºC in the air for 3 hrs. Mesoporous Fe_3O_4 was heated under H_2 and Ar mixed gas at 300 ºC for 2 hrs.

5.2.2 Sulfurization Reactor

The sulfur sorption experiments were carried out on a laboratory scale sulfur sorption apparatus which is shown in **Scheme 1.1**. Fresh hydrous ferric oxide sorbent was packed in the reactor supported by quartz wool. The samples were heated at 200 ^{o}C with 40 sccm He flowing for 1 h before each experiment. The outlet gases were analyzed for sulfur using an SRI 8610C gas chromatograph (GC) with a GS-GasPro capillary column (30 m × 0.32 mm I.D.) and a flame photometric detector (FPD). A 10-port sampling valve with an electronic actuator was used to make automatic injections into the GC every 10 min with He as the carrier gas. Two mass flow controllers (MFCs) controlled the flow rates, feed, and composition. One of the MFCs is a MKS model 1479A with 20 sccm ± 1% full scale. The other is an Alicat Scientific with 200 sccm ± 0.2% full scale. The weight hourly space velocity (WHSV) was fixed at ~ 60 L/h·g.

5.3 Results

5.3.1 Fresh Sorbent Characterization

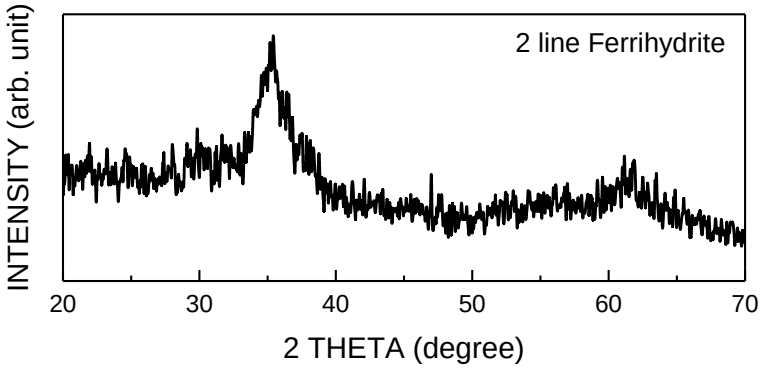

Figure 5.1. XRD pattern of the hydrous ferric oxide sorbent.

The XRD pattern of the material matches the 2-line hydrous ferric oxide pattern[4] as shown in **Figure 5.1**. Due to the nanocrystal size of the particle, the intensity of the spectrum is relatively low and peaks are broad, but the peak positions are matched with the standard pattern of hydrous ferric oxide. The peaks are too broad to calculate the grain size.

Figure 5.2 shows the N_2 adsorption isotherm hysteresis loop of the fresh hydrous ferric oxide adsorbent. The isotherm hysteresis loop shows a type I isotherm, which identifies the microporous powder. The surface area is calculated by the BET method[14] and Langmuir method[15]. Langmuir method is designed for describing the type I isotherm using a kinetic approach.[15] From the BET analysis, the surface area is 198 m^2/g and the pore volume is about 0.15 cc/g. Langmuir method gives 230 m^2/g on the analysis in the range of p/p_0 0.2 ~ 0.6. The tail of the isotherm loop turns upwards, which means the loop is starting to turn to a type II isotherm. Therefore, the pore size should be about the upper limit of the microporous size, which is about 2 nm. According to

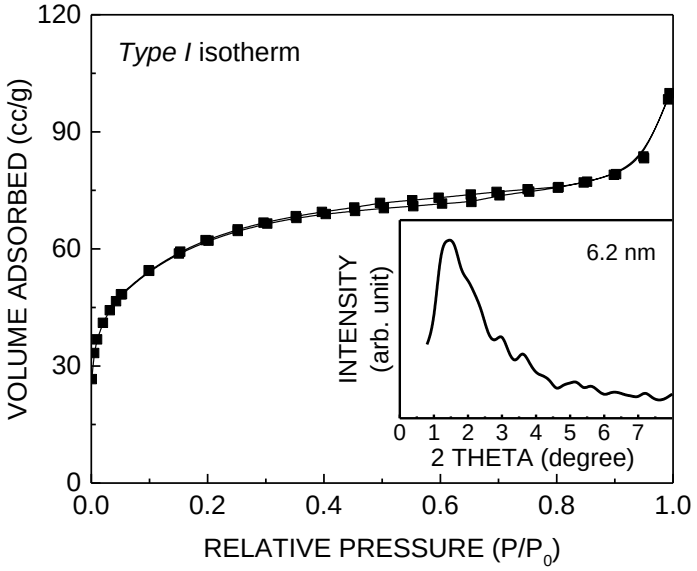

Figure 5.2. N_2 adsorption isotherm hysteresis loop of the hydrous ferric oxide sorbent. The insert picture is the low-angle X-ray diffraction pattern which is referring the center-to-center distance of the close-packed particles.

the non-linear density functional theory (NLDFT) method[16], the pore-size is about 1.2 nm which is consistent to the previous inference. The low-angle X-ray diffraction pattern is presenting as the insert picture in **Figure 5.2**. From Bragg's law $n\lambda = 2d \sin \theta$, the center-to-center distance of the close-packed particles is about 6.2 nm.

The high resolution TEM was equipped to confirm the nano-structure. The particle sizes are observing by HR-TEM in **Figure 5.3**, which is smaller than 5 nm. The voids among the particles can be barely observed from the image, but the particle arrangement can be identified from the contrast of the image. Considering the pore size estimation of the NL-DFT method from the N_2 sorption isotherm, the distance between the center of the close-packed particles is consistent with the calculation from the low-angle X-ray diffraction pattern. The insert picture is the Fast-Fourier Transform (FFT) pattern of diffraction. According to the literature[1], the structure of the

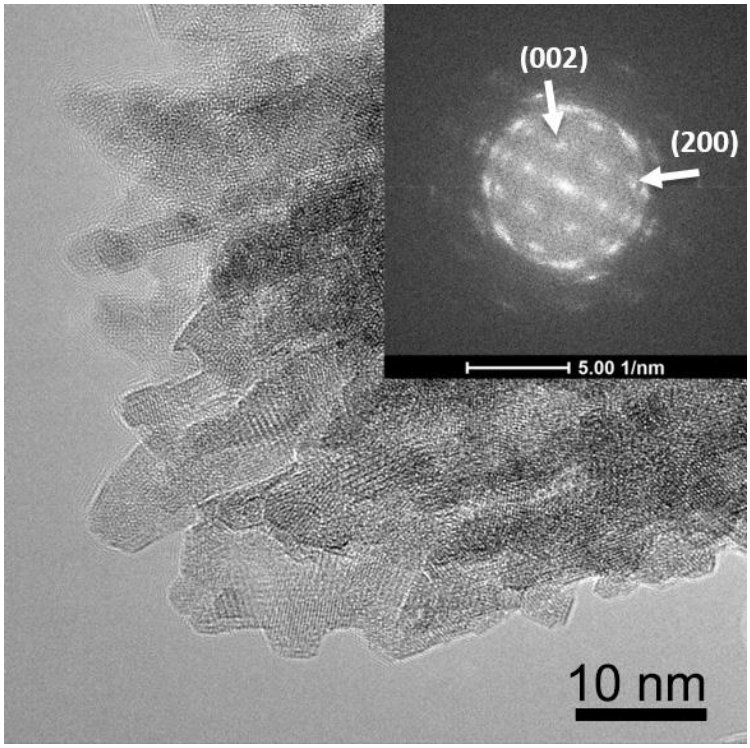

Figure 5.3. TEM image of the hydrous ferric oxide sorbent.
The insert figure is the Fast-Fourier Transform (FFT) pattern of diffraction.

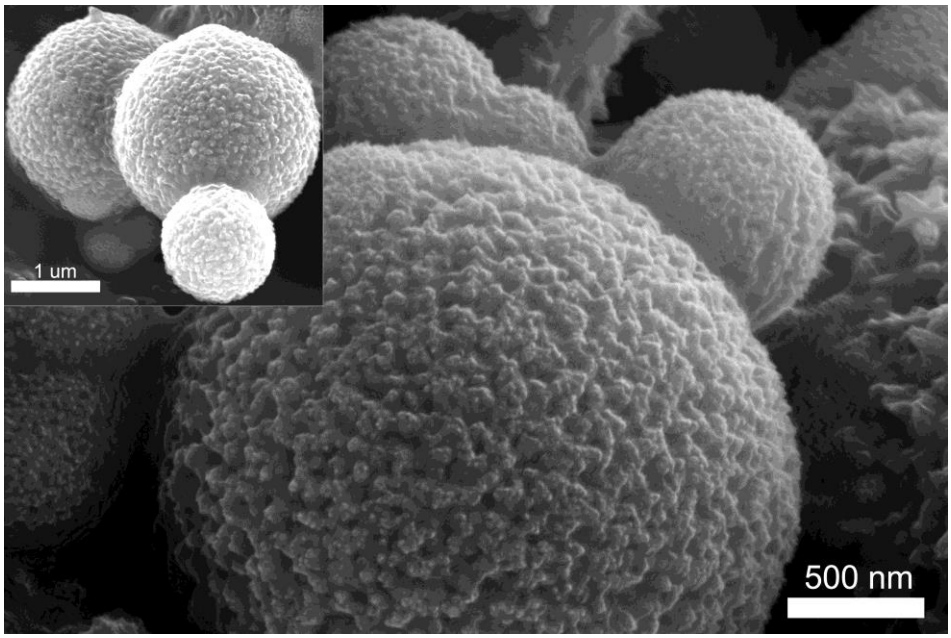

Figure 5.4. SEM image of the hydrous ferric oxide sorbent.

2-line hydrous ferric oxide is highly disordered. The face-centered cubic (FCC) and hexagonally close-packed (HCP) are mixed in the material. From the high resolution TEM, the crystallization of the material is very poor. The FFT pattern represents the highly disordered cubic close-packed (CCP) structure. The morphology of the cluster has been shown in **Figure 5.4** in the SEM image. The clusters are about 1.0 ~ 2.4 μm and formed by small particles.

5.3.2 Sulfur Sorption Capacity

5.3.2.1 Phase Effect

The different phases of iron oxides are compared in **Table 5.1**. The surface areas (SA) of each material are listed in the table. The porous materials have a higher sulfur sorption capacity (SSC) than the commercial sample, due to the large surface area. All the experiments were processed at 200 ^{o}C. Hydrous ferric oxide has the highest sorption capacity at pressure free

conditions. Mesoporous Fe_3O_4 has a little higher capacity value due to the higher processing pressure and larger surface area.

Table 5.1 Sulfur Sorption Capacity Comparison

	Microporous HFO	Mesoporous Fe_2O_3	Mesoporous Fe_3O_4	Commercial Fe_3O_4	Mesoporous Co_3O_4[17]
P (psi)	0	N/A[18]	5	0	0
SSC	42.3	24.8	51.4	9.8	30.3
SA (m^2/g)	198	N/A[18]	240	6	186

5.3.2.2 Flow Speed Effect

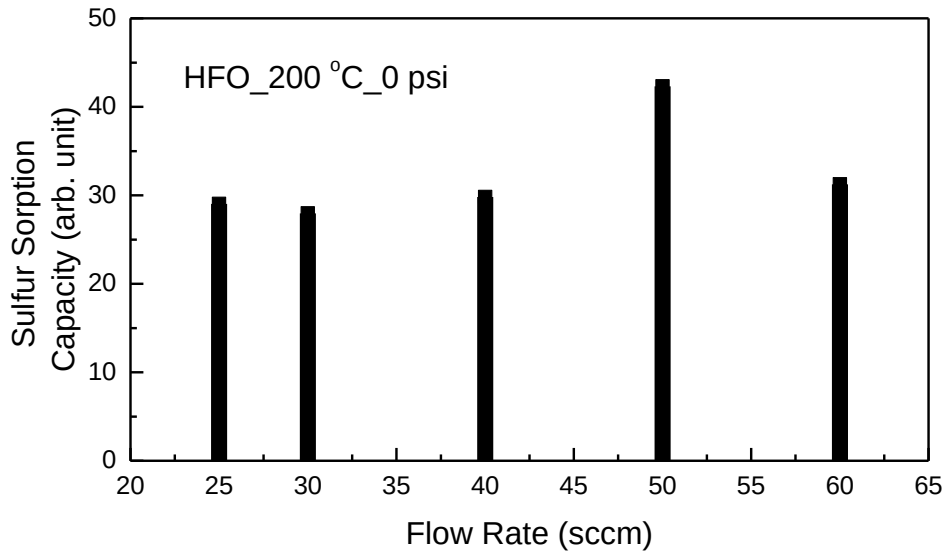

Figure 5.5. Flow Rate Effect on the sulfur sorption capacity of the hydrous ferric oxide sorbent.

Figure 5.5 shows the flow rate effect on the sulfur sorption capacity of the sorbent. The processes were under 200 ^{o}C and 0 psi. The highest sorption capacity reaches up to 42.3 at 50 sccm. With the lower flow rate, the sorption capabilities are about the same, which is about 30. The capacity dropped back, when the flow rate is even higher.

5.3.2.3 Temperature Effect

Figure 5.6 shows the sulfur sorption capacity of the sorbent under the different temperatures. The flow rates were at 50 sccm and the pressure was 0 psi. The sulfur sorption capacity is increasing with the process temperature increased and reaches the highest point at 300 ^{o}C, which is about 58.5. However, at 400 ^{o}C, the sorption capacity dropped to the lowest point which is about 22.3.

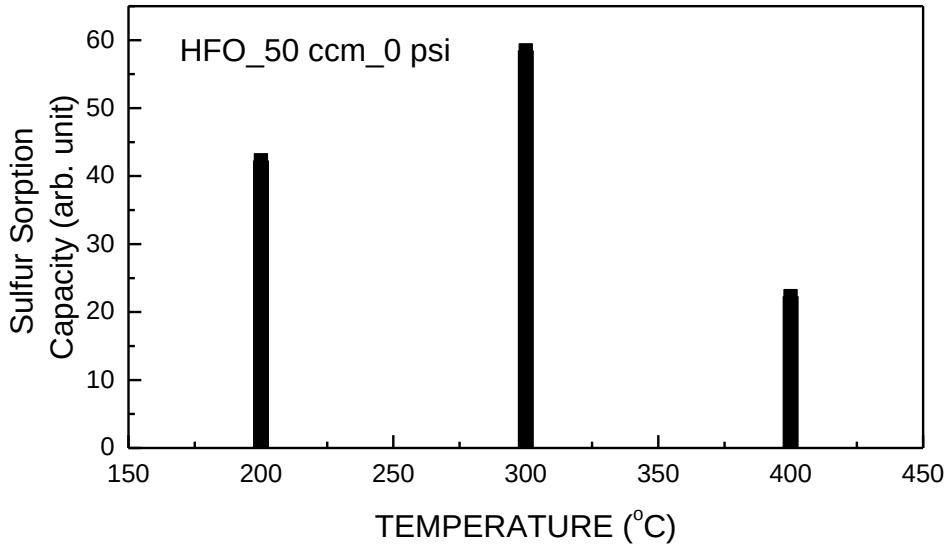

Figure 5.6. Temperature effect on the sulfur sorption capacity of the hydrous ferric oxide sorbent.

5.3.3 Material Characterization After the Sulfur Sorption Process

The sorbent was characterized after the sorption process. **Figure 5.7** represents the high resolution TEM image and the elementary mapping of the hydrous ferric oxide sulfurized with a 50 sccm flow at 300 ºC. Compared to **Figure 5.4**, the material is more crystallized and the grain size is enlarged to about 10 nm. The cluster was sintered and fully covered by sulfur based on element mapping. Oxygen might be absorbed from the air during storage and sample transfer.

The X-ray diffraction pattern of the sorbent after the sulfurization in 50 sccm at 300 ºC is

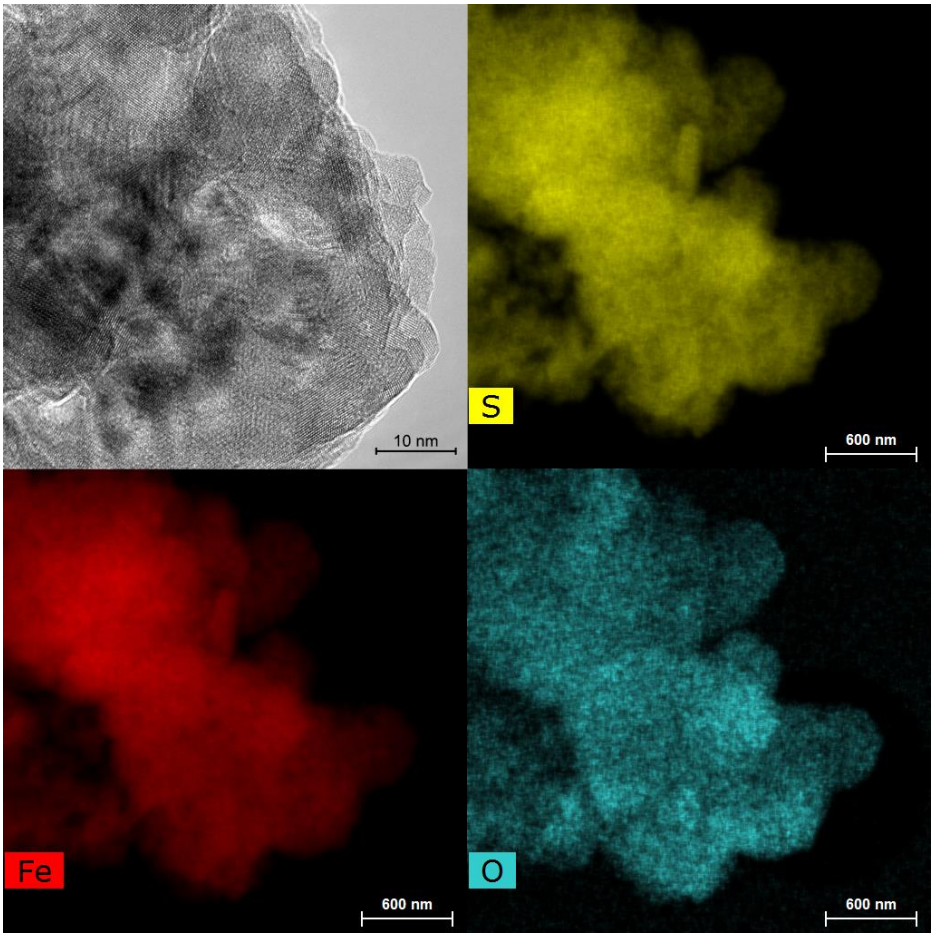

Figure 5.7. TEM image of the hydrous ferric oxide sorbent sulfurized in 50 sccm flow at 300 ºC.

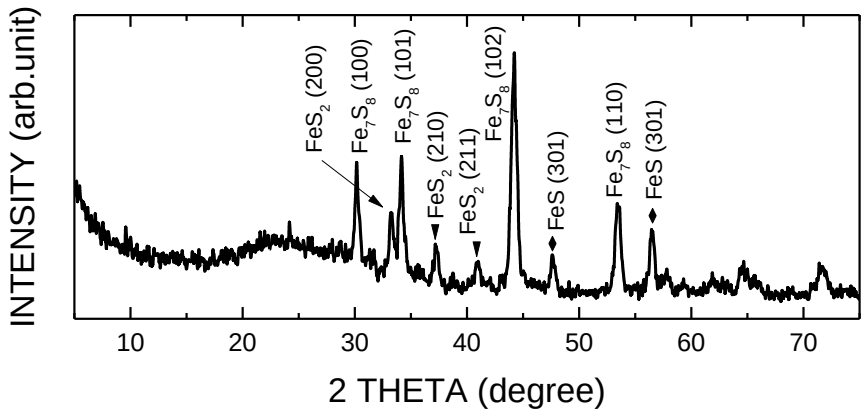

Figure 5.8. XRD pattern of the hydrous ferric oxide sorbent sulfurized in 50 sccm at 300 °C.

shown in **Figure 5.8**. The sorbent has been sulfurized during the process. The major component is Fe_7S_8 from the XRD pattern, and there is some FeS_2 and FeS mixing in with the products. According to the Scherrer equation which is shown in **Equation (1)** below, the grain size is about 14 nm.

$$D = 0.89\,\lambda / (\beta \cos\theta) \qquad (1)$$

where D is the crystalline grain diameter, β is the full width at half maximum (FWHM) of the diffraction peak, and λ is the wavelength of Cu Kα1, which is 0.15406 nm.

5.4 Discussion

The hydrous ferric oxide sorbent was carefully characterized before and after the desulfurization reaction. According to the comparison of the result, we considered the chemical reaction during the process would be as shown below[19]:

$$2\,Fe(OH)_{3\,(s)} + 3\,H_2S_{(g)} \rightarrow Fe_2S_{3\,(s)} + 6\,H_2O_{(g)} \qquad (2)$$

where Fe_2S_3 refers to the combination of Fe_7S_8, FeS_2 and FeS. Due to the different reaction conditions, such as pressure, flow rate or temperature, the ratio of the combination would be varied. Theoretically, 3 mole sulfur would be adsorbed by 2 mole iron. Comparing with the reaction on the sorbent Co_3O_4 below:

$$\mathbf{Co_3O_{4\,(s)} + 4\,H_2S_{\,(g)} \rightarrow Co_3S_{4\,(s)} + 4\,H_2O_{\,(g)},} \qquad \mathbf{(3)}$$

every mole sulfur needs 0.75 mole cobalt, which means that more H_2S would be absorbed by the same amount of hydrous ferric oxide sorbent.

Figure 5.9 is representing the trapped flow rate as a polynomial function of pressure, which is the flow rate difference in between the gas flowing in and out of the sorbent. The fitting function

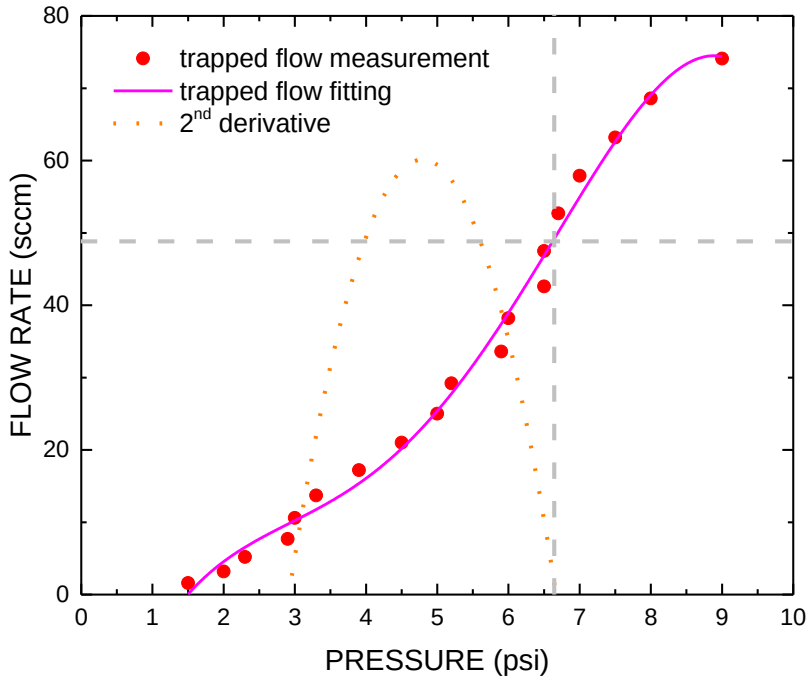

Figure 5.9. Trapped flow rate by the sorbent as a function of pressure.
The red dots represent the experiment data and the pink curve is the polynomial fitting curve.
The orange dotted line is the 2nd derivative curve of the fitting function.

is shown as below:

$$v = -0.1P^4 + 2P^3 - 12P^2 + 36P - 32, \quad \textbf{(4)}$$

The zero point of the 2nd derivative curve (orange dot) is predicting the highest trapping rate of the flow, which means that the gas molecules would be trapped fastest at 6.6 psi and equivalent to 50 sccm flow rate. Therefore, in the pressure free experiment, 50 sccm would be the optimized flow rate for the gas trapped by the porous sorbent. In the flow rate study of **Figure 5.5**, the highest capacity was consistently found at 50 sccm. In addition, during the longtime heat treatment the sorbent might be sintered and went through a phase change, so the sorption capacity dropped dramatically at 400 ^{o}C in **Figure 5.6**.

5.5 Conclusions

The microporous hydrous ferric oxide sorbent was synthesized by the inverse micelle templating method. The sorption capacity reached 58.5 with 0 psi at 300 ^{o}C and 50 sccm, which is much higher than the other transition metal oxide sorbent and other phases of iron oxides at pressure free conditions. Process condition of 50 sccm and 300 ^{o}C are optimized for HFO. Based on mechanistic studies, chemical and physical sorption occur at the same time during the process.

5.6 Reference

1. Janney, D. E.; Cowley, J.; Buseck, P. R., Structure of synthetic 2-line ferrihydrite by electron nanodiffraction. *Am. Mineral.* **2000,** *85* (9), 1180-1187.

2. Jambor, J. L.; Dutrizac, J. E., Occurrence and constitution of natural and synthetic ferrihydrite, a widespread iron oxyhydroxide. *Chem. Rev.* **1998,** *98* (7), 2549-2586.

3. Cornell, R. M.; Schwertmann, U., *The iron oxides: structure, properties, reactions, occurrences and uses*. John Wiley & Sons: **2003**.

4. Zhao, J.; Huggins, F. E.; Feng, Z.; Huffman, G. P., Ferrihydrite: surface structure and its effects on phase transformation. *Clays Clay Miner.* **1994,** *42* (6), 737-746.

5. Rancourt, D.; Meunier, J.-F., Constraints on structural models of ferrihydrite as a nanocrystalline material. *Am. Mineral.* **2008,** *93* (8-9), 1412-1417.

6. Lee, S.; Shen, Z.; Xu, H., Study on nanophase iron oxyhydroxides in freshwater ferromanganese nodules from Green Bay, Lake Michigan, with implications for the adsorption of As and heavy metals. *Am. Mineral.* **2016,** *101* (9), 1986-1995.

7. Drits, V.; Sakharov, B.; Salyn, A.; Manceau, A., Structural model for ferrihydrite. *Clay Miner.* **1993,** *28*, 185-185.

8. Manceau, A.; Drits, V., Local structure of ferrihydrite and feroxyhite by EXAFS spectroscopy. *Clay Miner.* **1993,** *28*, 165-165.

9. Foster, A. L.; Brown, G. E.; Tingle, T. N.; Parks, G. A., Quantitative arsenic speciation in mine tailings using X-ray absorption spectroscopy. *Am. Mineral.* **1998,** *83* (5-6), 553-568.

10. Welch, A. H.; Westjohn, D.; Helsel, D. R.; Wanty, R. B., Arsenic in ground water of the United States: occurrence and geochemistry. *Ground Water* **2000,** *38* (4), 589-604.

11. Hochella, M. F.; Kasama, T.; Putnis, A.; Putnis, C. V.; Moore, J. N., Environmentally important, poorly crystalline Fe/Mn hydrous oxides: Ferrihydrite and a possibly new vernadite-like mineral from the Clark Fork River Superfund Complex. *Am. Mineral.* **2005,** *90* (4), 718-724.

12. Postma, D.; Larsen, F.; Hue, N. T. M.; Duc, M. T.; Viet, P. H.; Nhan, P. Q.; Jessen, S., Arsenic in groundwater of the Red River floodplain, Vietnam: controlling geochemical processes and reactive transport modeling. *Geochim. Cosmochim. Acta* **2007,** *71* (21), 5054-5071.

13. Jin, J.; Hines, W. A.; Kuo, C.-H.; Perry, D. M.; Poyraz, A. S.; Xia, Y.; Zaidi, T.; Nieh, M.-P.; Suib, S. L., Magnetic studies of mesoporous nanostructured iron oxide materials synthesized by one-step soft-templating. *Dalton Trans.* **2015,** *44* (26), 11943-11953.

14. Brunauer, S.; Emmett, P. H.; Teller, E., Adsorption of gases in multimolecular layers. *J. Am. Chem. Soc.* **1938,** *60* (2), 309-319.

15. Lowell, *S., Introduction to powder surface area*. John Wiley & Sons, New York: **1979**.

16. Wang, B.; Dutta, P. K., Synthesis method for introducing mesoporosity in a faujasitic-like zeolite system from a sodium aluminosilicate gel composition. *Microporous and Mesoporous Mater.* **2017,** *239*, 195-208.

17. J. Jin, J. E. C., W. Song, and S. L. Suib, Pressure Effects on the High Sorption Capacity of Mesoporous Cobalt Oxide for Desulfurization at Low Temperature. *Surf. Sci.* **submitted**.

18. Pahalagedara, L. R.; Poyraz, A. S.; Song, W.; Kuo, C.-H.; Pahalagedara, M. N.; Meng, Y.-T.; Suib, S. L., Low temperature desulfurization of H_2S: High sorption capacities by mesoporous cobalt oxide via increased H_2S diffusion. *Chem. Mater.* **2014,** *26* (22), 6613-6621.

19. Davydov, A.; Chuang, K. T.; Sanger, A. R., Mechanism of H_2S oxidation by ferric oxide and hydroxide surfaces. *J. Phys. Chem. B* **1998,** *102* (24), 4745-4752.

FUTURE WORK

Porous iron oxides have been carefully studied in this work, and applied as a high sorption capacity desulfurization sorbent for low temperature H_2S removal. It would be very helpful if the material can be regenerated with the same porous structure, which will be greatly benefit industrial usage.

Based on the understanding on the desulfurization process and the study on HFO and mesoporous Co_3O_4 sorbent, an even higher sorption capacity sorbent is expected. For example, the porous $CoFe_2O_4$ or other elements doped into these materials should lead to large surface area materials that are possibly formed and easily regenerated with high sorption capacity.

According to the magnetic studies on the mesoporous iron oxides in this work, the other magnetic transition metal oxides or the mixed metal oxides in the porous structure are expecting to create unusual magnetic properties, which would be good for further applications. For instance, porous materials are widely applied for drug delivery, such as porous silicon (Anglin in *Adv. Drug Delivery Rev.*, 2008) and porous metal-organic-frameworks (Horcajada in *Nat. Mater.*, 2010). With the combination of iron oxide and silicon, Beg and co-workers published their porous Fe_3O_4-SiO_2 material as a drug nanocarrier in *J. Magn. Magn. Mater.* recently. As reported, this material has a good drug loading and release efficiency. Furthermore, the high R_2 relaxivity value supports this material as a high-performance magnetic resonance imaging (MRI) contrast agent, which might allow such drugs to be tracked during transportation.

In addition, iron oxides have been studied as anode materials for batteries. As Arico and co-workers reported in *Nature Material*, the nanoparticle sizes, porous structures, and large surface

areas will be very helpful for increasing the recharging capability. By tuning the phases and pore sizes of these materials, battery stability might be improved and this is expected.

LIST OF PUBLICATIONS

1. **J. Jin**, J. He, and S. L. Suib, High Desulfurization Capability Sorbent at Low Working Temperature: Hydrous Ferric Oxide, *In preparation*, **2017**
2. **J. Jin**, J. E. Cloud, W. Song, and S. L. Suib, Pressure Effects on the High Sorption Capacity of Mesoporous Cobalt Oxide for Desulfurization at Low Temperature, *Surface Science*, submitted, **2017**
3. J. M. Bobbitt, N. A. Eddy, C. X. Cady, **J. Jin**, J. Gascon, S. Gelpí-Dominguez, J. Zakrzewski, and M. D. Morton, Preparation of Some Homologous TEMPO Nitroxides and Oxoammonium Salts; Practical Notes on the NMR Spectroscopy of Nitroxide Free Radicals; The Observed Radical Nature of Oxoammonium Salt Solutions Containing Trace Amounts of Corresponding Nitroxides in an Equilibrium Relationship. *J. Org. Chem.*, submitted, **2017**
4. G. Liu, J. Liu, W. Li, C. Liu, F. Wang, J. He, C. Guild, **J. Jin**, D. Kriz, and S. L. Suib, Aerobic Oxidation of Alcohols over Ru-Mn-Ce and Ru-Co-Ce Catalysts: The Effect of Calcination Temperature. *Applied Catalysis A: General*, **2017**, 535, 77-84.
5. **J. Jin**, W. A. Hines, S. L. Suib, *et al*. Magnetic Studies of Mesoporous Nanostructured Iron Oxide Materials Synthesized by One-Step Soft-Templating. *Dalton Trans.*, **2015**, 44, 11943.
6. C. C. Agosta, **J. Jin**, W. A. Coniglio, B. E. Smith, *et al*. Experimental and Semiempirical Method to Determine the Pauli-limiting Field in Quasi-Two-Dimensional

Superconductors as Applied to κ-(BEDT-TTF)$_2$Cu(NCS)$_2$: Strong Evidence of A FFLO State. *Phys. Rev. B*, **2012**, 85, 214514

7. W. B. Mi, **J. Jin**, H. L. Bai. Enhanced Magnetic Properties of Annealed $Fe_{48}Pt_{52}$-C Composite Films by N Incorporation, *Phys. Stat. Solid. A*, **2011**, 208, 904-909

8. W. B. Mi, **J. Jin**, H. L. Bai. Dependence of Magnetic Properties on The Film Thickness and Pt Atomic Fraction of Post-Annealed $Fe_{1-x}Pt_x$-C Granular Films on MgO(100) and SiO_2/Si(100) Substrates, *J. Alloys. and Compd.*, **2011**, 509, 141-146

9. W. B. Mi, **J. Jin**, H. L. Bai. Effect of Mn Doping on The Magnetic Properties of the Post-Annealed $Fe_{48}Pt_{52}$-C Composite Films, *Phys. Stat. Solid. A*, **2011**, 208, 2198-2202

10. W. B. Mi, X. C. Wang, **J. Jin**, H. L. Bai. Structure and Magnetic Properties of Sputtered $(Fe_{1-x}Cr_x)_{0.09}Cu_{0.91}$ Solid Solution Films, *Thin Solid Films*, **2010**, 518, 6137-6141

11. W. B. Mi, **J. Jin**, H. L. Bai, The Method of Reducing the $L1_0$–FePt Grain Size in Films by Doping N, China Patent, CN200910312058.9, Dec. 23rd, **2009**.